Black Phosphorus: Pristine and doped surface investigations using Scanning Tunneling Microscopy

DISSERTATION
Submitted for the partial fulfillment of the requirement

for the degree of

DOCTOR OF PHILOSOPHY

by

Abhishek Kumar

under the supervision of

Prof. Stefan Heun

Scuola Normale Superiore di Pisa, Italy
Pisa, 2019

Abstract

Black Phosphorus (bP) is the most stable allotrope of phosphorus, first synthesized in 1914 by Bridgman. It was investigated along with other layered materials like GaS, GaSe, GaTe, graphite, boron nitride and transition metal dichalcogenides for nearly a century. One important characteristic of these layered materials is that they are composed of two-dimensional (2D) sheets of covalently bonded atoms that are kept together by van der Waals forces. Therefore, they were perceived as interesting materials with an ambition to achieve thinner and thinner materials, up to a single monolayer, called 2D materials.

In 2004, Andre Geim and Konstantin Novoselov demonstrated the first successful preparation of one-atomic-thin carbon films, called graphene. They used the technique of scotch tape exfoliation and studied the marvelous properties of graphene, which got them the Nobel Prize in physics in 2010. With the discovery of interesting properties of graphene, a search for other 2D materials started. A range of such materials have been realized since then, like hexagonal boron nitride (h-BN), silicene, germanene, stanene, and transition metal dichalcogenides (TMDCs). Black Phosphorus (bP) is an important part of this class of 2D materials, from which phosphorene is exfoliated.

Phosphorene, first exfoliated in 2014, has emerged as an important material. With its band gap tunable with thickness (from 2.0 eV for the single layer to 0.3 eV for the bulk), it occupies a special position between zero band gap graphene and high band gap TMDCs. Anisotropy is another important aspect discovered in its properties like effective mass, mobility, thermal conductivity, and plasmon resonance. This opens a gate for potential applications in electronics, photonics, thermoelectrics, and for gas sensing devices.

Surface studies of bP are quite limited so far. There have been some works reported showing bP atomic resolution and tunneling spectra on bP surfaces. However, most of them have been performed on cleaved bulk bP crystals. From a 2D application point of view, however, it is important to study thin exfoliated bP flakes. The majority of work reported until now on thin bP flakes concerns electrical transport or optical experiments, performed on flakes encapsulated in a protective layer. The reason for this is to protect the material from oxidation upon exposure to air, since bP is known to be highly reactive. One STM study on a few nanometer-thin bP flake shows surface atomic resolution, but mainly focuses on the spectroscopic properties of bP. Since surface plays an important role in nanomaterials due to the high surface-to-volume ratio, it is very important to understand the surface behavior of such materials.

Here, we have prepared samples on which surface studies on exfoliated bP flakes could be done. We have prepared samples by exfoliating bP in a glove bag continuously flushed

with nitrogen, which provides an inert atmosphere and protects the reactive bP surface from oxidation. We have used graphene on silicon carbide (SiC) as a substrate, which provides large atomically flat terraces of SiC and a conducting graphene sheet on top – fulfilling major requirements for scanning tunneling microscopy (STM) experiments. We mount the sample inside the glove bag and transfer it under inert atmosphere, which helps in preserving the highly reactive bP surface from oxidation. This is confirmed by flat, clean, and oxide-free bP surfaces as seen in STM.

We initially started with the investigation of surface behavior with temperature. We found that 200 °C to 300 °C is a proper temperature range for cleaning the surface. We saw defects on the clean bP surface, reported earlier to be the reason for the intrinsic p-type doping of bP. At 375 °C to 400 °C, eye-shaped craters started to develop on the surface due to phosphorus desorption. Meanwhile, we solved an existing debate in the literature regarding the orientation of the long axis of these elongated craters: along the crystallographic armchair direction due to an atomic phosphorus desorption mechanism, or along the crystallographic zigzag direction due to a molecular P_2 desorption mechanism, both investigated by electron microscopy and diffraction studies. Armed with the power of atomic resolution imaging enabled by the STM technique, we were able to resolve smaller craters, which are the seeds of the larger craters reported in previous studies. With a statistical analysis, we confirmed the specific directionality of the orientation of these anisotropic craters. Furthermore, with the help of atomic resolution provided by STM, we could directly compare the crater alignment with respect to atomic arrangement, and found that the long axis of the craters is aligned with the zigzag direction – thus solving the existing debate in the literature.

bP is intrinsically p-doped. Some works were performed to obtain an n-type behavior by doping, as it would allow p-type and n-type behavior in the same material, very useful for basic diode applications. In one paper focusing on devices, copper adatom doping has been shown to yield n-type behavior, using transport measurements. Here, we study copper growth morphology on bP. We observed the preference of copper atoms to occupy atomic vacancies of the bP surface. We also observed an alignment of copper islands along the crystallographic armchair direction of bP, and a step decoration of copper islands at bP step edges. With scanning tunneling spectroscopy, we studied the transfer doping of bP by copper at the local atomic level and found a shift of the Fermi level in bP from p-type behavior to n-type behavior. We also observed an increase in the band gap value measured on doped bP, consistent with DFT calculations.

Acknowledgements

PhD is a journey. And I am grateful to many for their support during this journey. Two most important persons who made this work possible are Prof. Stefan Heun, my supervisor and Dr. Francesca Telesio. First and foremost, I am thankful to Prof. Stefan Heun for giving me an opportunity to work with him. Your useful guidance directed my efforts on track and your foresightedness showed me the way when I could not see one. I used to come to your office multiple times to discuss my experiments and you always made time for me. I am very thankful for your time, patience, constructive feedback and an open atmosphere that I could freely discuss my thoughts and concerns without hesitations. I always left your office having learnt something new. You are an excellent supervisor, brilliant scientist and a very optimistic person - everything that a PhD student could wish for. Dr. Francesca Telesio, you were like my second supervisor. You were always there for me whenever I needed any advice or help, in academic as well as non academic matters. I learnt so many things from you, from scotch tape exfoliation to organizing things. You were there for me when I used to get stuck by tiniest and silliest obstacles. The road maps you made after every meeting played a very significant role in finishing my experiments and thesis on time. With your patience, passion and attention to details, I already believe that you are going to be a great supervisor in future. I am thankful to both of you for reading parts of my thesis every weekend and giving your quick feedback, which helped me finish thesis on schedule. I feel very fortunate to get the chance to work with both of you.

I am thankful to Prof. Fabio Beltram and Prof. Vittorio Giovannetti who were my internal supervisor at Scuola Normale Superiore. I would like to thank Dr. Pasqualantonio Pingue to oversee safety as well as to let me stay at NEST to finish my thesis even after finishing my contract.

As a part of my PhD curriculum, I attended several courses, which strengthened my understanding of physics of condensed matter and nanosciences. I am thankful to Prof. La Rocca, Prof. Stefano Luin, Prof. Rosario Fazio, Prof. Fabio Beltram, Prof. Miriam Serena Vitiello, Prof. Stefano Roddaro, Prof. Stefan Heun, Prof. Lucia Sorba, Prof. Fabio Taddei and Prof. Francesco Rosella for sharing their knowledge.

I would like to thank Dr. Yuya Murata and Dr. Holger Buch, working with whom I learned the basics of STM and UHV. On first glance what looks so complex, thanks to them, I was able to work independently on it. I would also like to thank Dr. Stiven Forti for his understanding while sharing machine usage time and for his time-to-time useful feedbacks.

Graphene on SiC substrates were provided by the goup of Dr. Camilla Coletti at Centre for Nanotechnology Innovation at NEST, IIT Pisa. I am thankful to her and her group members Dr. Stiven Forti, Ameer Al-Temimy and Dr. Neeraj Mishra for providing me substrates of high quality whenever I needed for sample preparation, sometimes even on short notice. I would additionally like to thank Dr. Neeraj Mishra, not only for training and teaching me how to use AFM, which was hepful for me to characterize the graphene substrates, but also for being a great friend and companion. I am thankful to Dr. Manuel Serrano-Ruiz and Prof. Maurizio Peruzzini from CNR-ICCOM, Firenze for providing high quality pristine bP crystals. I would like to thank Prof. Lucia Sorba for allowing us to use her CBE lab space inside clean room of NEST, Pisa for carrying out bP exfoliation and sample preparation. I would also like to thank Dr. Valentina Zannier from CNR-Nano Pisa for performing energy dispersive X-ray spectroscopy (EDS).

While working in lab during last years, I spent a lots of time with my group members. They were eager to discuss their work even when our projects were so different. I am thankful to Prof. Stefano Veronesi, Dr. Francesca Telesio, Dr. Sedighe Salimian, Dr. Shaohua Xiang, Stefano Guiducci, Luca Planat, Lennart Bours, Dr. Alina Mrenca-Kolasinska, Sara Fiori, Thea Papa, Gwenael Le Gal, Zoe Dubois, Marion Bonhomme, and Luca Basta for their interest and ideas, which helped me gain more insights and for making the lab such a friendly place.

I also had lots of opportunities to interact with people working at NEST apart from my group members. I would like to thank fellow colleagues at NEST, Umesh Gomes, Ilirjan Aliaj, Vinoshene Pillai, Abhishek Dubey, Roberta Cecchi, Keagan, Ajesh, Akash, Omer, Bala, Filippo Fabri, Sara, Titti, Domenica Convertino, Domenico Cassano, Cecilia, Paola Parlanti, Melissa, Ambra, Gina, Matteo, Simone Biasco, Dominic Prete, Alessia, and many more. I am thankful to Isha for her continuous support and encouragement. I would also like to thank 'Mensa friends', Henry, Romi, Tanvi, Arturo, Ophelie, Molly, Maisie, Akie, Maria Paola, Tonio and many others with whom I used to had healthy discussions on diverse topics.

I would like to express my gratitude to the members of my dissertation committee: Prof. Giuseppe La Rocca, Prof. Vittorio Giovannetti, Prof. Antonio Politano, Prof. Thomas Szkopek, Prof., Lucia Sorba and Prof. Francesco Rossella who kindly accepted to be in the committee and dedicated time to examine my thesis in their very busy schedule.

Finally, I thank my family, mummy, papa and Anshu, for your endless love and support. Thanks for always encouraging me to pursue my dreams. Your unwavering and unselfish love always motivated me and made me believe that nothing is impossible.

Contents

Chapter 1

Introduction

The field of van der Waals materials has been pursued as a field of interest in material science research for nearly a century. These materials consist of atomic planes, held together by van der Waals forces. Layered materials like GaS, GaSe, GaTe and InSe were investigated. Bassani *et al.* [1] published a theoretical study of band structure and optical properties of layer compounds, which were also explored experimentally [2–4]. Detailed reviews of transition metal layer compounds have been presented by Yoffe *et al.* [5, 6]. Graphite was recognized as an interesting layered material which attracted extensive interests to obtain nanometer thin films. 50 nm thin films of graphite were grown by pyrolysis of methane on single crystalline nickel in 1966 [7]. One to two monolayer graphite films were grown on LaB_6 in 1977 [8]. Monolayer graphite films were reported by carbon segregation on Ni(111) [9], Pd(100), Pd(111) and Co(0001) [10] and by chemical vapor deposition technique on metal carbides like TaC(111), HfC(111), TiC(111) and WC(0001) [11]. Several interesting experimental works were published by Oshima *et al.* investigating physical properties like phononic behavior [11, 12], electronic band structure [1, 13, 14], plasmonic behavior [15], and thickness dependent electronic states [16] of monolayer graphite. Surface investigation of monolayer graphite on TiC(111) was performed using scanning tunneling microscopy which showed a moire pattern formed by the superposition of the 2D atomic structure of graphite and the Ti-layer [17]. Thin films of hexagonal boron nitride (h-BN) were prepared [18] in which electronic dispersion on metals were studied [19, 20]. Black phosphorus is another layered material, which was intensively investigated. It was first prepared by Bridgman in 1914 [21]. Electronic investigations demonstrated that it is an intrinsically p-type semiconductor with a direct band gap of ∼0.3 eV. A hole mobility of ∼200 $cm^2/V{\cdot}s$ was reported at room temperature [22]. Other investigations were also reported studying its structural [23, 24], optical [25–27], electronic [22, 28, 29] and superconducting [30, 31] properties.

One reason for the interest in van der Waals materials was the aim to prepare single atomic layer-thin materials. Van der Waals materials were perceived as potential candidates in which it could be realized since these materials are essentially composed of layers of single atomic planes bound by van der Waals forces only. The task to exfoliate these materials was challenging and remained difficult for a long time. However, the field of 2D materials attracted significant attention after the first successful realization of graphene by Geim and Novoselov at the University of Manchester in 2004. They developed the method of scotch tape exfoliation of graphite [32–34], for which they were awarded the Nobel Prize in 2010 to honour their "groundbreaking experiments regarding the two-dimensional material graphene" [35]. With the expansion of the 2D material family, different materials with a wide range of properties have been realized, from conducting semi-metal graphene to semiconducting direct-band gap transition-metal dichalcogenides (TMDCs) [36], and to insulating hexagonal Boron Nitride (h-BN) [37]. 2D-Xenes [38], monolayer sheets of group IV-A elements like Silicon, Germanium, and Tin, called Silicene [39], Germanene [40], and Stanene [41], respectively, have been realized experimentally, and found to have interesting properties like large, tunable band gap and robust quantum spin Hall states, suitable for applications in the field of room temperature 2D topological insulators [42], anomalous Seebeck effect devices [43], and other spintronic applications [44]. Borophene, a monolayer sheet of Boron, has been synthesized and reported to have a highly anisotropic metallic character [45, 46].

The realization of these members of the 2D family with a wide range of properties paves the way for the realization of 2D heterostructures [47], in which different 2D crystals can be stacked on top of each other to make artificial heterostructured materials with desired properties. In this way, if one member of the 2D family does not fulfill the requirements, another member can be called upon to complement it and provide the desired performance. Black phosphorus (bP), which is the second elemental material to be exfoliated [48, 49], serves an important role in this regard. Bulk bP has a direct band gap of ∼0.3 eV, which can be tuned to ∼2.0 eV by decreasing the number of layers to a single monolayer of bP [50, 51]. With this range of values of band gap, it fills the void between zero band gap graphene and high band gap TMDCs [52]. Anisotropic crystallography imparts anisotropy to its optical [53], electronic [54] and thermal properties [55], which further adds to its virtuosity. Even when used independently, many practical applications have been realized for bP in electronics [48, 53, 56, 57], photonics [58–60], thermoelectric [61, 62] and gas sensing [63] devices.

I have focused my thesis on the surface properties of few atomic layer thin exfoliated bP flakes. This is interesting from a 2D materials application point of view, since a 2D material is essentially just a surface. However, the high reactivity of bP makes such an investigation challenging, which can be understood from the fact that surface studies on bP till now are severely limited. The main challenge in carrying out such investigations is the preparation of thin bP samples whose surface remains preserved. We have developed a strategy to solve this problem in a quite easy and inexpensive way, by using a glove bag which provides an inert atmosphere. The effectiveness of our sample preparation protocol is reflected by the high quality of STM images of the bP surface achieved in our experiments. Any such study that deals with surface studies of exfoliated bP flakes is interesting and important because it provides a simple and smart way to cope with the difficulty currently experienced by the community.

Since most synthesis methods and conventional device processing techniques require a high temperature treatment, it is essential to understand temperature dependent surface morphological changes of bP. Being able to prepare high quality surfaces of exfoliated thin bP samples suitable for surface investigations, we have carried out such experiments. Meanwhile, we found an existing debate in the literature regarding anisotropic craters on the bP surface and their elongation direction with respect to the crystallographic directions of bP, which we have solved taking advantage of the power of atomic resolution provided by STM. This gives interesting insights into the underlying phosphorus desorption mechanism resulting in anisotropic crater formation due to annealing.

bP is intrinsically p-type doped due to atomic vacancies [64]. Koenig *et al.* [65] has shown by transport measurements n-type doping in thin flakes of bP due to copper deposition. This n-type doping is important for applications of bP as a semiconductor. However, the physical morphology of copper deposited on bP in the study is not reported. We have performed such an investigation to shed light on changes in the morphology of copper on bP as well as on the electronic band structure of bP. We observe a shift of the Fermi level from p-type to n-type due to copper deposition and an increase in the band gap value measured on copper doped bP. Our study also provides an investigation at the nanometer level of doping caused by copper.

This thesis is organized in six chapters. This Chapter 1 presents an introduction to the work on surface investigations of exfoliated pristine and doped bP conducted by STM in an UHV environment presented in this thesis. Chapter 2 gives an overview of the reported results in literature, to understand the current state of the art of bP surface and doping studies. Chapter 3 explains the details of the various techniques used to perform experiments, like the basics of scanning tunneling microscopy, sample fabrication, and sample characterization techniques. Chapter 4 discusses the results obtained investigating the thermal properties of pristine bP surfaces. Chapter 5 discusses the morphological aspects of the growth of copper on bP as well as the electronic effect of copper on bP at the atomic level. Finally, Chapter 6 wraps up the thesis by providing a summary of all experiments and discusses future directions from this work.

Chapter 2

State of the Art

2.1 Recent advances in black phosphorus (bP)

Black Phosphorus (bP) is the most stable allotrope of phosphorus. The crystallographic structure of bP is very similar to graphite. Each phosphorus atom is strongly bonded to three other phosphorus atoms lying in the same layer, and each layer is only weakly bonded to the other layers through van der Waals forces. But a phosphorus atom has five electrons in its valence band. With three of them bonded to three other phosphorus atoms, the remaining two electrons form a lone pair, making each phosphorus atom in bP sp^3 hybridized, in contrast to graphite where each carbon atom is sp^2 hybridized. Also, because of the presence of a lone pair on each phosphorus atom, these three bonds do not lie in the same plane. Because of the repulsion of the three bonds by the lone

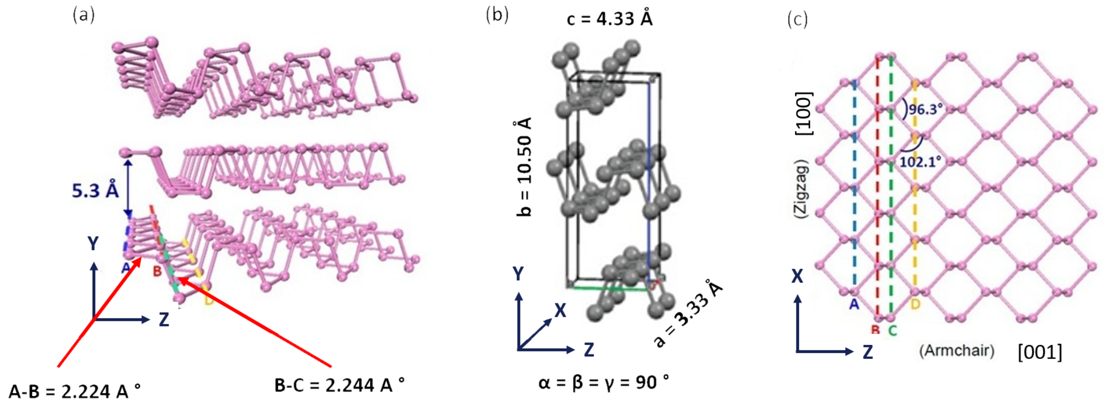

Figure 2.1 Schematics showing bP crystallography. (a) Side view of bP crytal lattice. Two different bond lengths are shown. (b) Orthorhombic unit cell of bP. Unit cell parameters are shown. (c) Top view of bP in which single layer of bP is shown. The zigzag and armchair directions are indicated. (a) and (c) are adapted from ref. [52]. (b) is reproduced from ref. [66].

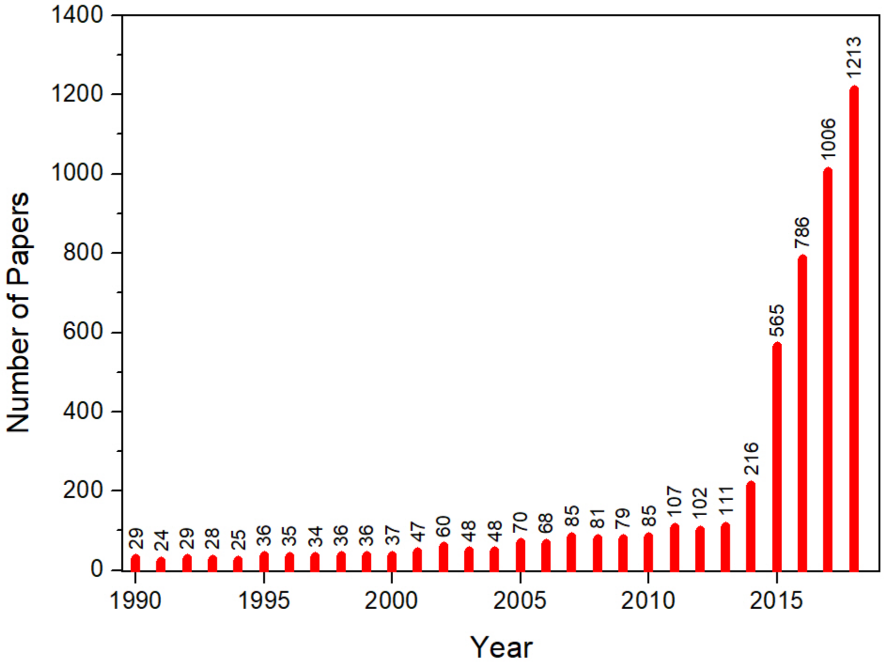

FIGURE 2.2 Number of academic papers published in more than two decades in which the term 'black phosphorus' or 'phosphorene' is mentioned in the title, abstract or keyword. The graph is plotted using data extracted from Scopus.

pair, a single layer of phosphorus in bP is not flat as graphene, but instead it is buckled, such that a single layer of bP has phosphorus atoms in two planes [52, 66], as shown in Fig. 2.1(a), which shows a schematics of a bP crystal. Each layer can be seen to have phosphorus atoms in two different planes, which illustrates that each layer of bP is buckled. A crystal of bP has an orthorhombic unit cell, as shown in Fig. 2.1(b), with unit cell parameters a = 3.313 Å, b = 10.473 Å, and c = 4.374 Å [66]. Fig. 2.1(c) shows the top view of a single layer of bP. The crystallographic armchair and zigzag directions are indicated, with reference to the unit cell directions.

Black Phosphorus was first prepared by Bridgman in 1914 [21], by applying a pressure of $\sim$ 12000 bar to white phosphorus at 200 °C. Subsequent experiments demonstrated that bP is thermodynamically more stable than other allotropes of phosphorus [67, 68]. Electrically, bulk bP is an intrinsically p-type doped semiconductor with a high hole mobility of $\sim$200 cm^2/V·s at room temperature [22]. Research on bulk bP remained steady in following decades, unraveling its structural [23, 24], optical [21, 25–27], phonon [29, 69, 70], superconducting [30, 31] and electrical [22, 25, 28, 29, 71] properties. However, these early works on bP did not attracted much attention probably due to the dominant role of silicon.

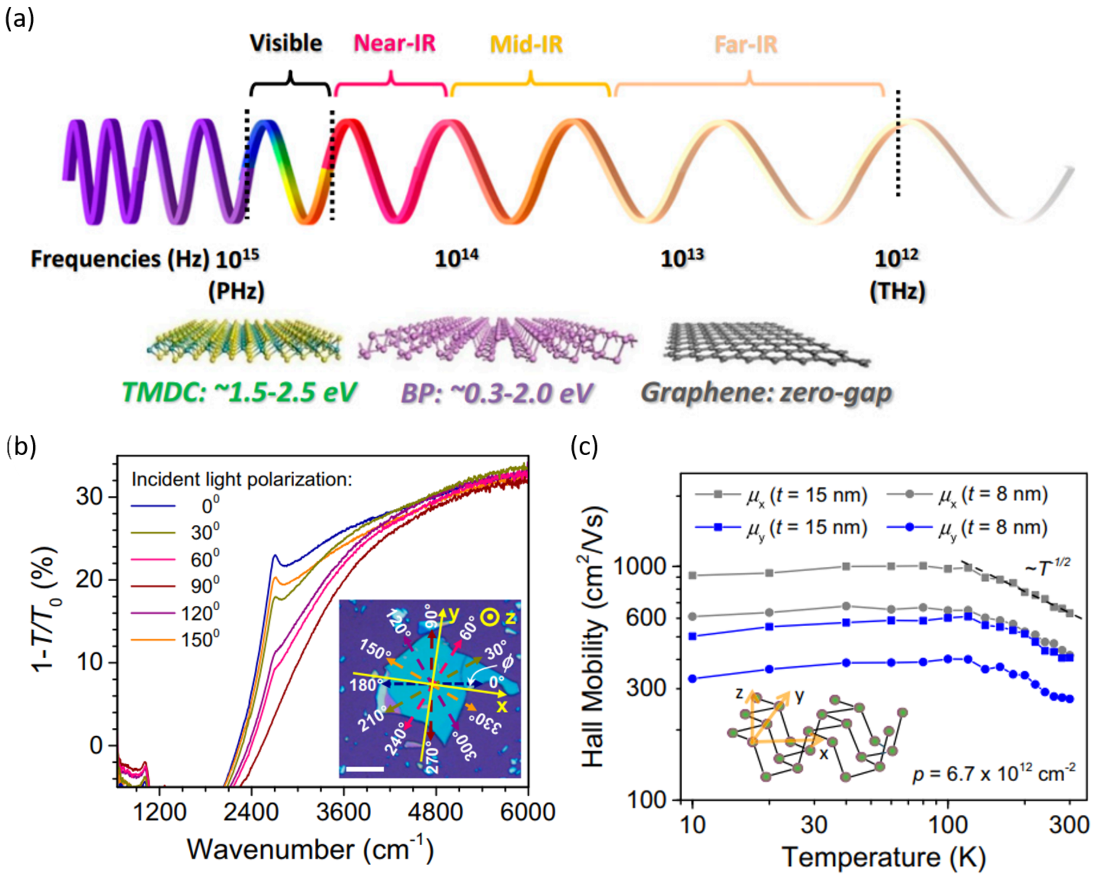

FIGURE 2.3 Marvelous bP properties. (a) Band gap of bP is shown, lying between zero band gap graphene and high band gap TMDCs. (b) Polarization-resolved infrared relative extinction spectra of bP thin film. The directions of light polarization are indicated in inset, which shows an optical micrograph of around 30 nm thick bP flake (scale bar: 20 μm). (c) Anisotropy in hall mobility measurement. μ_x is 1.8 times larger than μ_y. (a) is reproduced from ref. [52]. (b) and (c) are adapted from ref. [53].

With the realization of graphene in 2004 by Novosolov and Geim [32], for which they were awarded the Nobel prize in 2010, a new field of research started in materials science: the field of van der Waals materials. In an attempt to discover other such materials similar to graphene, bP got a renewed interest because of its layered crystal structure, where layers are weakly bonded by van der Waals forces, similar to graphite. Realization of phosphorene, a single layer of black phosphorus, by exfoliating bP crystals marked its entry into the family of van der Waals materials in 2014 [48, 49]. Since then, many research efforts have been focussed to explore band structure [51, 72, 73], strain [55, 74–79], defects [80], and intercalation [81] in bP. New studies probing novel physical properties [82] and characterization methods [83–85] as well as applications related to electronic [48, 50, 53, 56, 57, 86–88], photonic [58–60, 89–92], thermoelectric [61, 62], and anisotropic [93–95] properties of bP have been reported. Different structural varieties of bP like blue phosphorus [96], phosphorus nanotubes [97], phosphorus nanoribbons [98–102], stacked bilayer phosphorus [103], and hybrid structures of

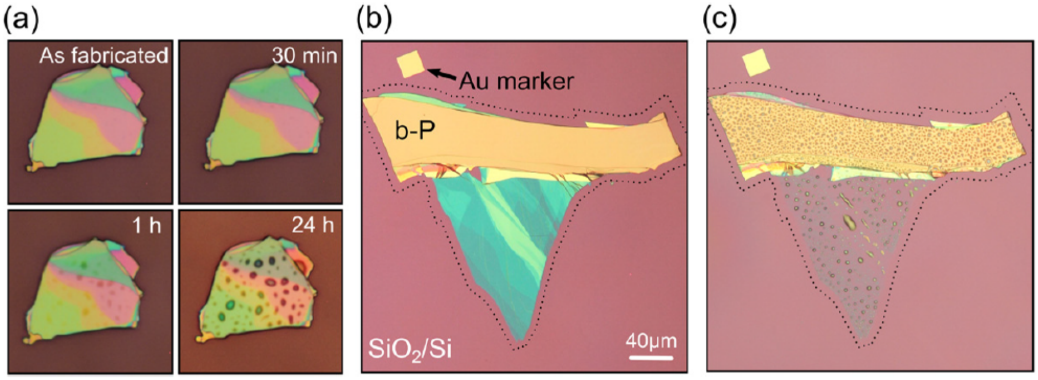

FIGURE 2.4 Optical microscopy images showing bP degradation on exposure to air. (a) Exposed for 30 min, 1 hour and 24 hours. Droplet-like structure become visible just after 1 hour of exposure. (b) Freshly prepared sample, and (c) exposed for 2 weeks – flake almost disappeared [49].

bP and other 2D materials [89, 100] have also been investigated. The recent boom in bP research can be seen in the graph shown in Fig. 2.2, which shows the sudden increase after 2014 in the number of publications which mentioned the words 'black phosphorus' or 'phosphorene'.

As a result of renewed interest in this material, many interesting properties have been discovered in bP. bP is intrinsically p-doped [22]. Kiraly *et al.* [64] have performed an STM investigation of bP and related its intrinsic p-type doped to atomic vacancies. In the bulk, it has a direct band gap of ∼0.3 eV, which can be tuned to ∼2.0 eV by decreasing the number of layers to single monolayer bP [50, 51]. With this value of band gap, it occupies a very important position among the 2D materials, filling the void between zero band gap graphene and high band gap transition metal dichalcogenides (TMDCs) [52], as shown in Fig. 2.3(a). The crystallographic anisotropy of bP also results in many interesting properties, imparting anisotropy to optical properties and carrier mobility, as shown in Fig. 2.3(b) and (c), respectively [53]. A theoretical simulation has predicted bP to have the direction of maximum thermal conductivity orthogonal to the direction of maximum electrical conductivity [55]. This orthogonality in the prominent electronic transport direction (armchair) and the prominent heat transport direction (zigzag) could significantly improve the efficiency of thermoelectric devices and give an interesting turn in the field.

However, even being the most stable allotrope of phosphorus, bP is a very reactive material. It shows thickness dependent surface instability in air because of the combined effect of water, oxygen, and light [104–106]. A study by Castellanos-Gomez *et al.* [49] shows the degradation of a bP flake over time on exposure to ambient atmosphere, as shown in Fig. 2.4. This constitutes a major challenge for the use of bP in practical device application. So, an investigation of bP surfaces to thoroughly understand its properties

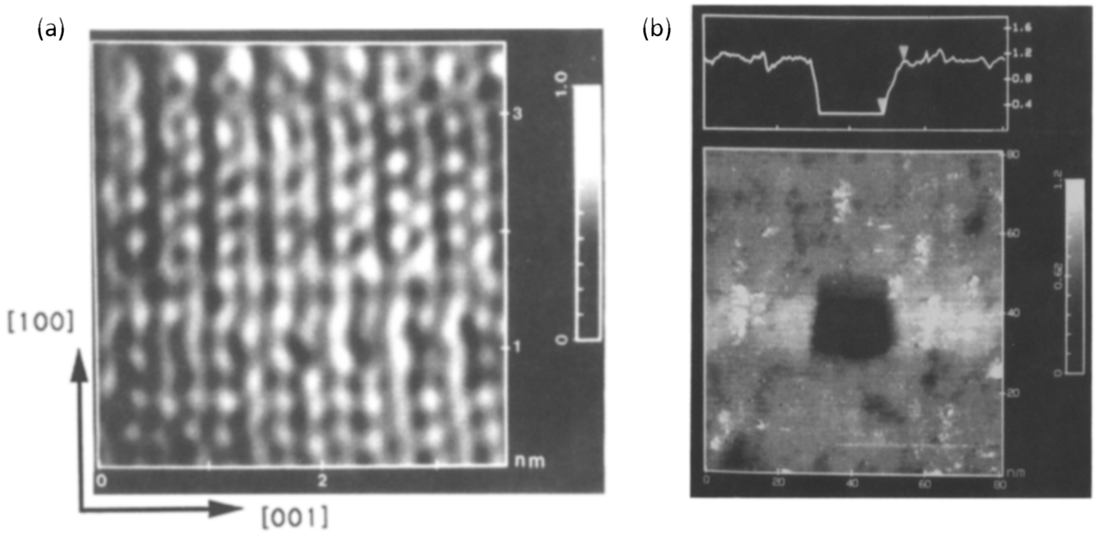

FIGURE 2.5 First STM on bP. (a) First atomic resolution of bP surface. The zigzag rows corresponding to phosphorus atoms in the upper plane can be recognized along [100] direction. Scanning parameters: (0.02 V, 5 nA). (b) 80 nm × 80 nm STM images of bP showing a 20 nm × 20 nm pit formed on bP by scanning for 2 min at (0.2 V, 1 nA) while bP was exposed to air. The height profile across the pit shown at the top of the image shows that the pit is 1 nm deep. Adapted from ref [107].

is very important. Also, if seen from a 2D material application point of view, a 2D materials is essentially just a surface. And so it is extremely important to study bP surfaces well, to make way for future developments for practical applications of single layers of bP.

2.2 bP surface characterization by STM

The first scanning tunneling microscopy investigation of the bP surface was performed in 1992 by the group of Yau *et al.* [107]. They studied a bP crystal exposed to ambient air while scanning, and measured atomic resolution on bP for the first time. Figure 2.5(a) shows the zigzag rows of phosphorus atoms lying in the upper plane of the top layer of bP. However, due to bP degradation in ambient air, the bP surface was getting oxidized very quickly. The presence of oxygen and water also induced a chemical reaction with the tip, causing an etching of the bP surface while being scanned. This is shown in Fig. 2.5(b) where a pit can be seen produced by scanning for 2 minutes.

Realizing the need of clean environment to preserve bP surfaces, later experiments to investigate bP were carried out in ultrahigh vacuum (UHV). A study by Zhang *et al.* [108] shows a more stable and clear STM image of the bP surface obtained by cleaving a bulk crystal measured and at 4.3 K, as shown in Fig. 2.6(a). Individual atoms lying in the upper plane of the bP surface can be clearly identified. Zhang *et al.* [108] also performed

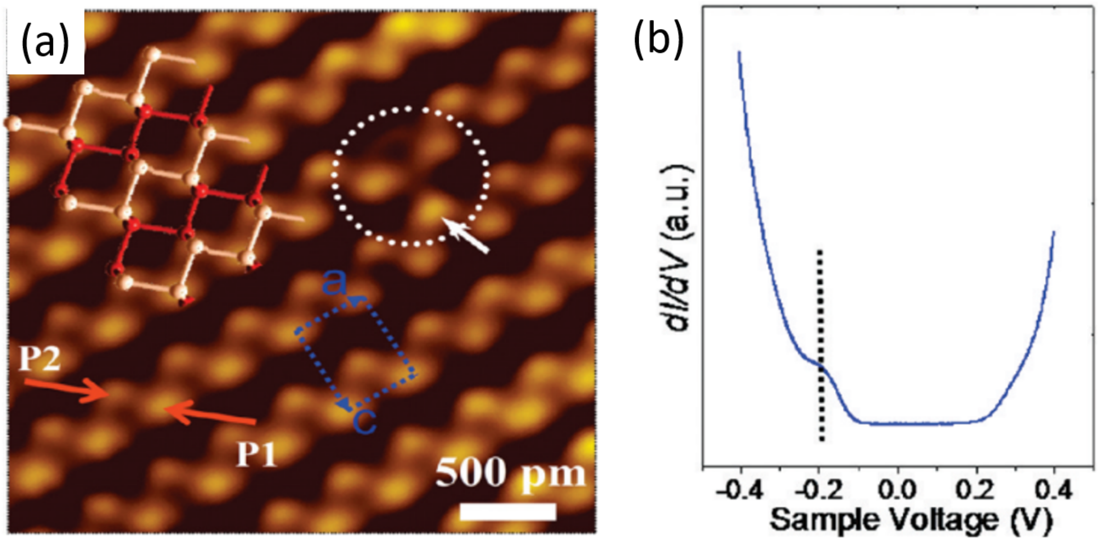

FIGURE 2.6 STM inside UHV. (a) Atomic resoltion of bP surface achieved in UHV at 4.3 K. A schematics of bP crystal structure is also shown. Only the phosphorus atoms lying in the upper plane of top layer of bP, indicated in white in the schematics, are visible in a STM image. These atoms form rows of zigzag chains, as seen in the measured image. A blue dashed rectangle indicating unit cell and a white dashed circle indicating a phosphorus vacancy are also shown. Scanning parameters: (-1.3 V, 0.157 nA). (b) Differential conductance measurement showing a band gap of ∼0.4 eV and a surface state at -0.17 eV. Adapted from ref. [108].

spectroscopic measurements showing a band gap of 0.3 eV, as shown in Fig. 2.6(b). Several other works have also reported STM investigations of high quality, with measured unit cell parameters and band gap values consistent with previously reported values [64, 109]. Other aspects important for the bP surface like single atomic vacancies, impurities, and hydrogenation and phosphorization of oxygenated bP have also been explored using STM [64, 110–112]. A recent work has investigated exfoliated thin flakes of bP using STM [113]. Liu *et al.* have shown an atomic resolution image of the surface of a thin bP flake, but the main part of the report focussed on spectroscopic and transport properties of these thin bP flakes for giant Stark effect investigations.

2.3 bP surface desorption

Even though there are no reports of STM investigations of the temperature-dependent surface behavior of bP, two experiments have been reported which evaluate this behavior using other characterization techniques. A work by Liu *et al.* [114] from 2015 studied exfoliated bP surface degradation with temperature using scanning and transmission electron microscopy measurements. They observed that thin bP flakes start desorbing in vacuum at ∼400 °C, in contrast to the 550 °C reported earlier for bulk bP. The decomposition initiates via anisotropic eye-shaped craters and proceeds by enlargement

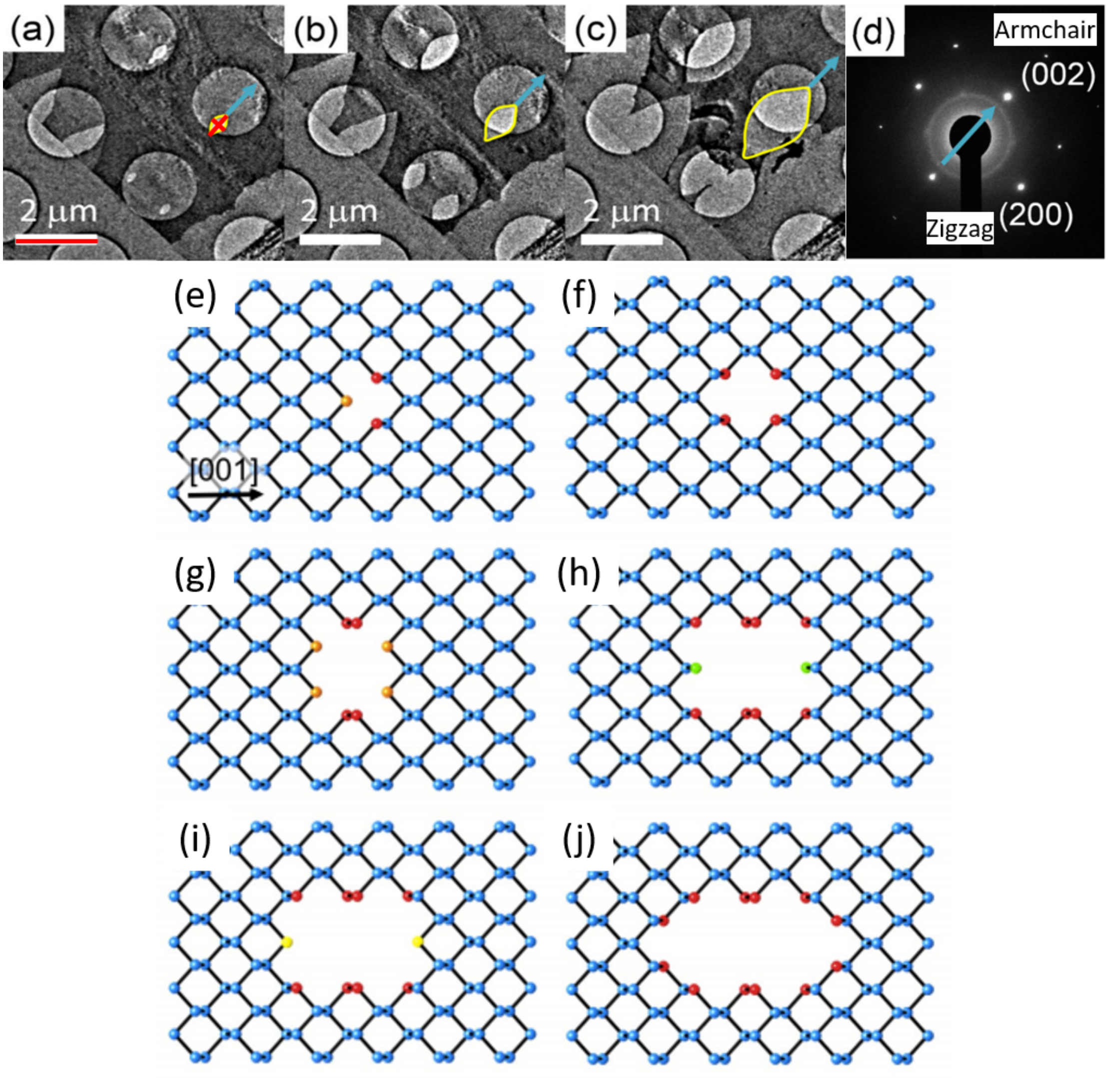

FIGURE 2.7 Craters aligned along the armchair direction. Eye shaped crater formation and growth on annealing at 400 °C for 5, 8, and 12 minutes shown in (a), (b), and (c) respectively. (d) Selective area diffraction (SAD) pattern showing the alignment of eye-shaped craters along the armchair direction. (e)-(j) Model illustrating crack propagation by sublimation of unsaturated P atoms, leading to anisotropic crater aligned along the armchair direction. Adapted from ref. [114].

of these craters. Figures 2.7(a), (b), and (c) shows such a process measured on a flake heated at 400 °C for 5, 8, and 12 minutes, respectively. The smallest crater shown in Fig. 2.7(a) has a dimension of about 650 nm × 400 nm, measured using the scale in the image. A selective area diffraction (SAD) measurement, as shown in Fig. 2.7(d), was performed to determine the direction of the long axis of these craters relative to the crystallographic directions of bP. Liu *et al.* [114] report that the long axis of anisotropic craters aligns along the armchair direction.

To understand the mechanism underlying the formation of these anisotropic craters, Liu *et al.* [114] performed a simplistic modeling, as shown in Figs. 2.7(e)-(j). They

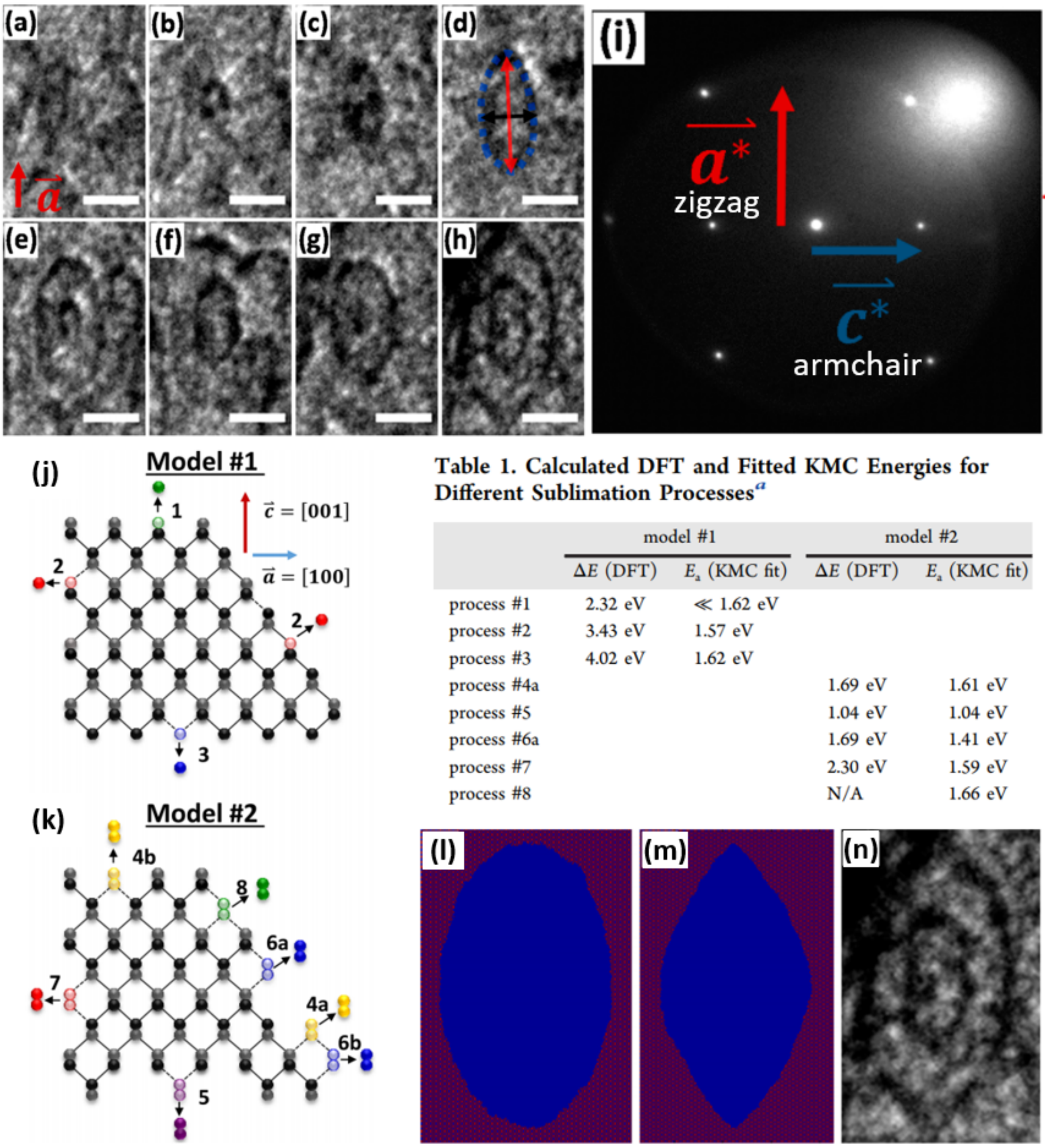

Table 1. Calculated DFT and Fitted KMC Energies for Different Sublimation Processes[a]

	model #1		model #2	
	ΔE (DFT)	E_a (KMC fit)	ΔE (DFT)	E_a (KMC fit)
process #1	2.32 eV	≪ 1.62 eV		
process #2	3.43 eV	1.57 eV		
process #3	4.02 eV	1.62 eV		
process #4a			1.69 eV	1.61 eV
process #5			1.04 eV	1.04 eV
process #6a			1.69 eV	1.41 eV
process #7			2.30 eV	1.59 eV
process #8			N/A	1.66 eV

FIGURE 2.8 Craters aligned along the zigzag direction. (a)-(h) Bright-field LEEM snapshots showing anisotropic hole expansion recorded at an interval of 2 seconds at 486 °C, 488 °C, 490 °C, 491 °C, 493 °C, 495 °C, 497 °C, and 499 °C, respectively. (i) LEED pattern identifying the crystallographic direction of bP, and indicating an alignment of elongated craters along the zigzag direction. Schematics showing different configurations of (j) atomic P desorption, and (k) molecular P_2 desorption for which activation energies are calculated using DFT. The calculated values are shown in Table 1. Results obtained from KMC simulations for the removal of 10^6 atoms to form craters by (l) atomic P desorption mechanism, and (m) molecular P_2 desorption mechanism, compared with the experimental result shown in (n). Adapted from ref. [115].

started from a single phosphorus vacancy shown in Fig. 2.7(e). Due to this vacancy, three P atoms which were bonded directly to the atom at the vacancy site, have become unsaturated[1]. Regular P atoms are indicated in blue in Fig. 2.7, and unsaturated P atoms are indicated in colors other than blue. There are three kinds of unsaturated P atoms that can be formed on a bP surface: (a) P atoms with only one bond, bonded with only one other P atom (green), (b) P atoms with two bonds, bonded with two other P atoms, both lying in the same plane (orange and yellow), and (c) P atoms with two bonds, bonded with two other P atoms, lying in different planes (red). Liu *et al.* [114] assume the order of removal of these unsaturated P atoms as: (a) desorb first, then (b), and finally (c). This leads to the formation of an anisotropic crater starting from a single atomic vacancy, with the crater aligned along the armchair direction.

A second study investigating the desorption of phosphorus from the surface of bP has been reported by Fortin-Deschenes *et al.* [115] in 2016. They have observed the formation of similar elongated craters on exfoliated thin bP flakes above (375 ± 20) °C using low energy electron microscopy (LEEM). The desorption initiates via anisotropic eye-shaped craters and proceeds by enlargement of these craters. Figures 2.8(a)-(h) show such a process. The crater marked in Fig. 2.8(d) has a dimension of about 400 nm × 200 nm, measured using the scale in the image, which is of same order as compared to the craters reported by Liu *et al.* [114]. A low energy electron diffraction (LEED) measurement was performed by Fortin-Deschenes *et al.* [115] to determine the long axis of these craters relative to the crystallographic directions of bP, which revealed that the long axis of these anisotropic craters aligns along the zigzag direction, as shown in Fig. 2.8(i). This result is inconsistent with the result of Liu *et al.* [114].

To understand the mechanism underlying the formation of these anisotropic craters, Fortin-Deschenes *et al.* [115] calculated the activation energies for the removal of P and P_2 in different configurations from bP nanoribbons using density functional theory (DFT) calculations. Figures. 2.8(j)-(k) show different configurations of P and P_2 removal, and Table 1 in Fig. 2.8 shows the computed values of activation energies for these processes. These computed activation energies were used in a kinetic Monte Carlo (KMC) simulation of crater formation by removal of 10^6 atoms. The results obtained from kinetic Monte-Carlo (KMC) simulations is shown in Fig. 2.8(l) for atomic P desorption and in Fig. 2.8(m) for molecular P_2 desorption. Fig. 2.8(n) shows an enlarged image of a measured crater for comparison to the results obtained from simulations. The simulated result for P_2 desorption gives craters with sharp tips, more similar to the ones measured. Also, the activation energies calculated using DFT for P desorption are

---

[1] A regular P atom on the bP surface forms three bonds, one each with three other P atoms. An unsaturated P atom is one which is bonded to less than three other P atoms, forming less than three usual bonds, which leaves one or more bond of this P atom unsaturated.

significantly higher than those for P_2 desorption. Thus, Fortin-Deschenes *et al.* [115] conclude that the preferred mechanism for crater formation is P_2 desorption. The results reported by Liu *et al.* [114] and by Fortin-Deschenes *et al.* [115] do not agree with each other and leave the debate of the layer-by-layer desorption of bP as an open field.

2.4 bP doping studies

Doping is an important technique in standard semiconductor industries used to tailor the electronic properties of intrinsic semiconductors. Some impurities are intentionally added to the crystal lattice sites of bulk semiconductors which modulates its electrical, optical and structural properties. This is called substitutional doping. In 2D materials, doping can be achieved by several other means also, like gating, in which an applied bias to the gate modulates the charge carrier density in the material. Transfer doping is another way to dope a 2D semiconductor, in which the impurities are introduced through physical or chemical adsorption on the surface of the 2D semiconductor, resulting in a transfer of electrons at the surface. A material with relatively higher tendency to accept electrons causes p-type doping, while those with relatively higher tendency to donate electrons cause n-type doping to the 2D semiconductor.

With high mobility and favorable band gap, bP is seen as a promising candidate for future electronic devices. Therefore, several theoretical works have been reported focusing on doping of bP. A detailed theoretical DFT calculation has predicted the behavior of a range of elements substitutionally doped in phosphorene [116]. First studying the role of a single atomic vacancy, their calculation indicates that a missing P atom causes p-type doping. On substitution, Au, Pt, C, O, S, F, and I cause p-type doping, while Li, Na, Ag, Pd, Fe, Co, Ni, Pb, Al, and Bi cause n-type doping. Out of these, C causes the strongest p-type doping, and Bi the strongest n-type doping. Another theoretical study has investigated using DFT calculations the effective doping of monolayer phosphorene by surface adsorption of 27 different adatom species and predicted the following materials to cause p-type doping: Pd, Ga, Al, In, Si, Cu, Pt, F, Br, Ge, O, Cl, S, Sn, Au, Ag, and As; and the following materials to cause n-type doping: K, Na, Mg, Ca, Ti, Ni, N, Li, Fe, and C, in decreasing order of effective charge transfer [117].

Experimental investigations of substitutionally doped bP using several materials have been reported. Akahama *et al.* [22] in 1983 reported an investigation of bulk bP substitutionally doped with Te. They reported p-type conduction in pristine undoped bP with effective acceptor concentration of $2-5\times\ 10^{15}$ cm^{-3}, and n-type behavior in tellurium-doped bP, with effective donor concentration of $2-3\times\ 10^{16}$ cm^{-3}. A recent experiment by Yang *et al.* [118] investigating 7 nm and 9 nm thin flakes of substitutionally doped

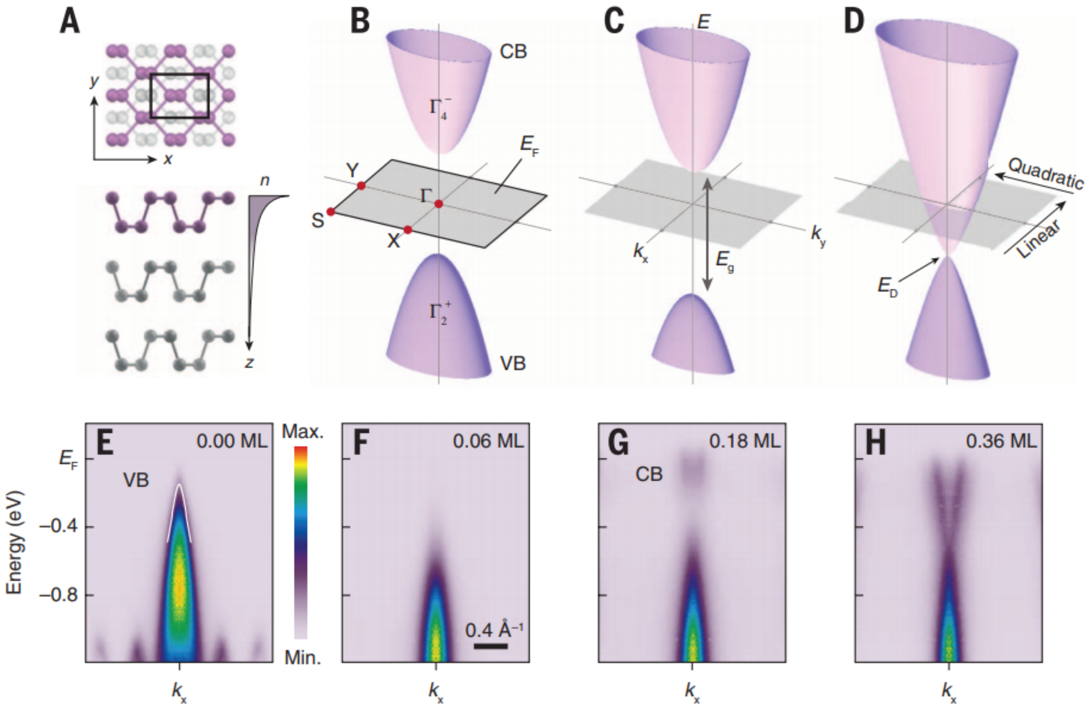

FIGURE 2.9 ARPES study of potassium doping on bP. (a) A Schematics of bP crystal. Band structure of (b) pristine bP, (c) bP in initial stages of potassium doping and (d) bP with higher potassium doping. Experimentally measured band structure using ARPES at 15 K of bP with increasing amount of potassium. Band gap increases initially for lower amount of potassium while at higher amount of potassium, it becomes a zero-gap semimetal. It also shows an n-type doping caused by potassium. Adapted from ref. [120].

bP with tellurium, has observed p-type behavior even in tellurium-doped bP, in contrast to the reported transformation of bP from p-type to n-type by doping with tellurium reported in the former work. Xu *et al.* [119] studied substitutional doping of bP by selenium. They have grown centimeter-scale selenium doped bP crystals with controllable doping contents using a mineralizer-assisted gas-phase transformation method and prepared field effect transistors (FETs) after exfoliating these bP crystals for their electrical characterization. They found that selenium-doped bP devices exhibit p-type behavior.

Recently some works have focused on surface transfer doping of bP. Sanna *et al.* [121] investigated transfer doping on bP by lithium. They have evaporated ∼1/8 ML of lithium on bulk bP cleaved *in-situ* and studied its influence on the band gap of bP by angle-resolved photoemission spectroscopy (ARPES) measurements. They found that lithium causes a strong n-type doping of the surface of bulk bP. It moves the Fermi level into the conduction band and causes the metallization of the bP surface.

Kim *et al.* [120] investigated transfer doping of bP by potassium. They have evaporated potassium on bulk bP cleaved *in-situ* in increasing amounts and observed its effect on the bP band gap using ARPES measurements at 15 K. For low potassium deposition of 0.06

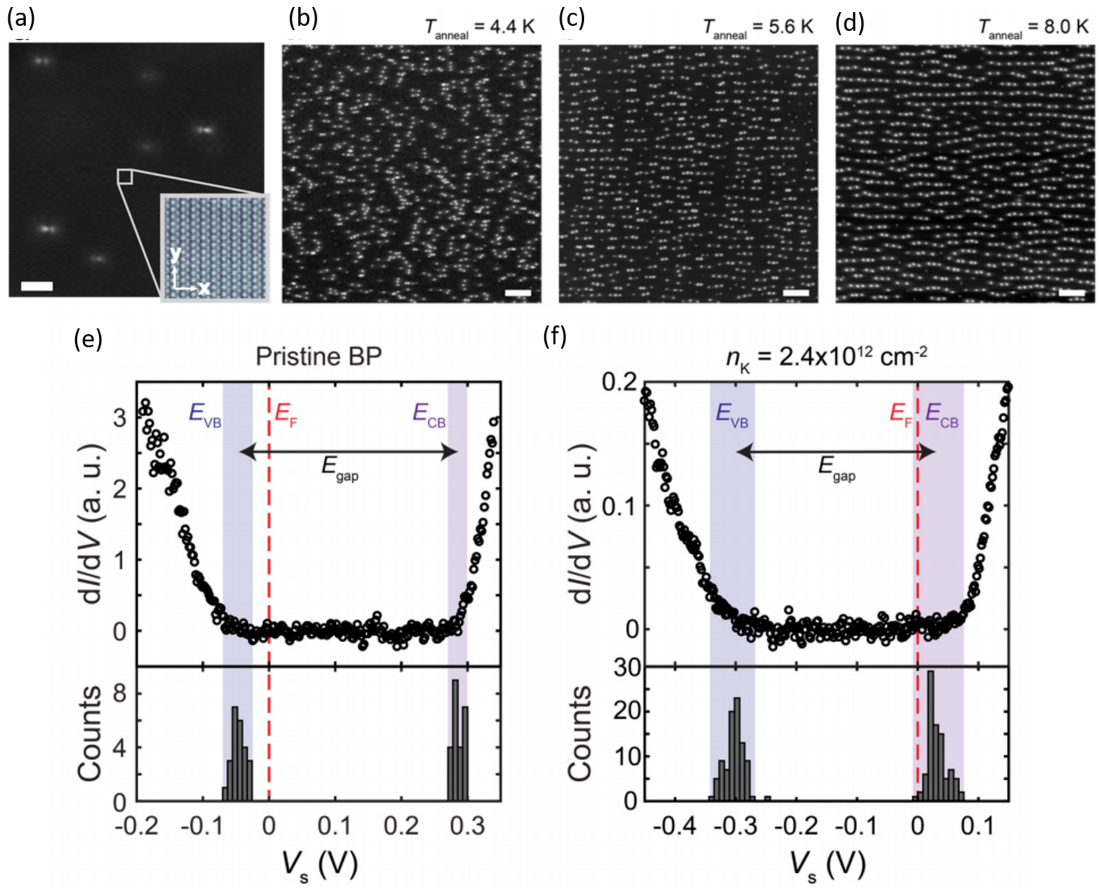

FIGURE 2.10 STM study of potassium doping on bP. (a) Pristine bP surface with atomic resolution shown in inset. Scanning parameters: (-0.4 V, 0.02 nA), scale bar: 10nm. (b)STM image of bP measured at 4.4 K with potassium deposited at 4.4 K. STM images of bP measured at 4.4 K with potassium deposited at 4.4 K and annealed at (c) 5.6 K, and (d) 8.0 K. Scanning parameters: (-1.0 V, 0.003 nA), scale bar: 20nm. The potassium atoms align along armchair direction on annealing to 5.6 K. STS measurement showing (e) p-type doping in pristine bP, and (f) n-type doping in potassium doped bP. Adapted from ref. [122].

ML, they observed a slight n-type doping and band gap broadening, resulting in a band gap of ∼0.6 eV. However, with increasing potassium amount, they observed a band gap closing, such that at 0.36 ML of potassium, the conduction band and the valence band crossed, causing a semiconductor-semimetal transition, as shown in Figs. 2.9. Apart from a trivial shift in the Fermi level, they also observed a significant band structure modification caused by doping.

Kiraly *et al.* [122] recently reported an STM investigation of transfer doping of potassium on bP at 4.4 K, as shown in Fig. 2.10. They deposited potassium using a SAES getter source on bulk bP cleaved *in-situ*. For an amount of potassium deposition thousand times lower than in the former study by Kim *et al.* [120], they reported an n-type doping of bP, based on scanning tunneling spectroscopy measurements and ARPES. They have also studied the morphology of potassium on the bP surface and found that

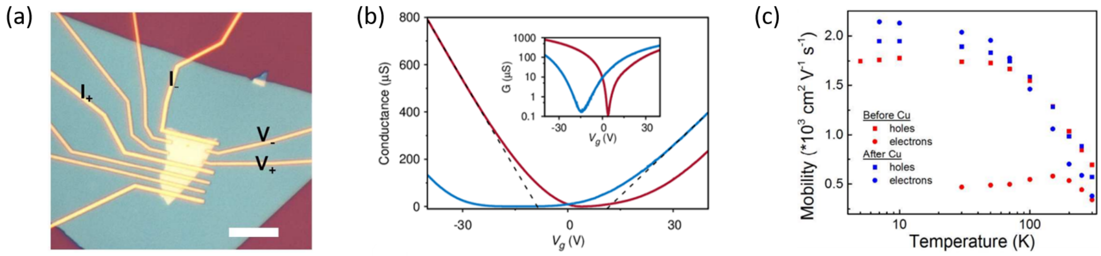

FIGURE 2.11 Transport study of copper doping on bP. (a) Optical image of FET device with 10 nm bP flake on hBN. Scale bar: 10 μm. (b) Four-point conductance versus gate voltage at room temperature before (red) and after (blue) copper doping. The inset shows the same data on a logarithmic scale. Copper causes an n-type doping. (c) Electron and hole mobilities before and after copper doping. Presence of copper does not degrades the transport properties. Adapted from ref. [65].

potassium adatoms have a lower diffusion barrier along the zigzag direction than along armchair direction. Kiraly *et al.* also found that the potassium atoms tend to align along the armchair direction.

Koenig *et al.* [65] investigated transfer doping on bP by copper. They deposited copper in a DC sputtering system on exfoliated bP flakes. They fabricated field effect transistors (FETs) from these flakes and studied the influence of the copper deposition on the band structure of bP using transport measurements at room temperature and low temperature (5 K), as shown in Fig. 2.11. They observed that copper causes n-type doping to bP and also noticed that doping by copper does not degrade the transport properties of the bP devices.

2.5 Discussion

bP has been revived as a material of significant importance after the emergence of the field of 2D materials due to its direct band gap, its layer dependent band gap tunability, and its anisotropic properties. The high surface reactivity of bP poses a major drawback for research and practical applications of bP, but on the other hand it encourages surface investigations to obtain a proper understanding of the surface properties of bP. Several studies have reported surface investigations of bP using STM, showing atomic resolution on the bP surface. Some other aspects of bP surfaces has also been explored in these studies, like defects, vacancies, hydrogenation, phosphorization, and spectroscopy on surfaces of bP. However, most of these studies used surfaces of bulk bP cleaved *in-situ* to conduct such investigations, rather than few layer thin bP flakes. The prime reason behind this is the high reactivity of the bP surface, which makes it very difficult to prepare exfoliated bP flakes with a clean surface. The thinner flakes are more reactive and degrade very quickly, because of which works on thin flakes of bP are mostly investigated by transport or optical measurements, after capping the bP surface by PMMA or other materials to protect the bP surface. But 2D applications require more surface investigations of thin bP flake samples. A recent study reported STM on exfoliated thin bP flakes, but their investigation focused on transport and spectroscopic aspects, not on surface morphology.

The evolution in surface morphology with temperature is another important aspect that needs to be understood, since device processing requires high temperature treatments. Two experiments have been reported which studied such a behavior of thin bP flakes by electron microscopy. Both have observed initiation of phosphorus desorption at $\sim$400 °C leading to anisotropic craters on the bP surface. These craters have been observed to be aligned along the crystallographic armchair direction by one group and along the crystallographic zigzag direction by the other group, both based on diffraction data. Also, the mechanism behind the formation of these craters as presented by the two groups is contradictory to each other. The former group reports atomic phosphorus desorption while the latter group reports molecular P_2 desorption. So, there exists a debate in literature regarding the understanding of crater formation. An STM investigation of such craters with atomic resolution could resolve this debate. Also the surface morphology behavior presented in both studies lacks the high resolution provided by STM.

Substitutional and transfer doping of bP has attracted a huge interest. These topics were investigated especially in transport and ARPES measurements. Substitutional doping of bulk bP and exfoliated bP with tellurium has resulted in n-type and p-type doping, respectively, which indicates that bulk and exfoliated bP behave differently to doping. Transfer doping of exfoliated bP by potassium has shown that the presence of doping does not only cause a Fermi level shift, but also significant changes in band structure of bP, like band gap opening and closing with increasing amount of potassium. Another work on transfer doping by potassium of bulk bP cleaved *in-situ* has studied surface morphology of potassium adatoms on the bP surface and observed that the preferential direction for diffusion of potassium atoms on bP is along the zigzag direction, while they tend to align along the armchair direction. A recent work studying transfer doping of exfoliated bP by copper using transport measurements has found that copper causes an n-type doping of bP. They have also observed that doping by copper does not degrade the electronic properties of bP. But an understanding of the morphology of copper on bP surfaces is still missing. An STM study, like the one performed for potassium deposited on bP, can provide the morphology study of copper deposited on bP and complement the transport studies. Furthermore, scanning tunneling spectroscopy can provide an understanding of the doping induced by copper at the atomic level.

Chapter 3

Methods

Thorough understanding and reproducibility are the keys to progress in science. Keeping these aspects in mind, in this chapter we discuss the details of the processes performed during the experiments, in order to make the reader understand each aspect of the experiment more clearly, and also to facilitate reproducing the work if necessary.

3.1 Scanning Tunneling Microscopy (STM)

3.1.1 STM basics

The technique of scanning tunneling microscopy was invented by Gerd Binning and Heinrich Rohrer in 1981 at IBM Zurich, for which they were awarded the Nobel prize in 1986. As the name indicates, a scanning tunneling microscope uses the principle of quantum tunneling [123], in which a tunneling current flows between tip and sample when they are brought to close proximity. A metallic tip is gradually brought very close to the sample surface, with a potential difference applied between the tip and the sample. The movement of the tip is driven by a piezoelectric motor and controlled by a feedback loop which depends on the current between tip and sample. When the tip is far away from the sample surface, no current is detected, since the circuit is open, and so the tip keeps moving towards the sample in nanometer steps. Once it reaches within Angstrom distance to the surface, a current is detected. This current is due to the electrons tunneling across the vacuum potential barrier, thus completing the circuit which causes the feedback loop to stop any further tip advancement. Then the tip is scanned over the sample parallel to the surface. In constant height mode of STM scanning, the tunneling current collected at different points during scanning gives the information regarding the surface. On the other hand, in constant height mode of STM

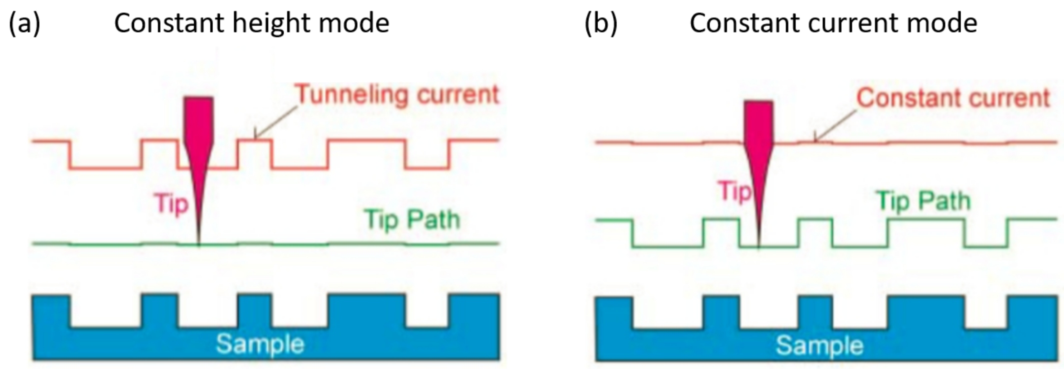

Figure 3.1 Schematics showing different STM scanning modes. (a) Constant height mode – tip moves horizontally at constant height from the sample, as indicated by the tip path. (b) Constant current mode – the feedback loop maintains a constant current so that the tip follows the surface morphology.

scanning, the tip is scanned with a particular voltage and current setpoint. The feedback loop monitors and adjusts the height of the tip from the surface to maintain the current constant. The resulting variation in height at different points on the surface gives the morphology information. The schematics in Fig. 3.1 illustrates the two modes of STM scanning.

With a lateral resolution of 0.1 nm and a depth resolution of 0.01 nm, individual atoms within a material can be imaged and manipulated using STM. This high resolution in STM is facilitated because of the exponential dependence of tunneling current I on the distance d between tip and sample [123]:

$$I \propto e^{-2\kappa d}, \tag{3.1}$$

where κ is a decay constant, which is ≈11.4 nm^{-1} for work function of 5 eV. The schematics shown in Fig. 3.2 illustrates the high resolution of STM. Figure 3.2(a) shows the exponential decay of tunneling current with increasing distance. Figure 3.2(b) illustrates that when the tip is positioned over an atom on the surface of the sample while scanning, the distance of the tip from that atom is slightly smaller than the distance of the tip from neighboring atoms. Due to this, the contribution to the tunneling current is almost entirely due to the closest atom and negligible from the neighboring atoms, which means that we collect signals from individual atoms at a time. Plotting the tunneling current against scanning coordinate enables visualization of the surface with atomic resolution, as shown in Fig. 3.2(c).

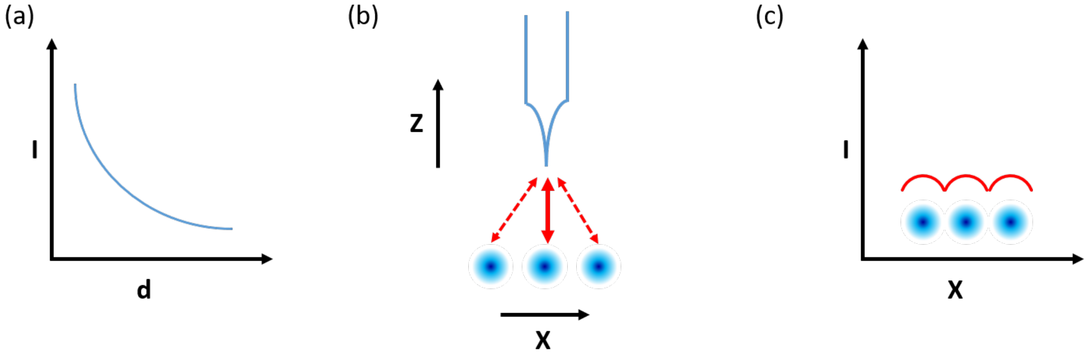

FIGURE 3.2 Schematics illustrating high resolution in STM due to tunneling. (a) Exponentially decreasing tunneling current with increasing distance between the tip and the sample. (b) Distance of the tip from the atom directly below it is only slightly smaller compared to the neighboring atoms. But because of exponential dependence, the tunneling current from the atom directly below it is much more than that from the neighboring atoms. (c) The red line shows the current collected by a tip moving in constant height mode. Plotting this current enables to differentiate between individual atoms and gives atomic resolution. In case of constant current mode, the red line would be the trajectory of tip in z-direction. Then plotting z would give the same atomic resolution.

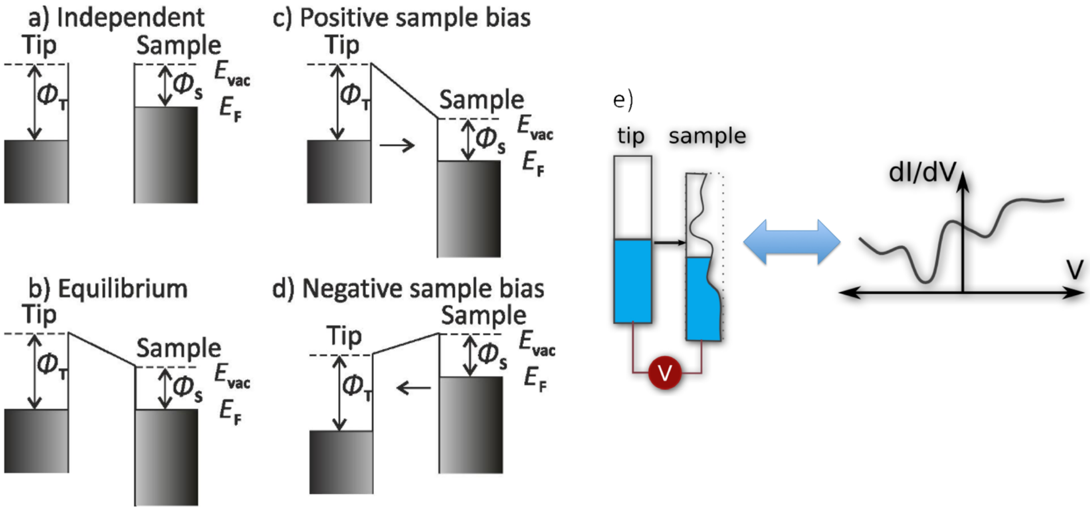

FIGURE 3.3 Schematics illustrating Scanning Tunneling Spectroscopy. Energy band diagram for the tip and the sample when: (a) the tip is far away from the sample and they are not intercating, (b) the tip is at small distance from the sample and they are at equilibrium, (c) a positive bias is applied to the sample, such that the electrons flow from the filled states of the tip to the empty states of the sample, and (d) a negative bias is applied to the sample, such that the electrons flow from the filled states of the sample to the empty states of the tip. The direction of flow of electron is also indicated by an arrow in (c) and (d). (e) A STS measurement in which voltage applied between the tip and the sample is swept. The density of states of a metallic tip is constant. So, the differential conductance represents the density of states of the sample. (a)-(d) adapted from ref. [124].

3.1.2 Fundamentals of Scanning Tunneling Spectroscopy

Scanning tunneling spectroscopy is another important measurement that can be carried out with the help of a STM. It is useful to understand the electronic structure of the sample. During this measurement, the scanning is stopped and the feedback is paused, such that the tip stays at a fixed distance from the sample, and then the voltage applied to the tip is swept. The changing current as a result of sweeping the voltage is recorded. Figure 3.3 shows a schematics of one such measurement. According to Bardeen's formalism, the tunneling current between tip and sample is given by [125, 126]:

$$I = \frac{2\pi e}{\hbar} \sum_{t,s} f(E_t)[1 - f(E_s + eV)] \mid M_{t,s} \mid^2 \delta(E_t - E_s), \tag{3.2}$$

where $f(E)$ is the Fermi function, $\mid M_{s,t} \mid$ is the tunneling matrix element between the states of the tip and the sample, and V is the applied bias voltage between tip and sample. Equation (3.2) essentially means that the tunneling current is the sum of individual tunneling events between the filled states, $f(E_t)$, of the tip and empty states of the sample in the energy range between E_s and $E_s + eV$, when a positive bias V is applied to the sample, and opposite for negative bias. Assuming small bias voltage and replacing the Fermi functions with step functions (for sharp cutoff at E_F between the filled and empty states) assuming low temperature, the equation is simplified to [123]:

$$I = \frac{4\pi e}{\hbar} \int_0^{eV} \mid M_{t,s} \mid^2 \rho_t(E_f(t) - eV + \epsilon)\rho_s(E_f(s) + \epsilon)\delta\epsilon, \tag{3.3}$$

where ρ is the density of states. Assuming constant matrix elements in the range of values measured, it can be further simplified to [125]

$$I \propto \int_0^{eV} \rho_t(E_f(t) - eV + \epsilon)\rho_s(E_f(s) + \epsilon)\delta\epsilon, \tag{3.4}$$

which shows that the tunneling current is proportional to the density of states of the sample and the tip. Thus, the differential conductance reads [123]:

$$\frac{dI}{dV} \propto \rho_t(E_f(t) - eV + \epsilon)\rho_s(E_f(s) + \epsilon)\delta\epsilon. \tag{3.5}$$

Assuming a constant density of states for the tip as shown in Fig. 3.3(e), which is true for the metals used to make tips, Equation (3.5) implies that the differential conductance is proportional to density of states of the sample, as illustrated in the schematics in Fig. 3.3(e).

Experimentally, this is measured directly using a lock-in amplifier. A small high frequency sinusoidal signal, V_{mod}, is superimposed to the DC voltage being swept while acquiring tunneling spectra. The modulation in sweeping voltage causes a sinusoidal response in the tunneling current being recorded. The lock-in then uses the modulation frequency to remove the noise from the signal. Dividing the output signal dI from lock-in by V_{mod} gives the differential conductance, dI/dV.

Figures 3.3(c) and (d) demonstrate that a positive bias applied to the sample (or a negative bias applied to the tip) corresponds to a signal due to empty states of the sample, while a negative bias applied to the sample (or a positive bias applied to the tip) corresponds to a signal due to filled states of the sample. In our system, the bias is applied to the tip. This means that a positive bias corresponds to filled states of the sample and a negative bias to empty states of the sample. So, when we investigate the differential conductance of bP, the signal at negative bias of the sweep corresponds to the conduction band of bP, and the signal at positive bias of the sweep corresponds to the valence band of bP.

3.1.3 The Omicron STM system

In our lab, we use an Omicron low temperature scanning tunneling microscope (LT-STM), as shown in Fig. 3.4. All our measurements have been performed using this system at room temperature. The STM head is placed in an ultra high vacuum (UHV) environment with pressure $\sim 10^{-10}$ mbar. An UHV environment is an integral part of surface science investigations. UHV is a vacuum regime with pressure lower than $\sim 10^{-9}$ mbar. A pressure of 10^{-9} mbar corresponds to a molecular density of $\sim 10^{-7}$ cm^{-3}, which requires ∼1 hour to form a monolayer of adsorbed gases on a clean surface with sticking coefficient of one at room temperature [127]. In our system with base pressure in 10^{-11} mbar range, it corresponds to a few days for which our sample surface remains clean. Such a condition is very important to keep the sample surface clean during studies. To achieve such a low pressure, the whole system is baked for 48 hours at 150 °C, being pumped simultaneously by continuously running scroll and turbo molecular pumps. This process is called bake-out. It helps with out-gassing of water vapor and other gases adsorbed on the surface of the chamber. After bake-out is over and the system is cooling down, ion pumps are started which helps in reaching the desired pressure of low $\sim 10^{-10}$ mbar.

As shown in Fig. 3.4, the system is equipped with a loadlock chamber, a preparation chamber, and an analysis chamber. The loadlock chamber is used to exchange samples and tips without breaking the vacuum in the main chambers. To insert a sample, it is first put into the loadlock chamber, which is then pumped with a turbo pump supported

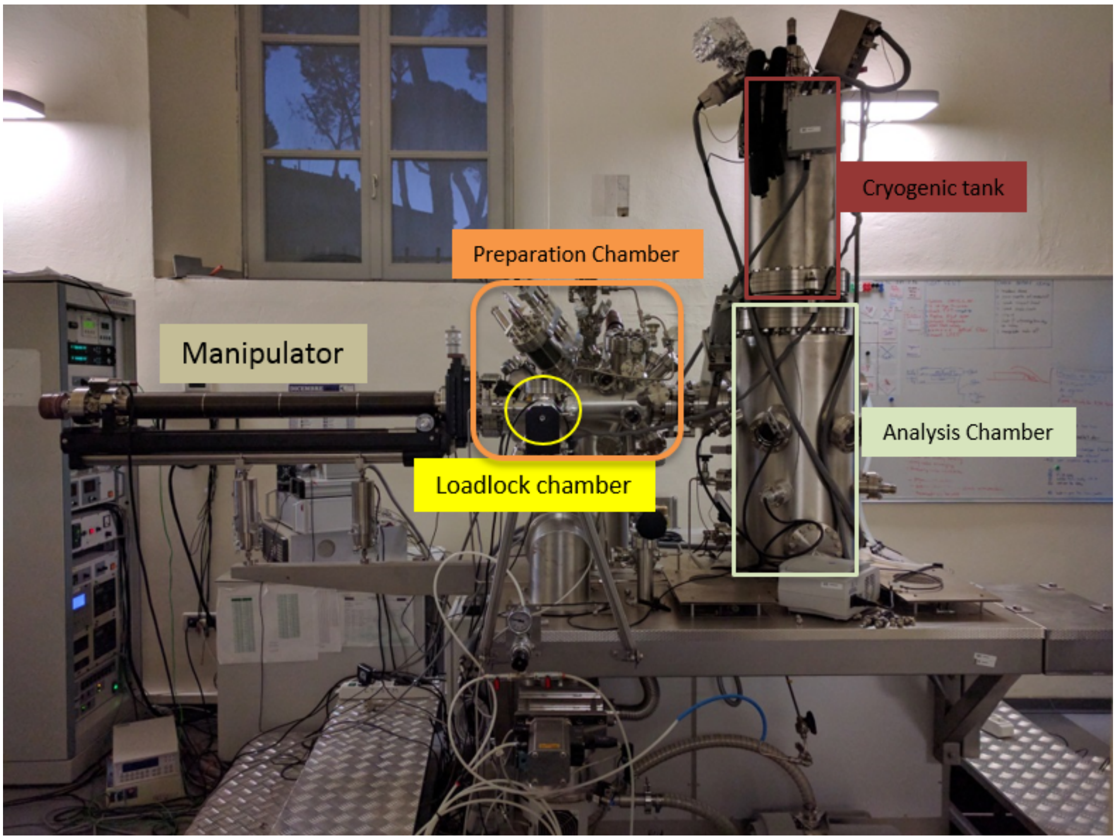

Figure 3.4 All STM measurements were performed on Omicron LT-STM system at room temperature. It has three chambers: loadlock chamber, preparation chamber and analysis chamber, indicated in the image. Loadlock chamber is used for inserting or taking out the sample or the tip. Preparation chamber is maintained at $\sim 10^{-10}$ mbar and is equipped with various tools like a metal evaporator, a sputter gun, a low energy electron diffraction (LEED) system, a residual gas analyzer, and an annealing stage, which is useful for in-situ processes on sample surfaces. Analysis chamber is maintained at $\sim 10^{-11}$ mbar and it hosts the STM head. All STM measurements are performed in this chamber.

by a scroll pump, until the pressure in the loadlock reaches below $\sim 10^{-7}$ mbar. Once it has reached the desired pressure, the sample is transferred onto the manipulator inside the preparation chamber. The preparation chamber and the analysis chamber are always maintained in UHV conditions using noise-free ion pumps and titanium sublimation pumps (TSPs). The preparation chamber is equipped with various tools like a metal evaporator, a sputter gun, a low energy electron diffraction (LEED) system, a residual gas analyzer, and an annealing stage, which is useful for in-situ processes on sample surfaces. The great advantage is that all these processes can be carried out on samples without breaking the vacuum, thus preventing the sample surface from getting exposed to air. This is even more important for investigating samples with highly reactive surfaces like bP. The annealing of bP samples was done in this chamber. One of the stages on the manipulator is equipped with a heating coil. It is also equipped with a thermocouple for temperature measurement. The current applied to the heater is controlled by a proportional integral derivative (PID) controller, using the temperature reading from the thermocouple to achieve and maintain the stage at a desired temperature. Copper evaporation is also performed in the same chamber, as discussed in detail in section 3.3.

After preparing the sample surface, the sample is transferred to the analysis chamber which hosts the STM head. The STM stage is then brought into a free position, suspended by a set of springs. This helps in minimizing the effect of mechanical noise of the surroundings on the tunneling signal. This is extremely necessary since the tip is within Angstrom range to the sample, and the tunneling current depends exponentially on the distance, and so even minute vibrations from the surrounding can cause huge alterations of the signal, or worse, a tip crash onto the sample surface.

3.2 Sample fabrication

The STM technique has certain requirements for the samples to be measured. It needs the substrate to be conductive so that the electrons tunneling between tip and sample can be drained. Since we will study exfoliated flakes, the substrate should be conductive, so that the electron tunneling to/from the tip does not charge up the flake. Furthermore, it helps if the substrate is flat, so that its roughness does not affect the surface of the flakes we are about to measure. In this section, we are going to discuss our approach towards fabricating samples which allow us to study the surface of exfoliated bP flakes by STM.

Silicon is a widely preferred choice worldwide as a substrate for fabricating devices made from exfoliated 2D materials. This is because of several factors. It has good mechanical and thermal stability even at high temperatures. Silicon wafers are cheap and readily available because of established large scale industrial production. The oxide of silicon, SiO_2, is a good insulator, which provides electric isolation to the devices. Finally, the processing methods like etching, sputtering, metal evaporation, and lithography are well developed for silicon.

However, in our case, the characterization technique to study the surface is STM. If the flakes of interest are put on an insulating surface, there would be no electrical channel for collecting the tunneling electrons, and the sample would charge up. That is why SiO_2, being an insulator, does not fulfill our requirements. A possible solution would be to fabricate a metallic contact to the flake to be scanned, which can collect the tunneling electrons. But this will require fabrication steps after bP exfoliation, like spin coating resists, such as poly(methyl methacrylate) (PMMA) and lithography,

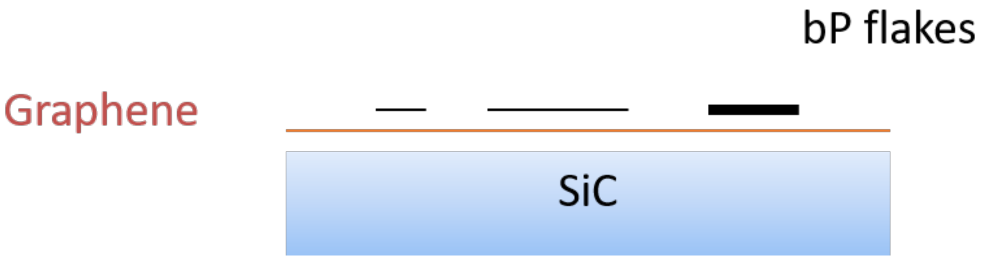

FIGURE 3.5 Schematics of a sample. First, epitaxial monolayer graphene is grown on silicon carbide. Then it is used as a substrate on which bP is exfoliated.

which would contaminate the surface of the sample. We preferred to work on flakes as clean as possible, which excluded processing steps involving resist. Furthermore, these fabrication steps would cause a lot of exposure of the sample to air. Since bP is very reactive, we aimed to reduce exposure of bP flakes to ambient air as much as possible.

For reasons that will be explained in the following, we have therefore decided to exfoliate bP on graphene on silicon carbide (SiC) as the substrate. A schematics of the sample is shown in Fig. 3.5.

3.2.1 Epitaxial monolayer graphene on silicon carbide

We used epitaxial monolayer graphene grown on the Si-face of 6H N-doped semiconducting SiC(0001) as a substrate on which we exfoliated bP flakes. Being conductive, graphene provides the required channel for the tunneling electrons to flow without the need of any fabrications steps. The flat graphene on $\sim$ 700-800 nm wide flat terraces of SiC provides a flat surface for bP flakes. And well established STM studies on graphene help to use the graphene substrate as a test sample. For example, if scanning on bP seems unreliable, we can scan the graphene next to the flake to check the tip quality.

Epitaxially grown monolayer graphene on SiC was provided by the group of Dr. C. Coletti at NEST, Pisa. The epitaxial monolayer graphene was obtained by annealing 6H-SiC(0001) samples in a high-temperature BM reactor (Aixtron) under argon atmosphere at about 1400 °C and 780 mbar. The epitaxial monolayer graphene on SiC thus prepared was annealed in the preparation chamber of the STM system in UHV overnight at 600 °C to clean the surface from oxides, water and residues from growth. Figure 3.6 shows a 10 μm × 10 μm image of monolayer graphene on SiC before and after annealing overnight at 600 °C. The clean surface thus obtained was used as the substrate for bP exfoliation.

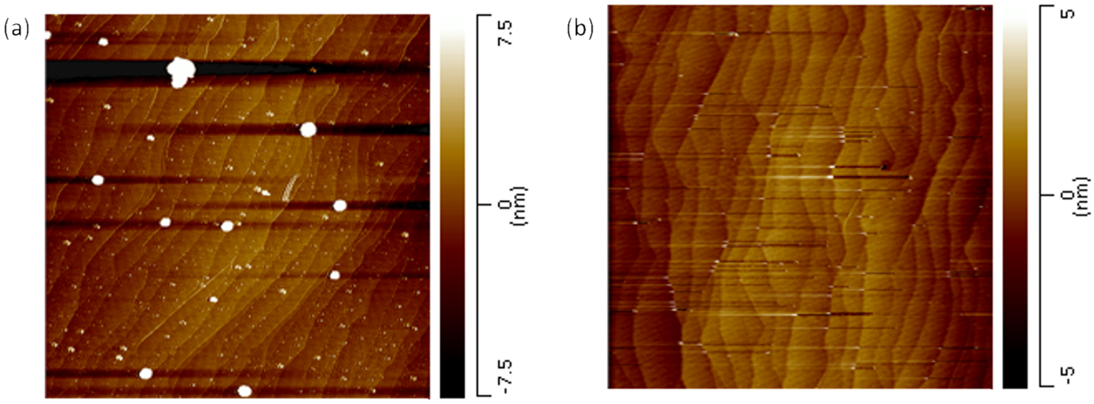

FIGURE 3.6 Substrate cleaning. 10 μm × 10 μm AFM images of monolayer graphene on SiC is shown (a) before annealing, and (b) after annealing overnight at 600 °C in UHV environment. The substrate looks much cleaner after annealing, suitable for bP exfoliation. Annealing is always performed just one night before new sample is prepared, which allows maximal clean substrate for bP exfoliation.

3.2.2 bP crystal growth

The crystals of bP used for exfoliation were grown by Dr. Manuel Serrano-Ruiz from Dr. Maurizio Peruzzini's group at CNR-ICCOM, Florence. The bP crystals were prepared by heating commercially-available red phosphorus ($> 99.99\%$) in a muffle oven, together with Sn ($> 99.999\%$), Au ($> 99.99\%$), and a catalytic amount of SnI_4, following a published procedure [128]: these solids were loaded into a quartz tube, which was then evacuated by a pumping procedure: the vacuum was backfilled by N_2 gas several times, and then the tube was sealed under vacuum. Then it was heated up to 406 °C (at a rate of 4.2 °C/min), kept for 2 hours at this temperature, and then heated up to 650 °C (2.2 °C/min). The sample was kept for three days at this temperature in the oven. Afterwards, a slow cooling rate was chosen (0.1 °C/min) to afford the formation of crystals of bP (typical size: 2 mm × 3 mm).

3.2.3 bP exfoliation

Even as the most stable allotrope of Phosphorus, bP is well known to be a very reactive material. A study by Castellanos-Gomez *et al.* [49] has shown that the exposure to atmosphere and light for less than an hour starts degrading the bP surface, as shown in Fig. 2.4. This makes it very difficult to prepare thin bP samples with clean surface, which has restricted surface investigations of thin bP samples.

To tackle this problem, we used a glove bag for bP exfoliation. A glove bag is simply a bag of plastic whose openings can be sealed. It has gloves attached to the bag, which

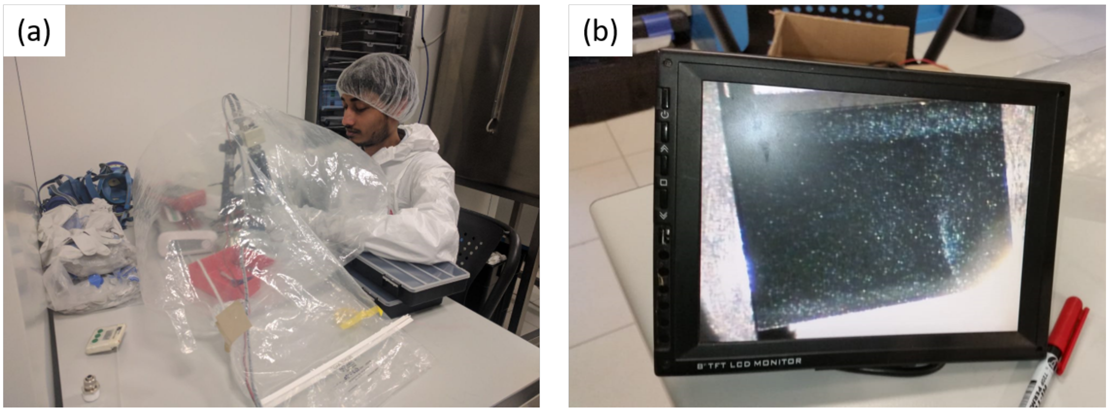

FIGURE 3.7 bP exfoliation inside glove bag. (a) Sample preparation inside a glove bag filled with N_2 which provides inert atmosphere for sample preparation. After bP exfoliation and transfer on a graphene substrate, sample mounting on the STM sample holder is also performed inside the glove bag. (b) Image of a sample after bP exfoliation and mounting on a STM sample holder, as seen on a monitor from a low magnification camera. Some larger bP flakes, which are visible by naked eye, appear like stars distributed on the sample.

allows the handling of the sample inside the bag. Meanwhile N_2 gas is flushed inside the bag, which provides an inert atmosphere for the sample. One such glove bag is shown in Fig. 3.7(a). We inserted a clean graphene substrate, a bP crystal, scotch tape, tools like tweezers, and a STM sample holder inside the glove bag before sealing it. We exfoliated bP using scotch tape inside the glove bag. The exfoliated bP flakes were then transferred from the scotch tape to the graphene substrate. Finally, the sample was mounted on the STM sample holder inside the glove bag. Fig. 3.7(b) shows a sample after bP exfoliation and mounting on the STM sample holder. Shiny star-like features, seen using a low magnification video camera placed inside the glove bag after completing the exfoliation procedure, are larger bP flakes, which indicates that flakes are evenly distributed and exfoliation is successful.

We also had inserted a small plastic bag and a sealing machine inside the glove bag. The prepared and mounted sample was sealed inside this small plastic bag with inert N_2 gas, suitable for taking it from the sample preparation site to the STM chamber without exposing the sample to ambient air. At the STM, the loadlock chamber was also flushed with N_2 and kept ready to be pumped. Once the prepared sample was removed from the sealed plastic bag, it was right away transferred to the loadlock chamber, and the pumping was started immediately, limiting the sample exposure to air to less than a minute.

Figure 3.8 shows characterization of the exfoliated bP flakes on graphene after finishing STM measurements. We did optical microscopy, as shown in Fig. 3.8(a), which shows the distribution of larger flakes of bP. Some of them are visible by naked eye and appear like stars on the substrate, as shown in Fig. 3.7(b). Optical microscopy also shows a

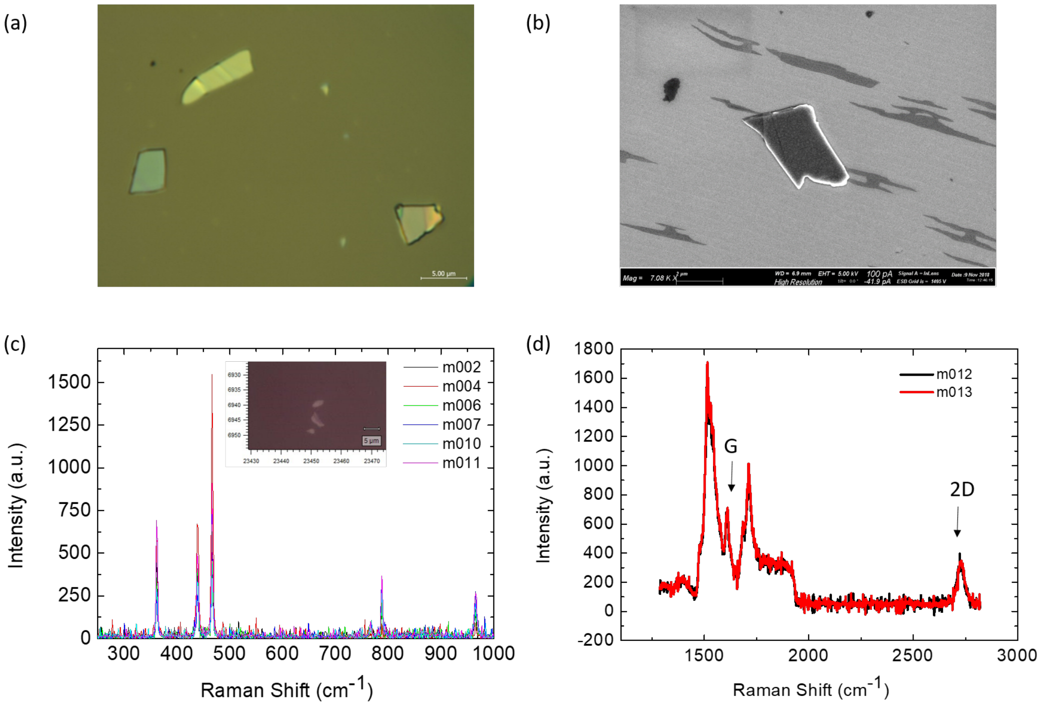

Figure 3.8 The bP samples were further characterized after the STM measurements were completed. (a) An optical image of the sample shows bP flakes of different sizes. The larger flakes might be the ones that appear like star with naked eye, as shown in Fig. 3.7(b). the smaller flakes are the ones typically measured by STM. Scale bar: 5.0 μm. (b) SEM image of the sample. Both large and small flakes can be seen. It also shows a contrast on the substrate. This is because of the presence of some bilayer graphene. Scale bar: 2 μm. (c) Raman characterization showing the A_g^1, B_{2g} and A_g^2 Raman modes of bP at 361 cm^{-1}, 438 cm^{-1}, and 468 cm^{-1}. This confirms the presence of bP on the sample even after the STM measurements has completed, which demonstrates that the bP flakes are well preserved during all STM measurements. Some peaks are also present at 766 cm^{-1}, 789 cm^{-1} and 964 cm^{-1}, which are due to 6H SiC from the substrate. (d) Raman characterization in different energy range showing the G and 2D peaks of graphene, which is present below and next to bP flakes. These measurements were performed by Dr. F. Telesio at CNR-NEST, Pisa.

large number of tiny flakes distributed around the larger ones, which are not visible at low magnification, but typically it is these flakes which are measured by STM. So, when we see evenly distributed larger flakes with the low magnification video camera (of Fig. 3.7(b)), we can also be sure that there are a lot of tiny flakes around them, suitable for STM investigation. We also did scanning electron microscopy (SEM) imaging, which further helps in understanding the flake density on the graphene substrate. In Fig. 3.8(b), tiny flakes can be seen, with steps in the SiC substrates in the background. The contrast in the graphene substrate is due to the presence of some bilayer graphene inclusions. Understanding the distribution of these flakes by optical microscopy and SEM has helped to optimize various parameters of the exfoliation process like the amount of bP crystal to be taken for exfoliation, the number of times the scotch tape is stuck and separated to have thin flakes ($\sim$70 times), and the number of times the substrate is tapped on the scotch tape (7 times) to transfer the exfoliated bP flakes onto the substrate. The fact that we are able to observe these tiny flakes after completing the STM investigation indicates that the bP flakes on the sample are well preserved in the UHV environment.

Raman spectroscopy is used to determine the vibrational modes of molecular bonds, which helps in identifying the chemical identity of bonds present in the sample. Figs. 3.8(c) and (d) show Raman spectroscopic measurements of the sample at $\lambda = 532$ nm, taken on different locations of the sample. The inset in (c) shows an optical image of one of the locations, named 'm006'. bP flakes are clearly visible. The three peaks in the Raman spectra in Fig. 3.8(c) at 361 cm^{-1}, 438 cm^{-1}, and 468 cm^{-1} correspond to the A_g^1, B_{2g}, and A_g^2 Raman modes of bP [104], respectively. The extra peaks at 766 cm^{-1}, 789 cm^{-1} and 964 cm^{-1} are due to 6H SiC [129], from the substrate below or next to exfoliated bP flakes. The G and 2D peaks marked in Fig. 3.8(d) correspond to the graphene substrate [130]. The fact that we see such clear Raman fingerprints of bP even after the STM studies is further evidence that the bP flakes are well preserved during all our experiments.

3.3 Copper evaporation

Copper evaporation was performed inside the preparation chamber of the Omicron LT-STM system with a base pressure of $\sim 10^{-10}$ mbar, using a Focus GmBH EFM-3s UHV electron beam evaporator. A schematics of the evaporator is shown in Fig. 3.9. It consists of a filament which acts as an electron source when current is flowing through it. The material to be evaporated, copper in our case, is kept in a crucible with high voltage applied to it. This high voltage accelerates the electrons from the filament towards the crucible, which heats the crucible and melts the material in it, leading to the deposition of the evaporant on the sample placed in front of the evaporator. The amount of copper being deposited is measured by an in-built flux monitor. A fraction of the copper atoms being deposited is naturally ionized in the process. An ion collector placed at the beam exit column measures the ion current which is proportional to the total flux of copper atoms deposited.

The table in Fig. 3.10(a) gives the deposition fluxes and times for three different samples used to investigate the morphological and electronic properties of copper on bP. Always the same parameters were used during all copper depositions: 800 V applied to the crucible and 1.95 A applied as filament current. Figure 3.10(b) shows copper fluxes for successive depositions and demonstrates the stability of flux output from the evaporator during our experiments. The average flux of 18 depositions is (9.62 ± 0.61) nA.

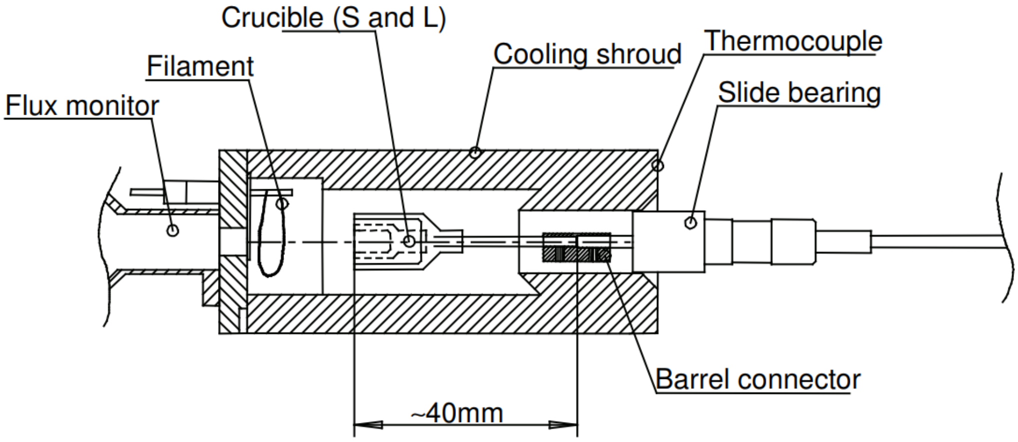

FIGURE 3.9 A schematics of EFM 3s UHV evaporator used to deposit copper on bP. [131]

(a)

Sl. No.	sample	Individual dep. Time (s)	total dep. Time (s)	Individual flux (nA)
1	bP-15_Cu-I	15	15	9,51
2	bP-15_Cu-II	15	30	9,04
3	bP-15_Cu-III	600	630	10,8
4	bP-15_Cu-IV	120	750	11
5	bP-15_Cu-V	180	930	9,85
6	bP-16_Cu-I	120	120	9,81
7	bP-16_Cu-II	180	300	9,9
8	bP-16_Cu-III	180	480	9,9
9	bP-16_Cu-IV	220	700	9,87
10	bP-17_Cu-I	30	30	9,4
11	bP-17_Cu-II	30	60	9,11
12	bP-17_Cu-III	30	90	9,04
13	bP-17_Cu-IV	30	120	9,15
14	bP-17_Cu-V	680	800	9,12
15	bP-17_Cu-VI	100	900	9,85
16	bP-17_Cu-VII	100	1000	8,72
17	bP-17_Cu-VIII	100	1100	8,9
18	bP-17_Cu-IX	100	1200	10,2

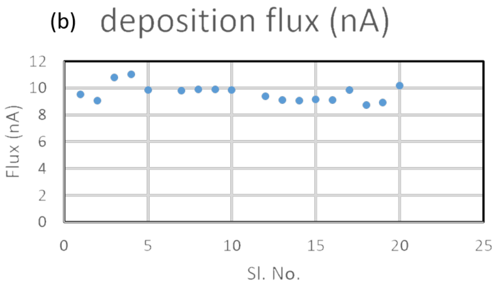

FIGURE 3.10 Three different samples were deposited with copper for total of 18 times to obtain bP surfaces with different amounts of copper. (a) Table showing the deposition times for individual copper depositions. Same parameters of filament current and crucible voltage are used to have same flux during all depositions. Flux values measured during individual depositions are shown in (b). The average flux of 18 depositions is (9.62 ± 0.61) nA.

A sample with copper deposited on it was characterized with energy dispersive X-Ray spectroscopy (EDS), to confirm the identity of the material deposited. Figure 3.11 shows such a measurement performed on a bP exfoliated sample after copper deposition. Figure 3.11(a) shows an SEM image of the sample marked with two points where EDS spectra were recorded: 'Objects 97' on the substrate and 'Objects 98' on a flake. Figure 3.11(b) shows EDS spectra from different regions of the sample, showing peaks at 1.739 keV and 0.277 keV, corresponding to silicon and carbon, respectively, present in the substrate of the sample. A peak at 2.013 keV corresponding to phosphorus, is present only in the spectrum corresponding to 'Objects 98', which identifies the bP flake on the substrate. A zoom-in around the energy of 0.93 keV, which corresponds to copper, is shown in Fig. 3.11(c) for enhanced visibility. Peaks in all spectra indicate the presence of copper all over the surface uniformly. The amplitude of the peaks is low due to the presence of very few layers of copper on the surface. Due to a slight oxidation after taking out the sample from the STM chamber, a small peak of oxygen can also be seen in both spectra at the energy of 0.525 keV.

3.4 DFT calculations

The PBE generalized gradient approximation for the exchange-correlation functional was used [132], and van der Waals interactions were included within the semi-empirical method developed by S. Grimme (DFT-D2) [133]. Ultrasoft pseudopotentials were employed as available in the PS Library by A. Dal Corso [134]. The kinetic energy cutoff for the wave functions (charge density) was set to 50 (600) Ry. The few-layer bP with copper impurities was modeled by employing a 4 × 3 supercell for single-layer (1L) and bilayer (2L) bP, with the in-plane lattice parameters set according to the optimized parameters of the 1L and 2L primitive cell. A vacuum region of 30 a.u. in the non-periodic directions was introduced to prevent interaction between periodic images; the Brillouin zone was sampled by using a $4 \times 4 \times 1$ k-points grid, according to Monkhorst-Pack algorithm. The atomic positions within the cell were fully relaxed until forces were less than 5×10^{-4} a.u. The binding energies of the copper impurities were computed as total energy differences according to:

$$E_b\left(Cu_X\right) = E_{tot}\left(Cu_X : bP\right) - N_{cell}\, E_{tot}\left(nL - bP\right) - N_{Cu}\, E_{tot}\left(Cu\right), \tag{3.6}$$

where Etot(CuX:bP) is the total energy of the copper-doped bP slab, Etot(nL-bP) is the total energy of n-layer bP (calculated in the primitive cell and multiplied by the number of primitive cells Ncell), and Etot(Cu) is the total energy of atomic copper.

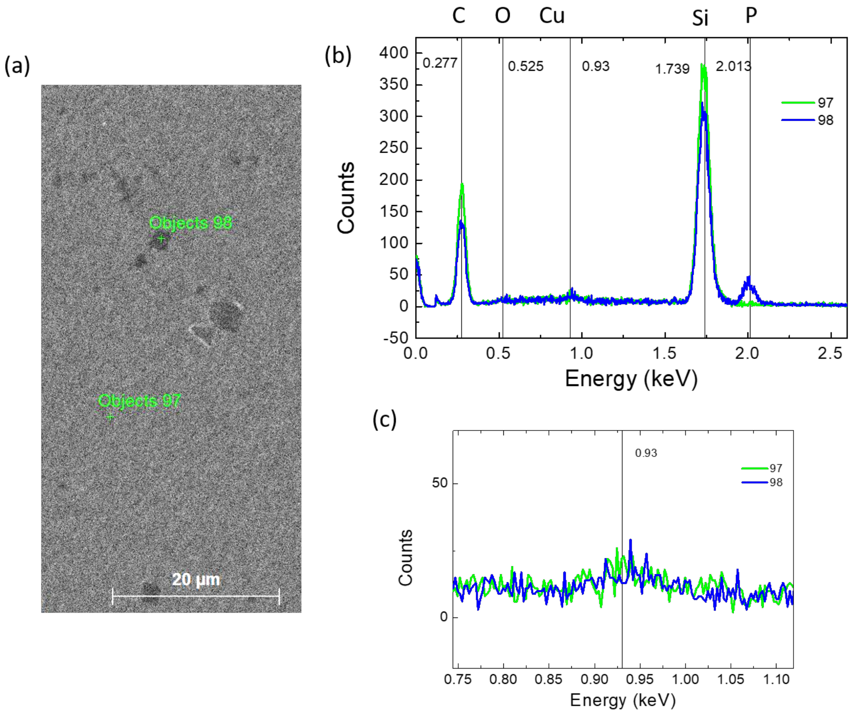

Figure 3.11 EDS measurements were performed after copper deposition. (a) SEM image of sample is shown were flakes can be identified on the substrate. EDS spectra on substrate (Object 97) and on flake (Object 98) are measured. (b) EDS spectra are plotted, showing substrate spectra (Object 97) in green and flake spectra (Object 98) in blue. EDS peaks are marked by the corresponding elements. Phosphorus peak is only seen in blue, which identifies bP flake on the substrate. Carbon and silicon peak are present in all spectra since they are in substrate, present everywhere. Copper peak is also present in all spectra. A zoom-in of curves near the energy corresponding to copper is shown in (c) for better visualization. A clear peak can be seen in all spectra at 0.93 keV. However, the amplitude of peak is small due to the presence of very few layers of copper on the surface. A small peak of oxygen can also be seen in all spectra, due to a slight oxidation after taking out the sample from UHV. These measurements were performed by Dr. F Telesio and Dr. V Zannier at CNR-NEST, Pisa.

Chapter 4

bP Surface Study

For studying the surface of any material, the prime necessity is to have a clean surface. This is ensured by the sample preparation methods described in Chapter 3. Having prepared a clean surface is however not enough, because the surface needs to be maintained clean during the experiment. This is taken care of by the UHV chamber inside which the samples are stored and the surface is studied. The surface probing technique used in our study is scanning tunneling microscopy, which requires a conducting substrate. And this is ensured by using graphene on SiC as the substrate.

Here, the first challenge was to identify the bP flakes on the graphene substrate. A priori, the position of the bP flakes is not known. The exfoliated bP flakes are randomly distributed over the substrate. We started our research by approaching the tip in random positions close to the center of the sample to search for bP flakes.

4.1 STM characterization of the pristine bP surface

The primary criterion to identify flakes is the height and size of the entity relative to the substrate. The bP flakes appear as plateau-like structures – several nm high, and flat. Some examples can be seen in Fig. 4.1(a)-(c), with the height profile of the flakes in the inset. The dimensions of the individual flakes are: (a) average height (22.3 ± 0.4) nm, flake size 1.0 μm^2, (b) average height (69.8 ± 0.1) nm for the higher part, (40.7 ± 0.2) nm for the lower part, flake size 2.5 μm^2, (c) average height (15.2 ± 0.2) nm, flake size 0.3 μm^2.

We performed a statistical measurement of flake sizes to have an estimate of the flake size distribution. The height of 42 flakes and the area of 36 flakes were measured, resulting in an average height of (37.5 ± 22.4) nm and an average area of (2.7 ± 3.2) μm^2. The

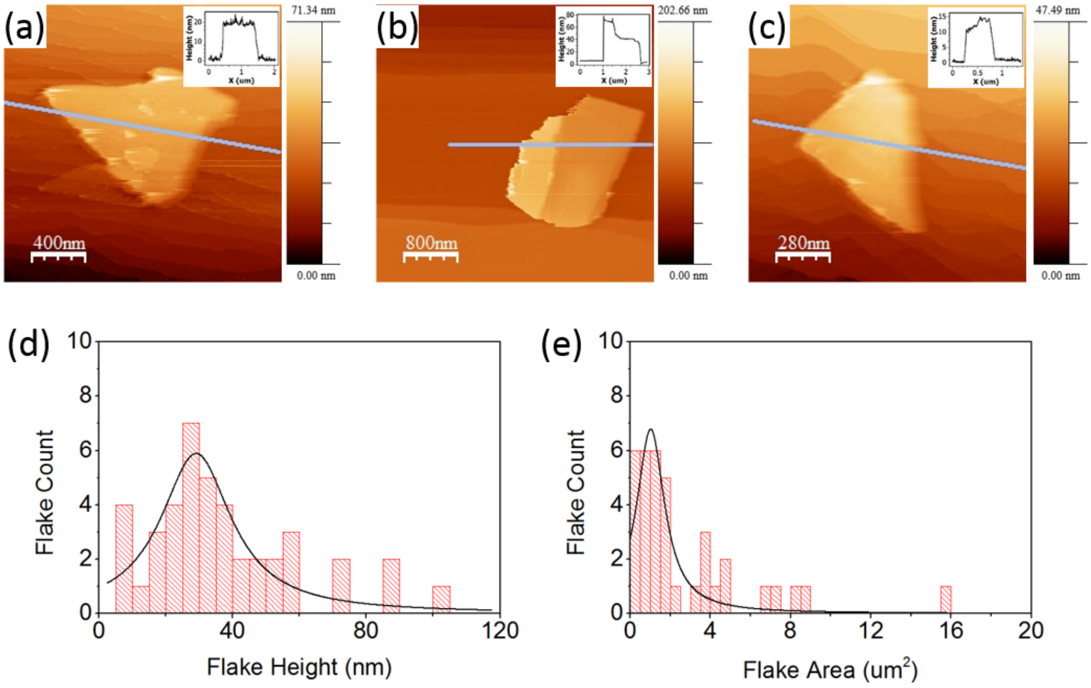

FIGURE 4.1 STM images of some flakes, indicating typical flake sizes of our samples. Scanning parameters and maximum annealing conditions: (a) (1.5 V, 100 pA), annealed at 400 °C for 5 min; (b) (1.0 V, 200 pA), annealed at 300 °C for 120 min; (c) (1.8 V, 100 pA), annealed at 350 °C for 120 min. Histogram plot of bP flakes' (d) height and (e) area - both fitted with a Lorentzian distribution.

area of some flakes is not measured because full images of the entire flakes were not obtained. Moreover, only flakes measured at T $\leq$ 400 °C are taken into account, to avoid significant thinning effects related to sublimation (as will be discussed later).

The average values of the height and the area of the flakes are slightly overestimated, because they are affected by few larger flakes measured. This can be appreciated in the histogram plots of Fig. 4.1(d) which shows flake height and Fig. 4.1(e) which shows flake area. The Lorentzian fits of the histograms give the values of the flake size distributions: a height of (29.1 ± 1.6) nm with FWHM (25.8 ± 4.9) nm, and an area of (1.0 ± 0.1) μm^2 with FWHM of (1.7 ± 0.3) μm^2. We take these as the typical sizes of our flakes, $\sim$30 nm high and $\sim$1 μm^2 in area.

After identifying a bP flake by its dimensions, we zoomed in on its surface to confirm its identity by measuring atomic-resolution images. An example is shown in Fig. 4.2. In Fig. 4.2(a), graphene can be seen on the left and a $\sim$25 nm high flake can be seen on the right. Fig. 4.2(b) shows atomic resolution on bP. The zigzag pattern corresponding to the phosphorus atoms in the upper plane of the bP surface is well visible. The measured unit cell parameters are $a = (3.45 \pm 0.43)$ Å and $c = (4.40 \pm 0.12)$ Å, close to literature values [66]. Figure 4.2(d) shows a bP surface with step and terraces. A line profile across several steps is shown in the inset, indicating the height of steps to be 0.5 nm or

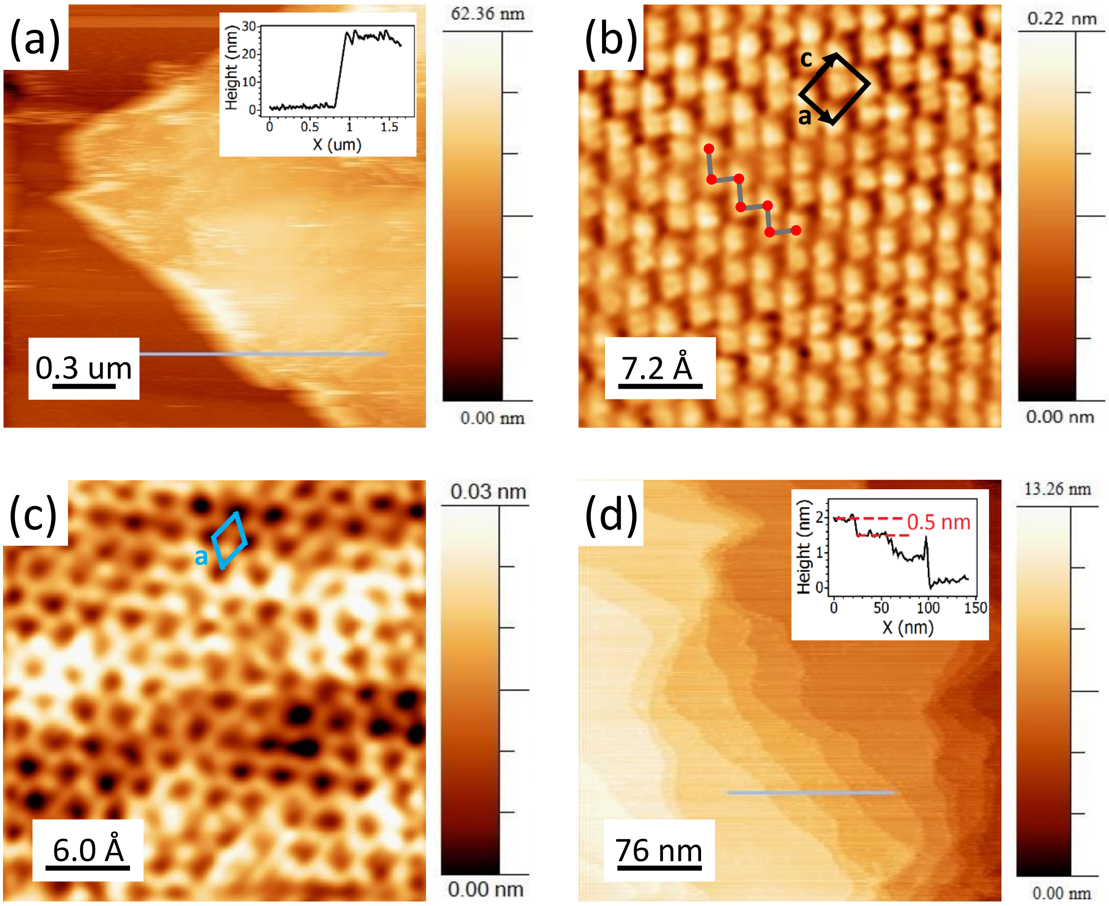

FIGURE 4.2 STM images identifying bP flakes and graphene substrate. (a) STM image showing on the right a bP flake ~ 25 nm high above the graphene substrate on the left. The inset shows the height profile across the line shown in the STM image. Scan size: 2 μm × 2 μm, imaging parameters: (0.7 V, 300 pA). Annealing conditions: 200 °C, 2 h. (b) Atomic resolution image obtained on bP at room temperature showing the zigzag pattern with unit cell parameters $a = (3.45 \pm 0.43)$ Å and $c = (4.40 \pm 0.12)$ Å. Scan size: 3.6 nm × 3.6 nm, imaging parameters: (0.7 V, 25 pA). Anealing conditions: 400 °C, 10 min. (c) Atomic resolution image on graphene. Unit cell indicated. Scan size: 3 nm × 3 nm, imaging parameters: (0.1 V, 157 pA). Annealing conditions: 450 °C, 2 h. (d) Steps measured on a bP flake. The height profile in the inset, taken along the line in the STM image, shows a step height of 0.5 nm, consistent with monolayer bP steps. Scan size: 380 nm × 380 nm, imaging parameters: (2 V, 100 pA). Annealing conditions: 400 °C, 10 min.

multiples of this value, consistent with the reported interlayer distance value for bP [66]. Figure 4.2(c) shows atomic resolution on graphene. The typical hexagonal pattern can be seen. The measured unit cell parameter, $a = (2.46 \pm 0.22)$ Å, is also consistent with the value reported in literature [135, 136]. This proves that we are reliably able to identify the bP flakes and the graphene substrate. This also indicates that we have achieved high quality bP surfaces, coping with the commonly experienced problem of bP surface degradation, and that these samples are ideal for high quality surface investigations.

4.2 Annealing experiments

Temperature is a very important parameter for material processing. Many such processes require the materials to go through high temperatures. Therefore, it is important to study the behavior of the surface of bP with increasing temperature. We carried out annealing experiments to investigate the morphological changes of the surface of bP.

The prepared sample was annealed in UHV in steps of 50 °C, and the surface was observed after each annealing step. Figure 4.3 shows a panel of 100 nm × 100 nm images scanned after annealing at temperatures starting from 200 °C to 500 °C. No atomic resolution was achieved for samples annealed below 300 °C, perhaps because the temperature was not high enough to suitably clean the surface from oxides or adsorbates. Figure 4.3(a) shows the STM image of a bP surface scanned after annealing at 200 °C for two hours, which looks quite noisy. Figure 4.3(b) shows the STM image of a bP surface scanned after annealing at 250 °C for 2 hours, which is slightly less noisy such that some features on the surface can be recognized. An inset shows a zoom-in of these features, which are defects on the bP surface. 300 °C and 350 °C annealing gives a clean and oxide-free surface where atomic resolution was measured. Figures 4.3(c) and (d) show bP surfaces scanned after annealing at 300 °C and 350 °C for two hours, respectively. The surfaces look smoother, and some defects can be clearly seen. The inset to Fig. 4.3(c) shows a zoom-in on the defects, better resolved than the one seen after 250 °C annealing in Fig. 4.3(b). Similar defects have been reported in other works, related to vacancies [64, 110], oxygen trapped in bP lattice [112], or to bP crystal growth related Sn impurities [111]. We measured the size of these defects to be 5-8 nm, in agreement with the reported values [64, 110–112].

Phosphorus starts desorbing from the surface upon annealing the sample to 375 °C - 400 °C. Figure 4.3(e) shows an example of such a bP surface with craters formed due to desorption, scanned after annealing at 400 °C for ten minutes. These craters appear elongated, and there seems to be some preferential alignment of these craters. A detailed analysis of these craters is performed and discussed in the next section. On further annealing at higher temperatures, large scale desorption of phosphorus starts due to the onset of sublimation. Figure 4.3(f) and (g) show the bP surface scanned after annealing for two hours at 450 °C and 500 °C, respectively. The bP surfaces can be seen to be quite rough. The RMS roughness is shown in the plot in Fig. 4.3(h) and has increased from 0.3 Å to 6 Å. Upon annealing to even higher temperatures, 550 °C - 600 °C, we observed that flake density, which was $\sim$ 1 flake in 100 μm^2, decreased by more than one order of magnitude.

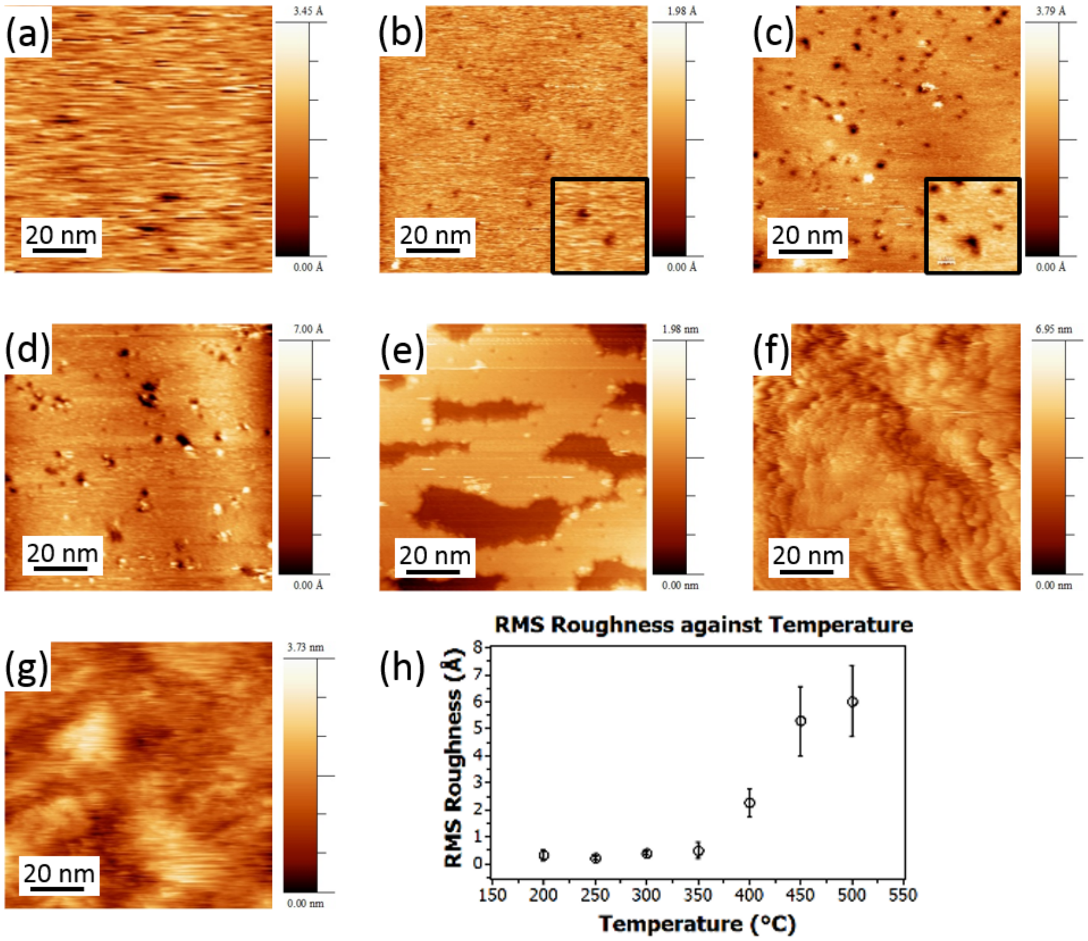

FIGURE 4.3 Surface morphology with temperature. 100 nm × 100 nm images of the bP surface taken after annealing at different temperatures, starting from 200 °C and increasing in steps of 50 °C, are shown, indicating the surface modification with temperature. Annealing temperature and scanning setpoints for individual images : (a) 200 °C, (2.5 V, 100 pA); (b) 250 °C, (1.3 V, 157 pA); (c) 300 °C, (1.2 V, 100 pA); (d) 350 °C, (1.8 V, 100 pA); (e) 400 °C, (2.0 V, 100 pA); (f) 450 °C, (1.2 V, 100 pA); (g) 500 °C, (1.2 V, 100 pA). All samples were annealed for 2 h, except (e) which was annealed for 10 min. The image after 200 °C annealing seems noisy, probably affected by oxides or adsorbates on the surface. After 250 °C annealing, we start seeing some features which could be defects (inset of (b)). These defects can be seen better resolved after 300 °C annealing (inset of (c)). After 400 °C annealing, craters start appearing on the surface, as seen in (e). Going to higher temperatures, a large amount of phosphorus desorbs, making the surface rough, as seen in (f) and (g) after annealing to 450 °C and 500 °C, respectively. The plot in (h) shows the trend of surface RMS roughness with temperature. The surface roughness at 400 °C is caused by the monolayer-deep large craters, although the individual terraces are flat enough to achieve atomic resolution.

4.3 Phosphorus desorption and crater formation

We observed elengated crates on the surface due to phosphorus desorption after annealing the samples at 375 °C - 400 °C. To eliminate the possibility that the craters might be forming as a result of scanning with the tip, we scanned one spot multiple times while changing tip scanning direction. Figure 4.4 shows a panel of scans corresponding to this measurement. The blue arrow in each image represents the direction of movement of the tip while scanning. First multiple images were taken with the tip scanning horizontally. Then the tip scanning direction was changed orthogonally, and multiple images were recorded. Finally, the tip scanning direction was again changed to the initial horizontal direction, to compare with the initial images. The craters remain unaffected by such a change of tip scanning direction which confirms that the observed craters are not caused by the tip.

Next we performed a statistical analysis of the orientation of these craters on the surface of three different flakes, shown in Fig. 4.5. We fitted an ellipse across each crater and noted the angle of the long axis of the ellipse with respect to the horizontal. We name this angle *crater angle,* θ. The average values for the crater angle, $<\theta>$ with respect to the horizontal for each image is: (1.6 ± 37.0) ° for (a), (3.5 ± 19.0) ° for (b), and (-3.2 ± 19.4) ° for (c). The value of the standard deviation is particularly high in (a) because of the presence of comparatively fewer craters on the surface of bP which gives mediocre statistics.

For a better visualization of relative orientation of the craters, we subtracted the average value of crater angle obtained for each image from the crater angle of individual craters of the image (performing θ - $<\theta>$). This operation just rotates each crater by the average angle of the image, such that the average crater angle becomes zero for each image. Since it rotates every crater of the image by the same angle, this operation does not affect the relative orientation of the craters. However, now with the help of this operation, we have craters of all images with the same average angle of 0 °. This helps to compare the orientation of craters measured on different flakes of bP.

The set of the rotated crater angles were plotted in histograms to evaluate the relative orientation of craters. Figures 4.5(d)-(f) show the data plotted with the same binning for three different flakes' images shown in Fig. 4.5(a)-(c), respectively, to compare the statistics of these three separate flakes. Each of these histograms was fitted with a Lorenzian curve which gives central angle as the position of the peak and spread of the angles as FWHM (full width at half maximum). Then the same dataset were plotted with a dynamical binning, as shown in Fig. 4.5(g)-(i), which represents the data better, reflected in reduced values of FWHM of individual data sets. The position of the peak

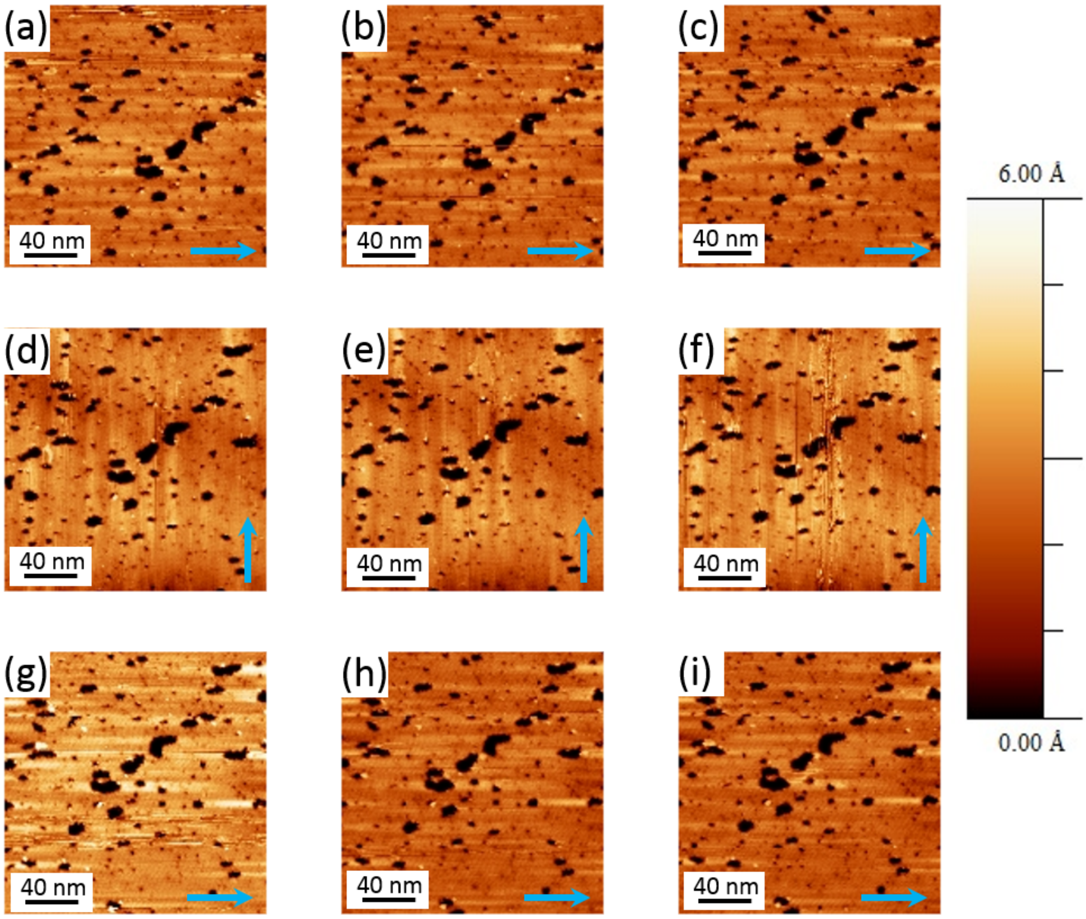

FIGURE 4.4 Craters were scanned with the tip moving along different directions with respect to the crater orientation, to check if the motion of the tip is causing crater formation or any surface modification that could produce scanning-related elongation of the craters on the surface. The same area is scanned with the tip moving almost parallel to the crater orientation: (a)-(c), then almost perpendicular: (d)-(f) and then again almost parallel: (g)-(i). The blue arrows indicate the direction of motion of the STM tip while scanning. Several images were measured but only the 1^{st}, 3^{rd}, and 5^{th} are shown in each of the three categories, which is sufficient to demonstrate the consistency of the experiment. All images are scanned with the same scanning parameters (1.2 V, 25 pA) after annealing the sample at 375 °C for 10 min. The flake is 101.7 nm high and 4.6 μm^2 in area.

of the Lorenzian curves for histograms corresponding to craters in all three images is around 0 °. The reduced FWHM demonstrates the preferential orientation of the craters. Moreover, absence of even a single data point at 90 ° rules out the presence of any crater in the perpendicular direction.

As discussed in detail in Sectio2.3, the presence of these elongated craters with preferential orientation on the surface of bP was recently reported in two different studies investigated by electron microscopy [114, 115]. Because of comparatively higher resolution provided by a STM, we were able to resolve craters that are one order of magnitude smaller in size than the craters reported in literature. The larger craters reported in

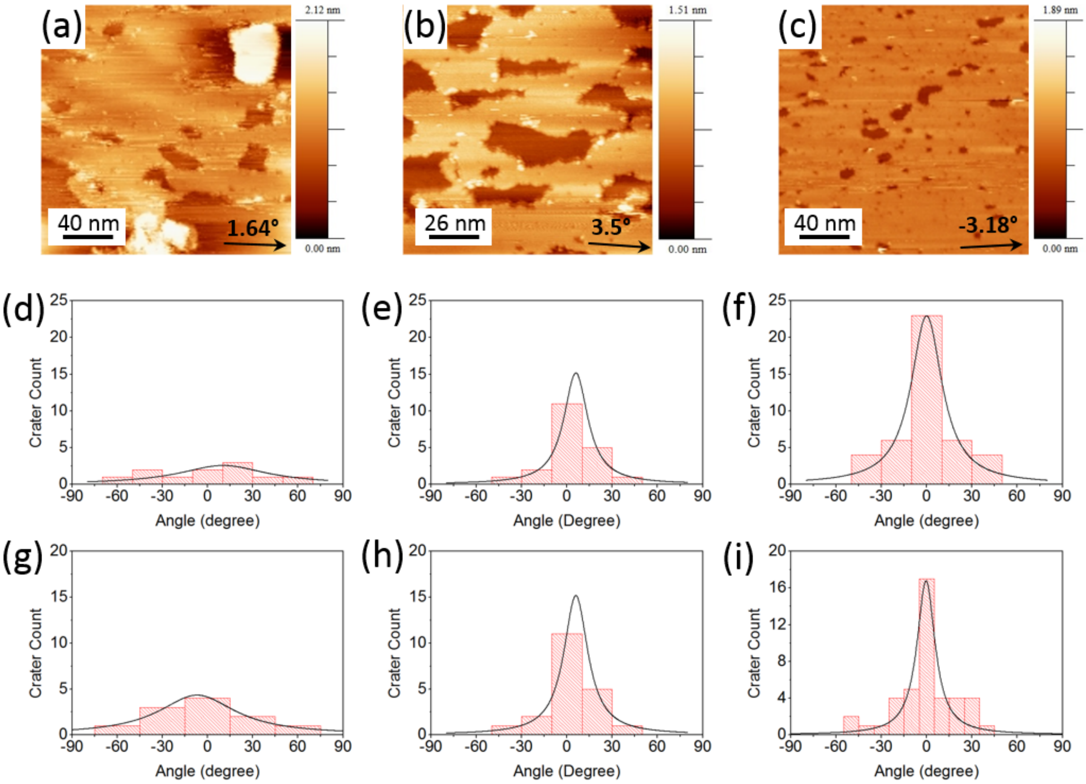

FIGURE 4.5 STM images of craters as observed on three different flakes. Scanning parameters, maximum annealing temperature, and flake sizes for each image: (a) (1.5 V, 100 pA), annealed at 400 °C for 5 min, flake 22.3 nm high and 0.96 μm^2 in area; (b) (2.0 V, 100 pA), annealed at 400 °C for 10 min, flake 58.8 nm high and 1.18 μm^2 in area; (c) (1.2 V, 25 pA), annealed at 375 °C for 10 min, flake 101.7 nm high and 4.6 μm^2 in area. The average angle of the long axis obtained for the craters on each image is indicated. The individual angles for each craters in the figures (a), (b) and (c) are represented in histogram plots: first with same binning of 20 ° with the peak and the FWHM of the Lorentzian fit in figures (d) peak at (10.0 ± 8.3) ° and FWHM of (71.0 ± 26.0) °, (e) peak at (6.0 ± 0.7) ° and FWHM of (19.5 ± 2.6) ° and (f) peak at (0.0 ± 1.95) ° and FWHM of (25.2 ± 2.5) °, respectively, and then with dynamical binning of 30 °, 20 °, and 10 ° with the peak and FWHM of the Lorentzian fit in figures (g) peak at (-7.0 ± 3.3) ° and FWHM of (62.8 ± 9.5) °, (h) peak at (6.0 ± 0.7) ° and FWHM of (19.5 ± 2.6) °, and (i) peak at (-0.4 ± 1.1) ° and FWHM of (14.7 ± 1.7) °, respectively.

literature were most likely formed by the coalescence of the smaller craters that we observed. So, we were able to observe the initial stages of crater formation at 375 °C-400 °C, and show that even these craters are elongated and have a preferential direction of orientation.

However, the reported studies contradict each other in their results obtained regarding the direction of the orientation of these craters and the mechanism behind the formation of these craters. First study published by Liu *et al.* [114] in 2015 reported that atomic P desorption leads to the formation of elongated craters aligned along the crystallographic armchair direction of bP. A second study published by Fortin-Deschenes *et al.* [115] in

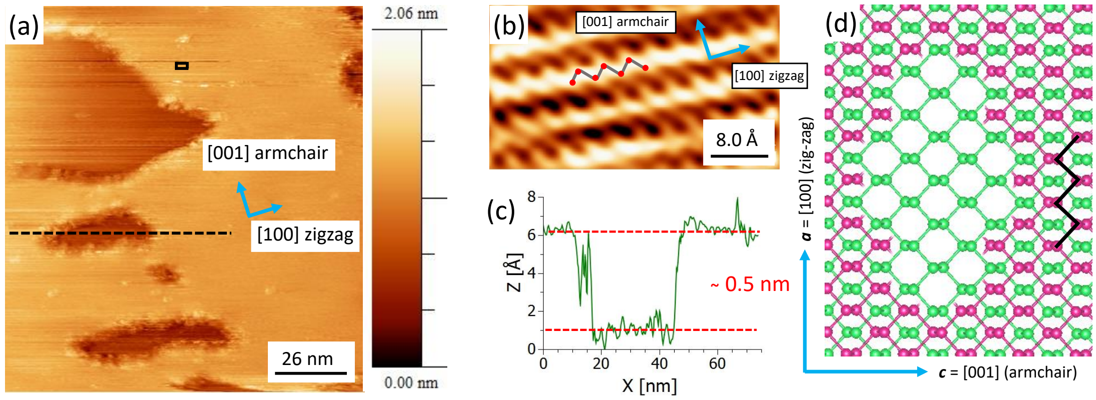

FIGURE 4.6 Crystallographic direction of crater alignment. (a) STM image of a 130 nm × 130 nm scan area, showing aligned craters on bP after annealing at 400 °C for 2 h; scanning parameters: (1.2 V, 100 pA). (b) Atomic resolution image obtained after zooming into the region marked in (a), providing information of the crystallographic directions of the bP flake; scanning parameters: (1.2 V, 100 pA). (c) Height profile across the crater along the dashed line in (a), showing ∼ 0.5 nm step height, compatible with monolayer desorption. (d) Schematics showing crater formation due to bP desorption - bottom layer (green) visible under desorbing top layer (red). Crystallographic direction is denoted by black zigzag drawn along [100] direction.

2016 reported that molecular P_2 desorption leads to the formation of elongated craters aligned along the crystallographic zigzag direction of bP. These two crystallographic directions are orthogonal to each other, while we observed in our experiment that there was not a single crater oriented orthogonally, which suggests that there is some inconsistency in the present literature regarding the crater orientation direction. We decided that an STM investigation of craters along with atomic resolution on bP surface could resolve the debate and help to understand the underlying mechanism behind the formation of these craters.

Figure 4.6 shows an investigation done to relate the direction of crater orientation to the bP crystallographic directions. Figure 4.6(a) shows an image of the surface of a bP flake. Elongated craters can be seen with their long axes aligned. Figure 4.6(c) shows the height profile across a crater along the black dashed line in Fig. 4.6(a). Crater depth of ∼0.5 nm indicates monolayer desorption. To determine the crystallographic direction of bP, we zoomed in for atomic resolution. Figure 4.6(b) shows an image acquired by zooming-in on the region indicated by the black rectangle in Fig. 4.6(a). Crystallographic armchair and zigzag direction can be clearly identified in the image, which is then marked in Fig. 4.6(a) to compare with craters' alignment. Thus, the long axis of the craters can be attributed to align along the zigzag direction. Together with the observation regarding the preferential direction of the alignment of these craters, we can conclude that asymmetric craters form during annealing which tend to align along zigzag direction, in agreement with the study reported by Fortin-Deschenes *et al.* [115].

4.3.1 Discussion

Two competing underlying mechanisms have been presented in literature leading to anisotropic crater formation: (i) atomic P desorption leading to crater formation along armchair direction [114], and (ii) molecular P_2 desorption leading to crater formation along zigzag direction [115].

A simplistic model has been proposed to explain the anisotropic crater formation by atomic P desorption using the propagation of cracks, starting from a single vacancy site [114], as shown in Figs. 2.7(e)-(j). The order of removal of unsaturated P atoms considered for the propagation of a crack is: (a) P atoms with only one bond, bonded with only one other P atom, desorbs first, then (b) P atoms with two bonds, bonded with two other P atoms, both lying in the same plane, and finally (c) P atoms with two bonds, bonded with two other P atoms, lying in different planes. This leads to the formation of an anisotropic crater starting from a single atomic vacancy, aligned along armchair direction.

However, if we take a look at the in-plane and the out-of plane bond lengths in bP, the in-plane bond (2.22 Å) is shorter than the out-of plane bond (2.24 Å). A shorter bond length implies a stronger bonding. This implies that on comparing the unsaturated atoms having two bonds, P atoms bonded with two atoms in the same plane (P atoms with two in-plane bonds), named earlier as (b), should be more strongly bound than unsaturated atoms bonded with two atoms in different planes (P atoms with one in-plane and one out-of plane bonds), named earlier as (c). This suggests that it should be easier to remove (c) compared to (b). A density functional theory (DFT) calculation reported in Ref. [115] which compares the activation energy required for removal of P atoms from bP surface in different configurations, supports this idea by showing that the activation energy required for removal of (b) [process # 3, 4.02 eV] is higher than the activation energy required for removal of (c) [process # 3, 3.43 eV], as shown in Fig. 2.8.

On analysing the activation energies for different atomic desorption processes, the proper order of removal that should be used is: (a) should desorb first, then (c) and finally (b). Therefore, the order of removal of unsaturated P atoms considered in the model represented in Fig. 2.7 appears unfounded. We did the same modeling employing the proper order of stability of unsaturated P atoms and obtained crater elongated in zigzag direction, as shown in Fig. 4.7.

The mechanism of molecular P_2 desorption leading to crater formation has been evaluated in detail by Fortin-Deschenes *et al.* [115]. They have calculated activation energies for removal of P and P_2 in different configurations from bP nanoribbons using DFT

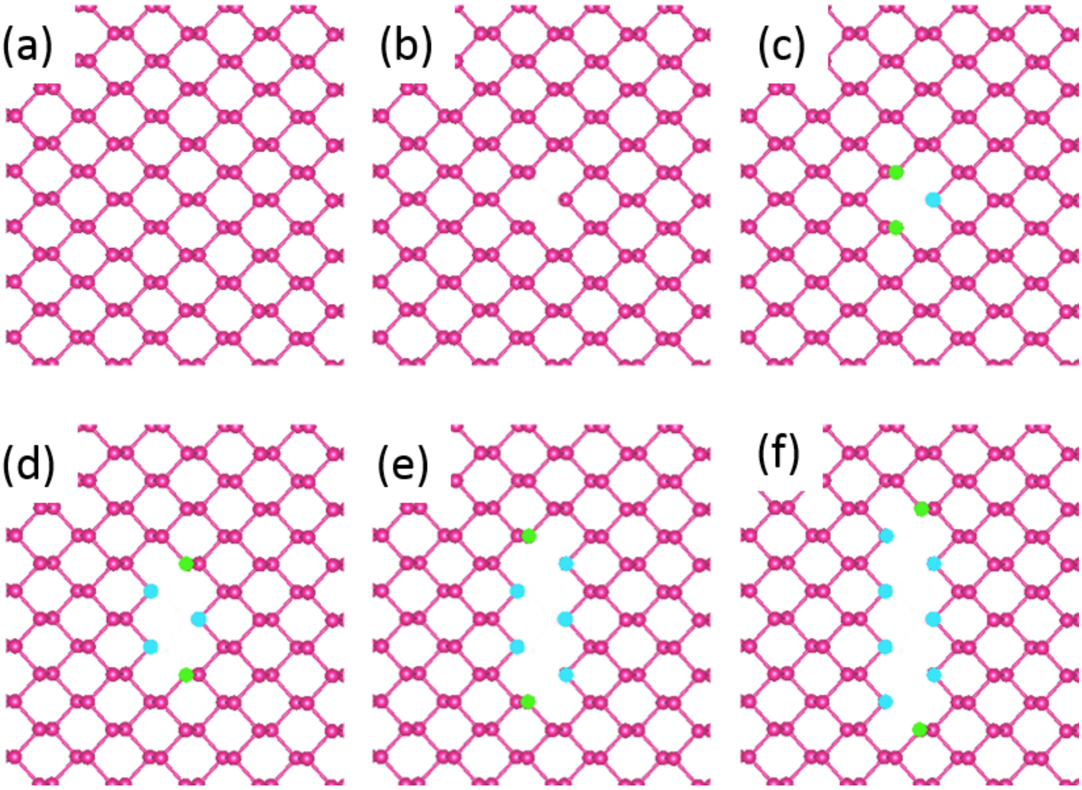

FIGURE 4.7 Sublimation model for crater elongation by monoatomic P desorption. (a) Monolayer bP lattice without defects, (b) monoatomic vacancy, (c) color coding the different types of unsaturated P atoms – those with two bonds in the same plane (sky blue) and those with the two bonds in different planes (light green), (d)-(f) removing the atoms according to the bonding strength and further color coding the unsaturated P atoms – thus leading to the evolution an elongated crater with the long axis aligned along the zigzag direction.

calculations and used these energies in a kinetic Monte Carlo simulation of crater formation by removal of 10^6 atoms. Their simulation gives anisotropic craters aligned along the zigzag direction, in agreement with their LEED mesurements and our STM measurements.

From the models presented in literature, it appeared that atomic P desorption should lead to crater alignment along armchair direction and molecular P_2 desorption to crater alignment along zigzag direction. So, the underlying desorption mechanism seemed to be identifiable using the simple criterion of crater orientation. However, from a careful analysis of the activation energies for different configurations of atomic P desorption, we found that even atomic P desorption should lead to crater alignment along the zigzag direction. Thus, the measurement of crater orientation alone is not enough to distinguish between atomic P and molecular P_2 desorption mechanisms.

Nevertheless, Fortin-Deschenes *et al.* [115] obtained an experimental activation energy of (1.64 ± 0.10) eV from an Arhenius plot for sublimation leading to crater formation, which is in good agreement with the activation energy predicted by DFT calculation for molecular P_2 desorption. Moreover, according to their DFT calculations, the formation energy of divacancies is significantly lower than the one for monovacancies, which was confirmed later independently by a different group [137].

In conclusion, our study provides information on suitable annealing conditions of bP which yield stable and clean surfaces of bP flakes, which is 300 °C - 350 °C. We observed the onset of sample modification by eye shaped crater formation due to phosphorus desorption at 375 °C - 400 °C, and further degradation of bP flakes at higher temperatures, which is 450 °C - 500 °C. We also examined the preferential direction of craters' long axis alignment and could assign it to the crystallographic zigzag direction, and thus solved an existing debate in literature. Since after careful analysis we found that both atomic P and molecular P_2 desorption mechanisms lead to crater elongation along the zigzag direction, the determination of crater alignment direction with respect to bP crystallographic direction alone is not sufficient to pinpoint the underlying desoption mechanism. However, the discussion of energetics for various desorption configurations gives further insight into this matter. This is the first surface morphological study of exfoliated few layer thin bP flakes using STM conducted in UHV environment which provides useful insight in surface behavior and its degradation with temperature, which is very important in limiting thermal processing of bP for any practical applications.

Chapter 5

Copper on bP

Black phosphorus is intrinsically p-doped [66]. The p-type doping has been related to atomic vacancies in a recent STM study carried out by Kiraly *et al.* [64]. However, a p-n diode is a fundamental building block of electronic devices, which requires the realization of n-type bP. Copper causes n-type doping of bP. A recent study has demonstrated this through transport measurements [65]. But the details of growth and morphology of copper on bP are completely unknown.

In this work we have therefore studied the morphological features of copper growth on bP surfaces in detail. First, copper islands on a pristine bP surface are observed with atomic resolution. Then increasing coverage of the bP surface with copper has been examined. We encountered interesting behavior of copper islands on bP, like pinning of copper islands by bP defects, decoration of copper islands at bP step edges, and alignment of copper islands along the bP crystallographic armchair direction. We investigated the n-type doping of bP with copper by studying the local charge transfer using scanning tunneling spectroscopy. We observe a modulation in band gap and Fermi level position at the nanoscale. All these aspects are discussed in detail in this chapter and complemented by DFT calculations, which give us useful insights for the interpretation of experimental observations, including modifications of the electronic structure of bP.

5.1 Copper growth dynamics on the bP surface

To study copper on bP, we deposited copper on bP/graphene samples inside the UHV preparation chamber of an Omicron LT-STM (explained in detail in Chapter 3). In Fig. 5.1(a), a typical flake after 1200 seconds of copper deposition is shown, with graphene in the background overlaid on SiC steps. At this magnification, copper islands cannot be resolved on the surface. The bP flake looks very similar to the flakes

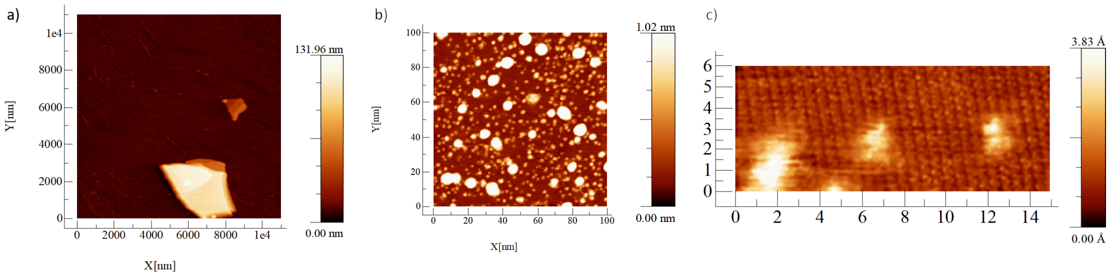

Figure 5.1 Atomic resolution - Cu on bP. (a) 11 μm × 11 μm STM image showing two bP flakes on graphene substrate after 1200 seconds of copper deposition. Scanning parameter: (-3.0 V, 0.33 nA). The smaller flake is ~30 nm high, and the bigger flake is ~100 nm high. Copper on sample can not be resolved at this magnification. (b) 100 nm × 100 nm STM image obtained on zooming in on the larger flake, showing copper islands on bP. Scanning parameter: (-1.0 V, 0.33 nA). (c) 15 nm × 6 nm STM image obtained on further zooming in, showing zigzag pattern corresponding to phosphorus atoms in the upper plane of bP surface measured at room temperature. Copper islands can be seen on atomically resolved bP surface. Scanning parameter: (-1.0 V, 0.33 nA).

shown in Chapter 4, which demonstrates the reproducibility of the bP sample preparation procedure. However, a big difference can be seen in Fig. 5.1(b), in which a zoom-in on the surface of the bP flake is shown. Here, the surface is not flat as seen for pristine bP in Chapter 4, but full of small white features. These are copper islands on the bP surface. On looking carefully, one can see that a few copper islands are much bigger (appear brighter) than other smaller copper islands which are however more numerous. We measured the dimensions of these two differently sized copper islands and found: an average diameter of (2.19 ± 0.34) nm and an average height of (0.47 ± 0.12) nm for smaller islands, and an average diameter of (7.20 ± 0.98) nm and an average height of (2.00 ± 0.25) nm for bigger islands. On further zoom-in, in Fig. 5.1(c) we see some small copper islands with bP atomic resolution in the background. This confirms that the high quality of the bP surface is maintained even after copper deposition on the sample.

In Fig. 5.1(c), we see an atomic resolution on bare bP surface but we do not see atomic resolution of bP crystal at the position of copper islands. This indicates that the copper stays at the surface and is not intercalated. Also, the height of copper islands indicates the presence of multilayers of copper which implies island growth on the surface instead of intercalation.

We start with a morphological investigation of copper growth on the bP surface with an increasing amount of copper. The sample was subjected to increasing copper deposition times at the same flux of 10 nA to obtain bP surfaces with increasing copper coverage. Each deposition episode needed the sample to be moved from the STM stage to the preparation chamber, which requires tip retraction and reapproach after the deposition,

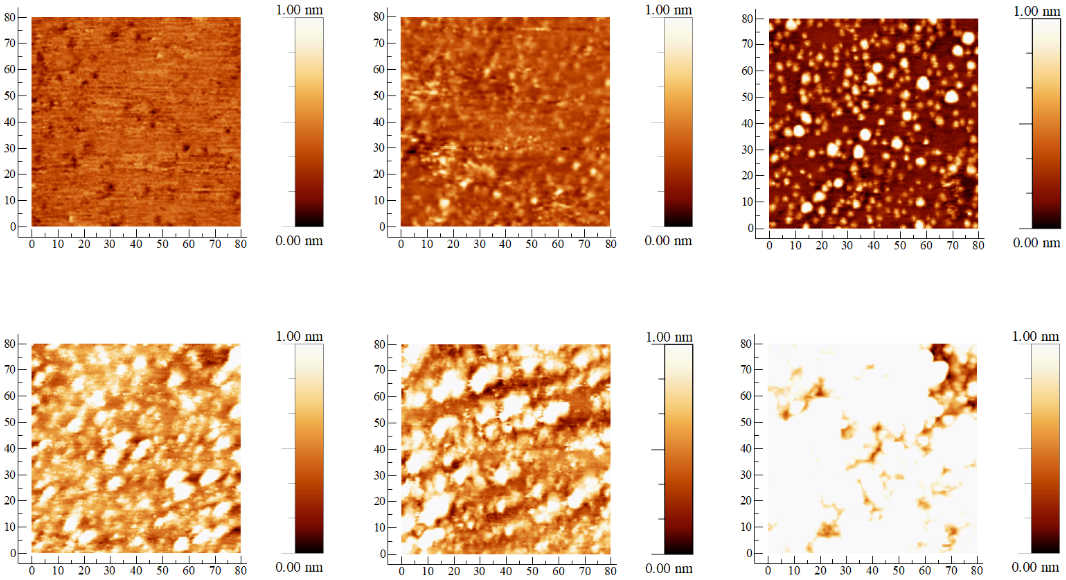

FIGURE 5.2 80 nm × 80 nm STM images of bP surface with increasing amount of copper deposited on sample. Total deposition time and scanning parameters for individual images: (a) 0 seconds, (1.0 V, 0.83 nA); (b) 120 seconds, (-1.0 V, 0.83 nA); (c) 300 seconds, (-1.0 V, 0.83 nA); (d) 480 seconds, (-1.0 V, 0.83 nA); (e) 750 seconds, (-1.0 V, 0.83 nA); (f) 930 seconds, (-1.0 V, 0.83 nA). Flux of ∼10 nA was used for all copper depositions. All images are shown with same color bar to compare increasing amount of copper in successive images.

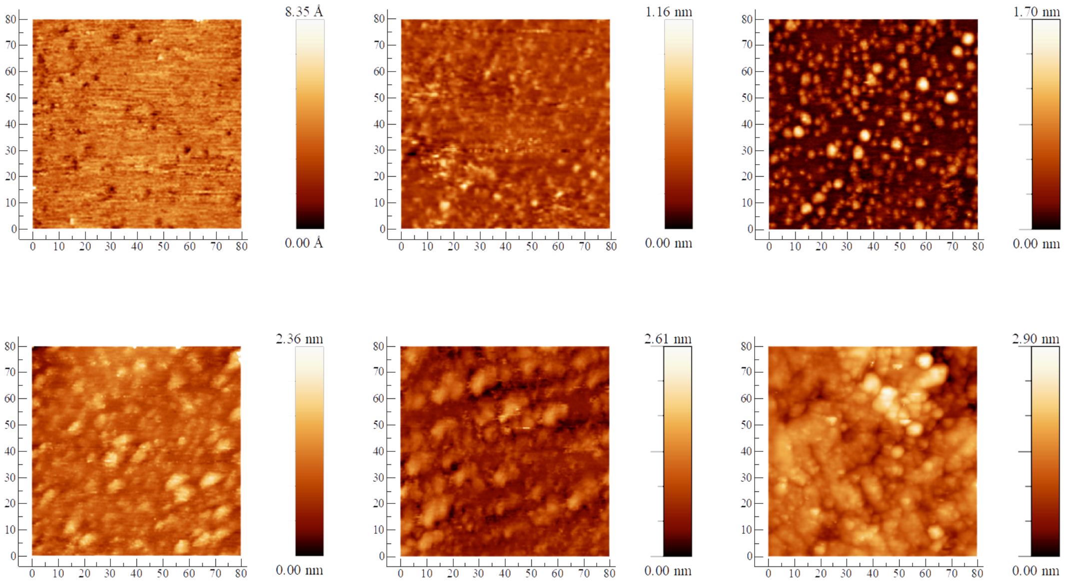

FIGURE 5.3 STM images of Fig. 5.2 shown with individual color bar, for better visualization of copper morphology on bP.

which implies scanning different flakes after every deposition. However, after each deposition, we measured several flakes, to obtain a statistical estimate of the bP surface appearance. Overall, 3 different samples with a total of 18 distinct copper coverages were measured to get a good overview of the copper coverage on the bP surface.

Figure 5.2 shows a series of 80 nm × 80 nm STM images of bP surfaces with increasing

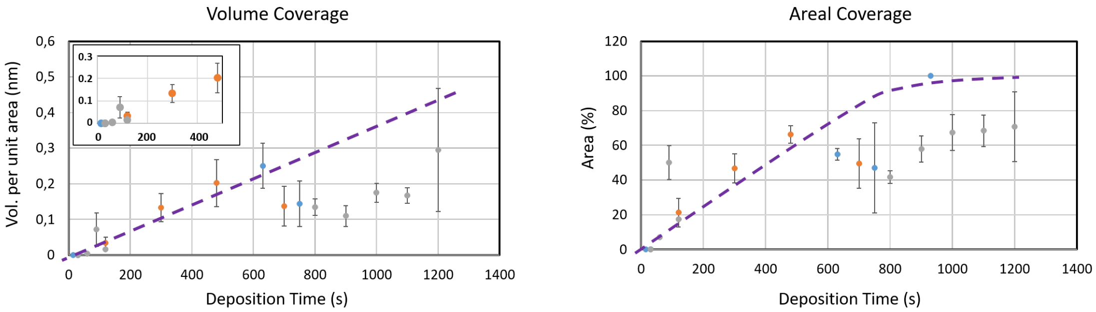

FIGURE 5.4 (a) Volume coverage, and (b) areal coverage of bP surface is plotted against increasing time for which copper is deposited at a constant flux of (9.62 ± 0.61) nA. The data is obtained by performing STM measurements of three different samples (indicated by blue, orange and grey data points in the plots) deposited with copper. In total, 18 depositions were performed. The dashed lines are a guide to the eye indicating the expected behavior. The inset in (a) is a zoom-in to show that no copper was seen on bP initially at lower deposition times.

copper coverage. The z-scale color bar is the same for all images, higher features appear brighter, and features more than 1 nm high appear white. Successive images appear brighter, which illustrates well the increasing amount of copper. Figure 5.3 shows the same STM images in Fig. 5.2 as with individual color bars, at which the copper morphology is better visible. In some of the images, we also see a particular arrangement of copper islands which is clearly non-random: this is discussed in detail in Section 5.4 and Section 5.6 of this chapter.

After each deposition, 3-4 flakes have been analyzed for statistical merit by flattening and flooding, using WsXM [138] software, and areal and volume coverage of the copper islands has been calculated. The values for areal and volume coverage are plotted against increasing deposition time in Fig. 5.4. We expect a linearly increasing volume coverage with increasing deposition time. For areal coverage we also expect an increasing behavior, but since areal coverage cannot exceed 100%, we expect it to saturate for the data points corresponding to higher copper deposition times. Dashed lines, which are a guide to the eye, are drawn in the plots in Fig. 5.4 indicating this expected behavior for areal and volume coverages.

However, we observe some deviations in the data from the expected behavior. First of all, we do not see any copper for the first 60 seconds of deposition, as shown in the inset of Fig. 5.4(a). Probable reason for this behavior is discussed in section 5.2. Secondly, we see a lower amount of copper than expected for deposition times beyond 700 seconds, which starts rising again after 900 seconds of deposition time. The most likely explanation for this behavior is intercalation. It is a common phenomenon observed in 2D materials, reported in several studies [139, 140]. Since STM is a surface sensitive technique, at

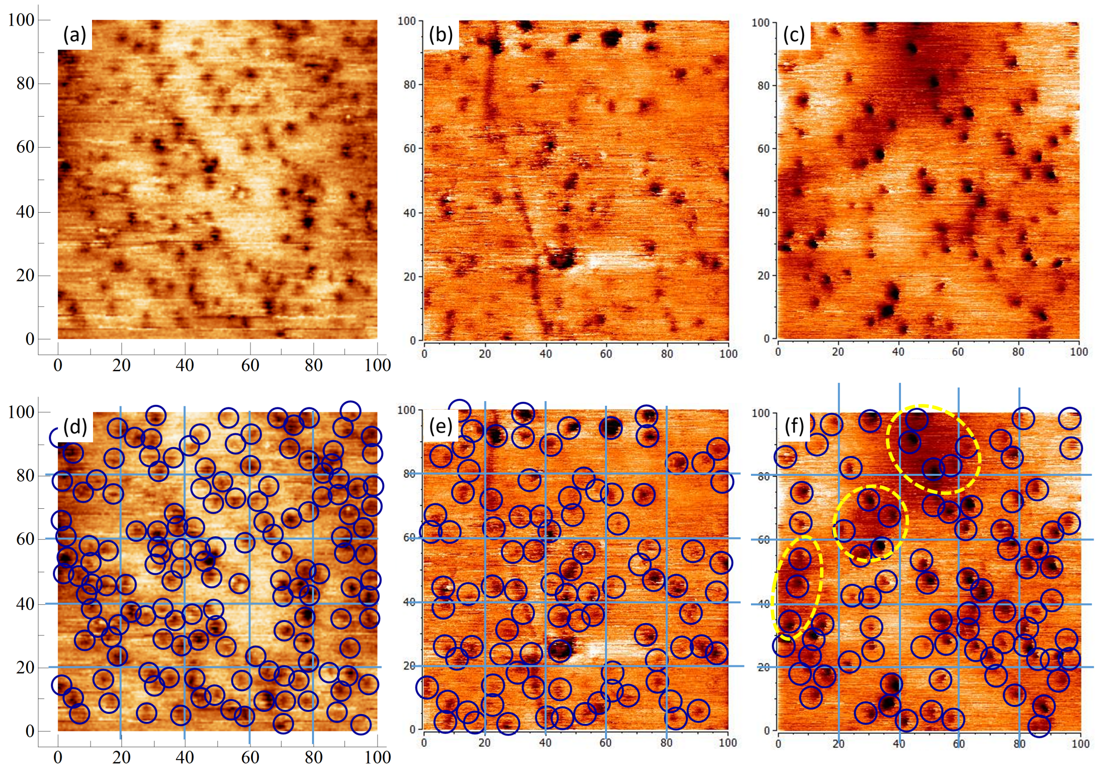

FIGURE 5.5 Defect quantification. 100 nm × 100 nm STM images of bP surface with copper deposition times and scanning parameters of individual images: (a) 0 seconds, (1.0 V, 0.20 nA); (b) 15 seconds, (1.0 V, 0.83 nA); and (c) 30 seconds, (1.0 V, 0.83 nA). The images (d), (e), and (f) are identical to (a), (b), and (c), respectively, on which counting of defects is done. Blue circles indicate individual defects in all three images. The region marked by yellow boundary in (f) indicates depressions commonly observed surrounding these defects.

high coverages, it is difficult to observe intercalation using a STM. However, a recent work has reported intercalation of copper into bP [141].

5.2 Defects in bP

We have always seen defects on pristine bP surfaces, as discussed in Chapter 4. Figure 5.5 shows these defects. Figure 5.5(a) shows a pristine bP surface. Figures 5.5(b) and (c) show the surface of bP after depositing copper for 15 seconds and for 30 seconds, respectively. All these images have the same scan size: 100 nm × 100 nm. Quantification of these defects has been performed by counting individual defects, as shown in Figs. 5.5(d)-(f). On performing a statistical analysis on multiple bP flakes, we found an average of (135 ± 37) defects on the pristine bP surface (data from 6 different bP flakes), (106 ± 11) defects on the bP surface after 15 seconds of copper deposition, and (88 ± 8) defects on the bP surface after 30 seconds of copper deposition. The number of defects is therefore decreasing with increasing copper coverage. Moreover, we do not see any

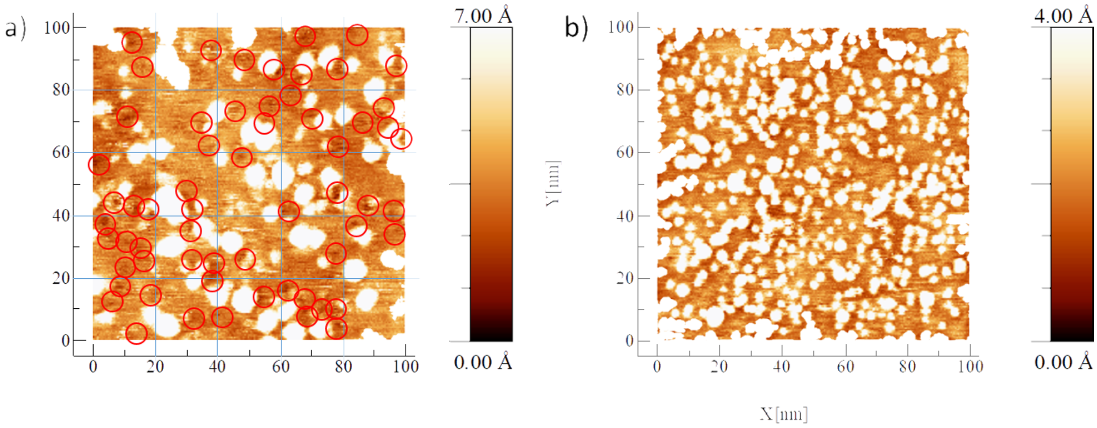

FIGURE 5.6 Copper in bP defects. 100 nm × 100 nm STM images of bP surface partially covered with copper. Scanning parameters of individual images: (a) (1.0 V, 0.83 nA); and (b) (-1.0 V, 0.83 nA). Copper islands can be recognized by in both the images as bright features. In (a), the defects are marked by red circles. In (b), no defects are visible. In both images, depressions can be seen in the background of copper islands. These depressions are characteristics of bP defects as shown in Fig. 5.5(f). They indicate the presence of defects, which are not visible by STM, under the copper islands.

copper on the surface of bP in Fig. 5.5(b) and Fig. 5.5(c) (corresponding to 15 s and 30 s of copper deposition, respectively). These two factors, (i) decreasing defect density with increasing copper deposition time, and (ii) no observation of copper islands on the surface of bP for low copper coverage, clearly points towards the preference of copper atoms to fill atomic vacancies of the bP surface. This also implies that the copper atoms are mobile on the bP surface at room temperature, such that they can move around after deposition and occupy a defect as soon as they encounter one.

On deposition of some more copper on sample, we start noticing copper islands on the bP surface. This is shown in Fig. 5.6. The first image has 21 % of the area covered by copper. In this image, we see some defects next to the copper islands (marked by the red circles). On counting, we found a total of 59 defects, which is only half of the average number of defects on the pristine bP surface. This can be rationalized by the fact that half of the defects are already occupied by copper. However, if we assume random arrival of copper on the sample, then 21 % area coverage by copper implies that only 21 % of defects should be covered, so $\sim$ 79% (or $\sim$ 90 defects) should have been still visible. This indicates that at higher copper coverages, we observe the competition of two effects: on the one hand, copper continues to fill the vacancies in the bP surface, but on the other hand, first copper islands have formed, most likely because the cohesive energy between copper atoms is higher than their energy at the surface of pristine bP. Such Volmer-Weber growth mode is quite common for the growth of metals on semiconductors. This is further evidence for the fact that copper can diffuse on bP at room temperature.

In Fig. 5.6(b), we have ∼ 40 % of the area covered by copper. Under the same assumption as before, this means that ∼ 60 % of the defects should still be visible, but we do not see even a single defect. One could argue that maybe there was no defect present on the bP surface prior to copper evaporation, but we have always seen defects on pristine bP surfaces, as shown in Chapter 4. Also, whenever we see a defect, we see a slight depression surrounding it (indicated in Fig. 5.5(f) by the yellow boundary). In Fig. 5.6(b), we see the presence of similar depressions. So we do not see the defects in the image in Fig. 5.6(b) because they are covered by copper islands, but we do see the signature of the presence of the defects in the form of depressions around copper islands. There are some copper islands in the image which do not have any depressions surrounding them: these are the cases of copper islands which have nucleated on the defect-free bP surface.

5.3 Step decoration

Step decoration is a well known phenomenon reported in surface science studies [142, 143]. It is a result of the fact that atoms at step edges are more reactive compared to atoms in the surface. In a 3D material, an atom located in the bulk is coordinated to other atoms on all sides. But an atom lying in the surface of a 3D material has no other atom on one side. A atom bonding to one such surface atom will have coordination number one. At a step edge on the surface of a 3D material, the same atom can bond simultaneously to two different surface atoms, and can therefore have coordination number two. A higher coordination number means higher stability of adsorbed atoms. So on the surface of 3D materials, adsorbates will line up along the step edges to have higher stability, if the kinetics permits the mobility of adsorbates on the surface.

But in 2D materials, the atoms are bonded only to the atoms lying in the same plane (the atoms across different planes are bonded by weak van der Waals forces only). So, only the atoms at the edge of the surface (for example atoms at the step edges) have unsaturated bonds. This makes the atoms at the edges much more reactive than the atoms on the surface. Therefore the phenomenon of step decoration is even more prevalent in 2D materials.

We have observed the same phenomenon in our experiments. Fig. 5.7 illustrates the step decoration of copper at a bP step edge. Fig. 5.7(a) shows with bright color a higher terrace and with dark color a lower terrace. At the border between the two terraces, we see bright copper islands lining along the step edge of bP. For better contrast, a derivative of the raw image is shown in Figure 5.7(c) in which a 1D chain of copper islands along the bP step edge can be clearly distinguished from the individual copper

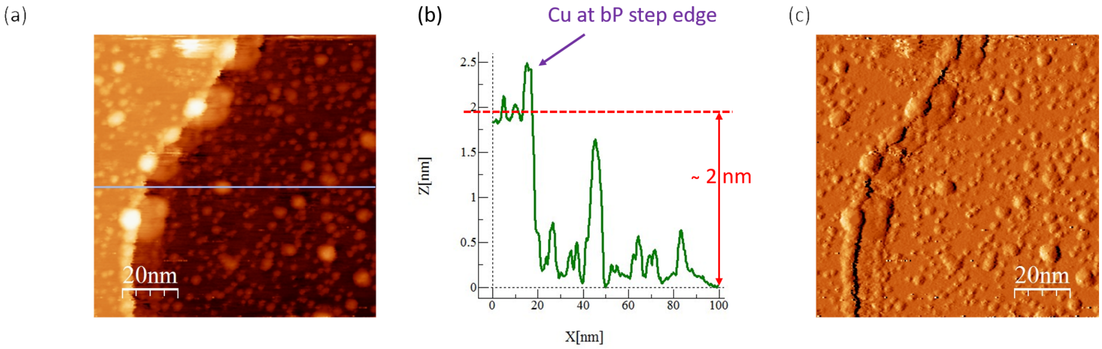

FIGURE 5.7 Step decoration of copper on bP. (a) 100 nm × 100 nm STM image showing a step edge on bP surface after copper deposition for 1200 seconds, which shows copper islands on bP. Scanning parameters: (-1.0 V, 0.33 nA). (b) Height profile across the step edge along the blue line in (a) shows a ∼2 nm step of bP. ∼0.5 nm high copper island at the step edge is indicated by a purple arrow in the plot. (c) Derivative of image (a) with respect to X is shown to enhance the contrast and provide better visualization of copper islands. They appear to be distributed randomly on flat bP surface, while they seem to ornament along step edge forming a queue, which demonstrates decoration of copper at bP step edge.

islands distributed all over the flat bP surface. The line profile across the step edge shown in Fig. 5.7(b) further helps to understand this phenomenon. We see a 2 nm step height which is four times the distance between individual layers in bP. This is a result of step bunching at the step edge. The presence of copper islands at the step edge is exhibited clearly by the line profile, pointed out by the purple arrow in Fig. 5.7(b). This indicates a low diffusion barrier of copper atoms on the bP surface, the same factor which led to the nucleation of copper islands on bP defects, as discussed in section 5.2.

5.4 Copper island alignment

The deposition of copper on the sample using an UHV evaporator is essentially a random process on the surface. However, in many cases, we observed the copper islands to be aligned. One such example is shown in Fig. 5.8. Fig. 5.8(a) shows a flake ∼20 nm high. On zooming in, Fig. 5.8(b) shows a 200 nm × 200 nm surface of bP with copper islands. It is clearly evident that the copper islands are aligned along an angle of 26 ° to the horizontal. On further zooming in to check the crystallographic direction, Fig. 5.8(c) shows a 5 nm × 5 nm surface of bP. The parallel lines, which are blurred zig-zag lines, help us to indicate the crystallographic directions of the bP crystal. It is very clear that the copper islands tend to align along the armchair direction.

This has been observed in multiple occasions. To confirm that this is not due to the movement of copper islands by the tip during scanning, we checked the alignment of copper islands upon changing scan direction. Figure 5.9 shows a series of images taken

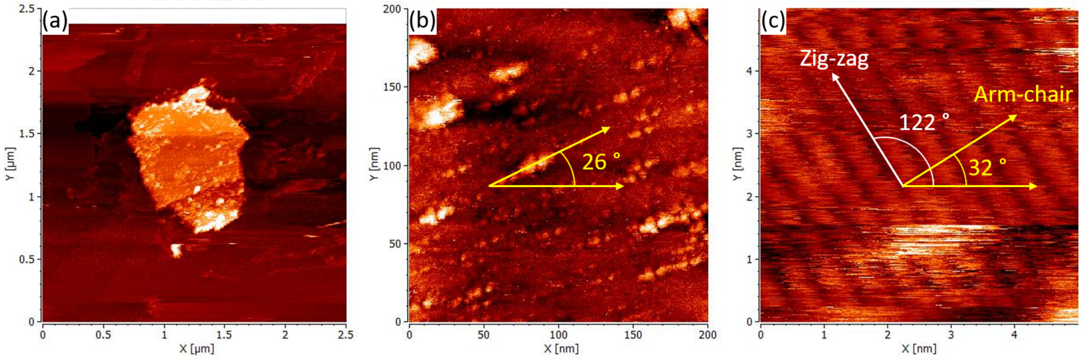

FIGURE 5.8 Copper alignment along armchair direction. (a) 2.5 μm × 2.5 μm STM image showing a bP flake ~20 nm high. Scanning parameters: (1.0 V, 0.83 nA). (b) 200 nm × 200 nm STM image measured after zooming in on the flake. Copper islands seem to be aligned in a direction 26 ° with respect to horizontal direction. Scanning parameters: (1.0 V, 0.83 nA).(c) 5 nm × 5 nm STM image measured after further zooming in on the flake. Scanning parameters: (-1.0 V, 0.83 nA). The parallel lines indicate the crystallographic zigzag direction of bP along white arrow, 122 ° with respect to the horizontal. Yellow arrow is drawn at 90 ° with respect to white line to point towards the armchair direction of bP. Yellow arrows in (b) and (c) seem almost parallel which demonstrates alignment of copper islands along the armchair direction.

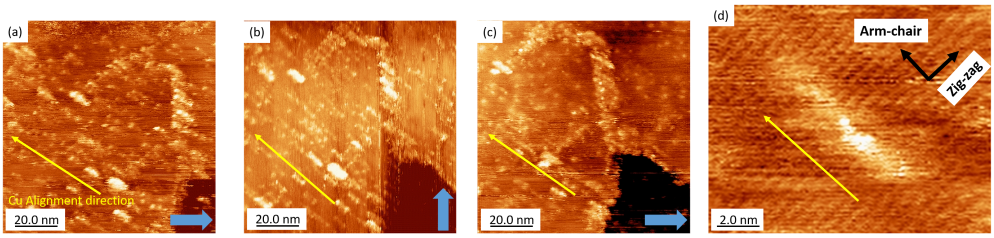

FIGURE 5.9 Copper islands alignment unaffected by STM tip movement direction. Copper islands were scanned with the tip moving along different directions to check if the motion of the tip is causing alignment of copper islands. The same area is scanned with the tip moving horizontally in (a), then vertically in (b), and then again horizontally in (c). The blue arrows indicate the direction of motion of the STM tip while scanning while the yellow arrows indicate the direction of alignment of copper islands. Unchanging copper alignment direction in the three images demonstrates that it is not a tip induced effect. A zoom-in on bP surface to identify the crystallographic direction is shown in (d). The parallel line corresponding to the zigzag direction of bP is almost perpendicular to the direction of alignment of copper islands, which again demonstrates the armchair alignment of copper islands. All images are scanned with the same scanning parameters: (-1.0 V, 0.83 nA).

on the same area with different scan directions. The blue arrow at the bottom right of each image indicates the direction of tip movement, while the yellow arrow indicates the direction of the copper island alignment. The scan area slightly shifts due to drift, but it is very clear that the alignment of copper islands remains unchanged upon changing the tip movement direction, even orthogonally. Furthermore, on zooming in to check the bP crystallographic direction, we again observe in Fig. 5.9(d) that the direction of alignment of copper islands coincides with the armchair direction of the bP lattice.

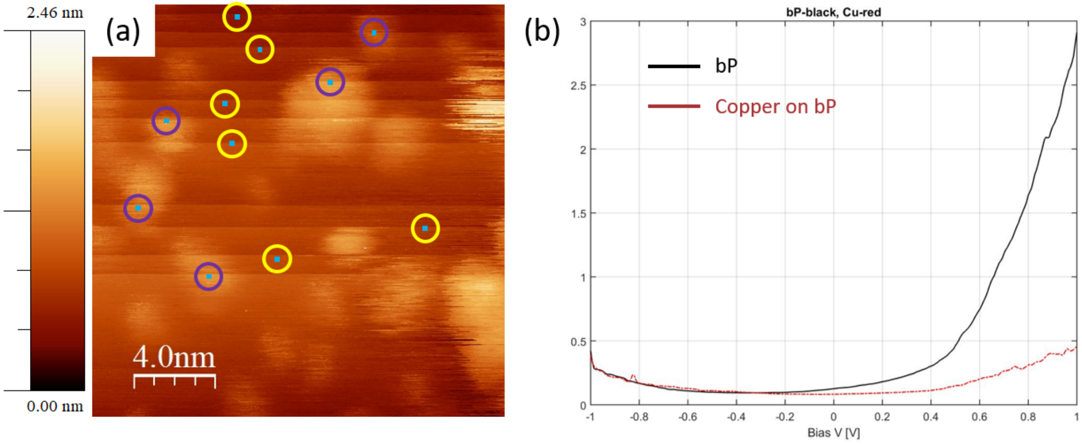

FIGURE 5.10 STS – bP and copper. (a) 20 nm × 20 nm STM image of bP with copper islands showing spots of STS measurements. Green squares mark the spots at which spectra are recorded. Yellow circles and purple circles indicate the spots where spectra were measured on pristine bP and copper islands, respectively. Scanning parameters: (-1.0 V, 0.33 nA). (b) Distinct types of STS curves measured on bP and copper islands. Each curve is an average of 42 spectra.

5.5 Scanning Tunneling Spectroscopy (STS)

Scanning tunneling spectroscopy, as discussed in detail in Chapter 3, is used to measure the local density of states (LDOS) of a system. In this section, we present our investigations of the LDOS of copper on bP.

5.5.1 Point spectroscopy

Figure 5.10(a) shows an STM image of a bP surface with copper islands on top. The blue squares mark all spots on which spectra have been recorded. The spots marked by yellow circles indicate those measured far away from the copper islands. STS measurements carried out at these spots give consistently one class of spectra, which we attribute to pristine black phosphorus. An average of 42 spectra, measured at such points far from copper islands, is shown in Fig. 5.10(b) (black line). We performed the same measurements on copper island, at the spots marked by purple circles. This consistently gives another class of spectra, different from the first class. An average of 42 spectra measured at such points on copper islands is shown in Fig. 5.10(b) (red line). These spectra appear flatter compared to the former spectra taken far away from copper islands, which are more V-shaped.

In the image in Fig. 5.10(a), horizontal flat lines just above the location of each STS measurement can be seen. This is because the STM scanning (from bottom to top) is paused during each STS measurement. When scanning resumes after recording the

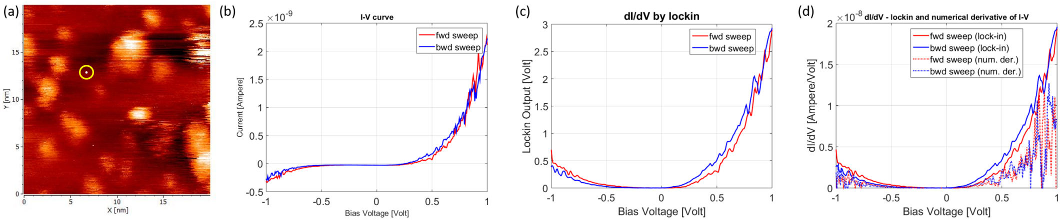

Figure 5.11 Point STS. (a) 20 nm × 20 nm STM image of bP with copper islands showing a spot of STS measurement on bP surface away from copper islands. Scanning parameters: (-1.0 V, 0.33 nA). (b) Plot of current (I) measured against forward and backward voltage (V) sweep. (c) Plot of differential current (dI) against forward and backward voltage (V) sweep measured simultaneously using a lock-in amplifier. (d) Comparison of differential conductance obtained by numerical derivative of (b), plotted using dotted line, and the differential conductance directly measured using lock-in amplifier, plotted using solid line. Signal from lock-in amplifier is more clear because of the noise filtration by lock-in amplifier. Both the curves follow the same trend, which demonstrates the reliability of STS measurement.

STS measurement, the position of the sample has drifted a bit relative to the tip during this time. Due to this, the contrast in pixels in the next scan line appears to have a jump rather than the continuous behavior seen during normal scanning. However, before and after each STS measurement, we have made sure that the spot of the STS measurement stays where intended. As can be seen in Fig. 5.10(a), for all STS spots, the line scans before and after the STS measurement have the same profile: for example, for an STS spot on bP, the surrounding region is flat before and after the measurement, and similarly for a spot on a copper island, the surrounding of the STS spot shows a bright copper island both before and after the measurement. We can therefore neglect the role of drift in these measurements. A more detailed and quantitative analysis of drift present in these experiments is given in section 5.5.2.

Now, let us have a closer look at the spectra taken far away from copper islands. Fig. 5.11(a) shows one such measurement spot marked by a yellow circle, and Fig. 5.11(b) shows one set of I-V curves measured at that position. The forward sweep in red and the backward sweep in blue overlap, which shows the good reproducibility of the STS measurement. Fig. 5.11(c) shows data taken simultaneously using a lock-in amplifier, which gives the derivative of the I-V curve shown in Fig. 5.11(b) (the details of STS measurements using lock-in amplifier are discussed in Chapter 3). Again, the forward sweep in red and the backward sweep in blue overlay, which shows the reproducibility of the measurement. This plot is very helpful since it gives the differential conductance vs. bias voltage, which is proportional to the local density of states. When the value of the voltage is within the band gap of the material, the differential conductance is approximately zero. In our experiments, the bias is applied to the tip, which means that the onset of differential conductance for negative bias voltage values corresponds to the onset of the conduction band, while that for positive bias voltages corresponds to

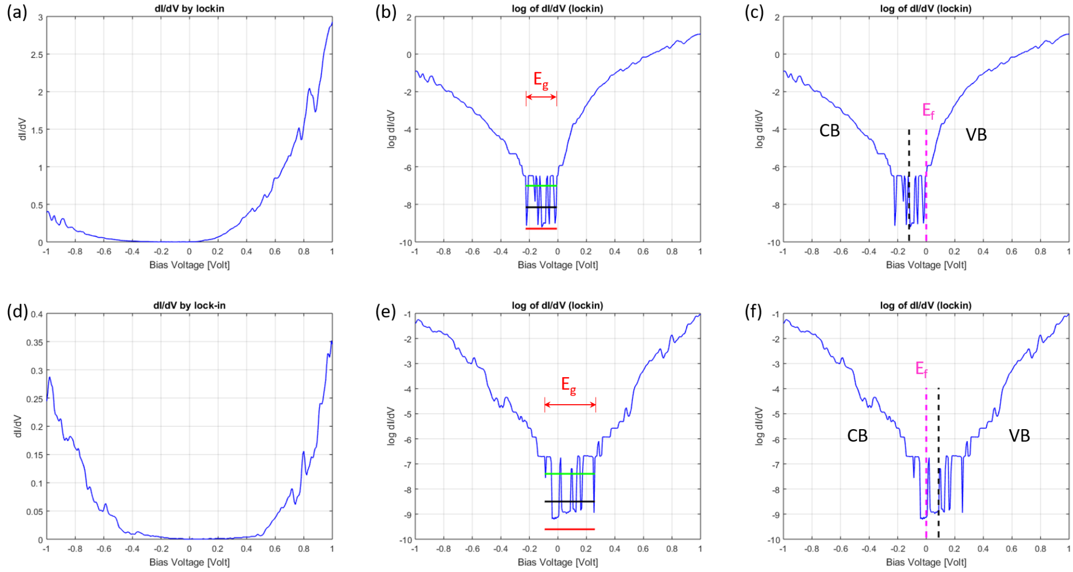

FIGURE 5.12 Bandgap of pristine and doped bP. Analysis of band gap value and doping is shown in (a)-(c) for pristine bP, and (d)-(f) for copper doped bP. Measured spectra of differential conductance using a lock-in amplifier is shown in (a) for pristine bP, and (d) for copper doped bP. The difference in the y-scale distinguishes between the pristine bP-type and doped bP-type spectra. Analysis of band gap value from the measured spectra is shown in (b) for pristine bP and (e) for copper doped bP. The calculated band gap value is indicated. Analysis of doping behavior is shown in (c) for pristine bP and (f) for copper doped bP. Vertical dashed pink line marks the position of the Fermi level, E_F at 0 eV in both plots. Position of E_F close to valence band in (c) indicates p-type doping for pristine bP and close to conduction band in (f) indicates an n-type doping for copper doped bP.

the onset of the valence band. The y-axis of the graph is in units of Volt, because the lock-in amplifier gives the output in terms of voltage. In the graph in Fig. 5.11(d), we compare the numerical derivative of the I-V curve from Fig. 5.11(b) (plotted with dotted lines) with the derivative measured simultaneously by lock-in (plotted with solid lines) for the same set of data. The following parameters have been used to convert the lock-in output from Volts to dI/dV so that it has the same units as the numerical derivative of the I-V curve to be compared to: gain of the STM pre-amplifier $= 3 \times 10^7$ V/A; bias modulation applied to lock-in = 100 mV; and sensitivity setting of lock-in used during the measurement = 200 mV. The close agreement between the curves underlines the reliability of the data measured.

Next, we quantified the bandgap and the chemical potential for each set of measurements. This is shown in Fig. 5.12. The plot in Fig. 5.12(a) shows the derivative of the I-V curve measured by lock-in, for the same set of measurements shown in Fig. 5.11, taken at a spot far away from copper islands. So, this spectrum is attributed to pristine black phosphorus. In Fig. 5.12(b), the same curve is plotted on a logarithmic scale. This is very helpful to identify the region of the curve where the signal is below the noise floor of the current amplifier. As seen in the plot, the noise floor can be clearly identified and well distinguished from the actual signal. This gives information about the band gap and the chemical potential of the system. The bias range in which there is no signal corresponds to the band gap of the material, identified by the region with a signal at the noise floor. To quantify the exact band gap value, the method reported in Kiraly *et al.* [64] is used. First of all we choose the point of minimum signal which lies in the noise floor, as is quite evident by looking at the plot. Then using 10 points surrounding that point on the curve (5 points before and 5 points after), an average value and a standard deviation is calculated for the noise floor. In Fig. 5.12(b), this average value is shown using the horizontal black line in the middle of the noise floor. A horizontal green and red line mark the average plus and minus standard deviation value in the noise floor, respectively. Then, the first and last data point of the curve, for which the y amplitude goes below the green line, marks the opening and closing of the band gap, respectively. The size of the band gap is illustrated in Fig. 5.12(b) by the extension of the three horizontal lines in the plot in the x-direction. Even visually, it can be clearly seen that the length of the horizontal lines approximately marks the length of the noise floor in the curve. This algorithm has been used to quantify the band gap for each set of measurements. In the current case, we obtain a band gap value of $\sim$ 0.2 eV. We repeated the same analysis for 42 such curves (average is shown using a black line in Fig. 5.10(b)) and obtained a band gap value of (0.25 ± 0.10) eV, consistent with the reported bandgap of pristine bP [64]. Figure 5.12(c) shows two vertical dashed lines, one in black indicating the middle of the band gap, and one in pink at 0.0 V bias, indicating the position of the Fermi level of the system. The position of the middle of the band gap, is at approximately -0.1 eV, while the position of Fermi level, indicated by the vertical pink line, is close to the valence band edge, which implies a strong p-type doping of the sample at this position.

Figures 5.12(d)-(f) show a set of curves measured on a copper island. A differential conductance curve on a linear scale is shown in Fig. 5.12(d). Note the different scale in y-axis with respect to Fig. 5.12(a). On performing the band gap analysis for this curve, shown in Fig. 5.12(e), we obtain a band gap value of $\sim$ 0.35 eV (red line in Fig. 5.12(e)). We repeated the same analysis for 42 such curves and obtained an average band gap value of (0.46 ± 0.20) eV, which will be discussed in the next paragraph. Figure 5.12(f) shows the Fermi level close to the conduction band edge, which indicates n-type doping, while the position of the middle of the band gap, as indicated by a vertical black line, is about 0.1 eV.

For copper alone, we would expect a metallic behavior. However, in the spectra measured on the copper islands, the tunnel current is flowing from the tip to the copper islands and then through the bP underneath to the ground. Thus, what we measure is the

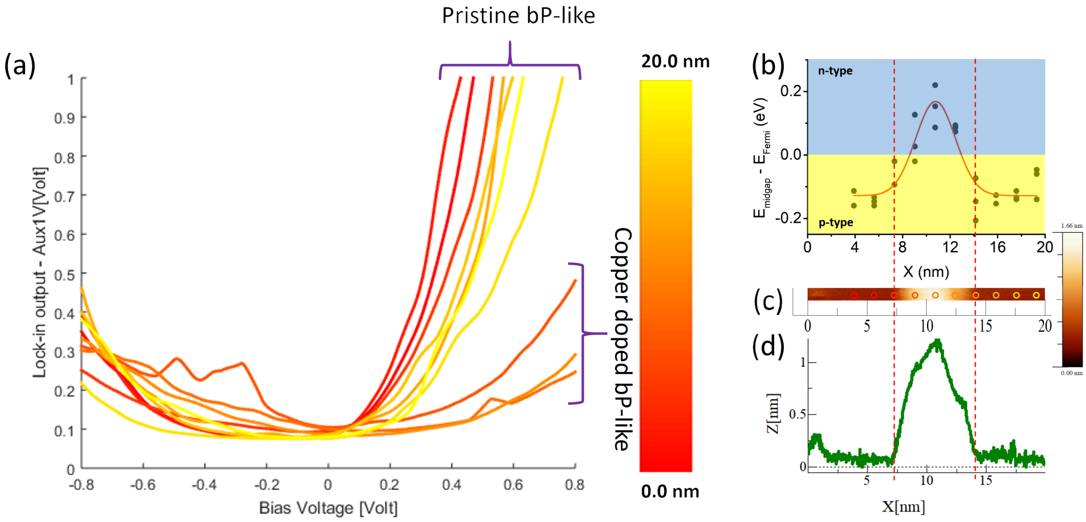

FIGURE 5.13 Line STS - single copper island. (a) Average spectra at each spot of line STS measurement across a copper island in (c) is plotted. Color bar indicates the spectra respective to lateral positions in (c). Red and yellow spectra corresponding to spots on bP show pristine bP-like behavior, and can be clearly distinguished from the orange curves corresponding to spots on copper island, which shows copper doped bP-like behavior. (b) Position of mid-band gap value in individual spectra with respect to the position of the Fermi level is plotted against lateral position where individual spectra are recorded. (c) 5 nm × 1 nm STM image of the copper island on bP is shown on which the line STS measurement is performed. Spots of individual spectra measurement is indicated in a red-to-yellow color gradient. Scanning parameters: (-1.0 V, 0.33 nA). (d) Height profile across the island is shown. The x-axis in (b), (c), and (d) are kept at same scale. Two vertical dashed red lines provide a correlation of the beginning and end of the copper island with the doping behavior, convoluted accordingly.

convolution of both copper and bP electronic structure, and therefore it is consistent to observe a band gap, which indicates semiconducting behavior.

Comparing the results shown in Figs. 5.12(a)-(c), for pristine bP we observe a band gap value of 0.25 eV and a p-type doping, consistent with results in literature for pristine bP [50, 51]. On the other hand, for copper-doped bP, we observe clear evidence of n-type doping of the bP and an increase in the measured value of the band gap to 0.46 eV.

5.5.2 Spectroscopy across islands

Line spectroscopy is an important tool which is used to visualize the lateral variance of the spectral attribute over a feature. In our experiments, we have used this tool to measure the variation in spectroscopy while measuring data points across copper islands. One such example is shown in Fig. 5.13.

Figure 5.13(a) shows a series of line spectra taken across a copper island. The copper island and the lateral position of the individual points at which spectra are recorded is

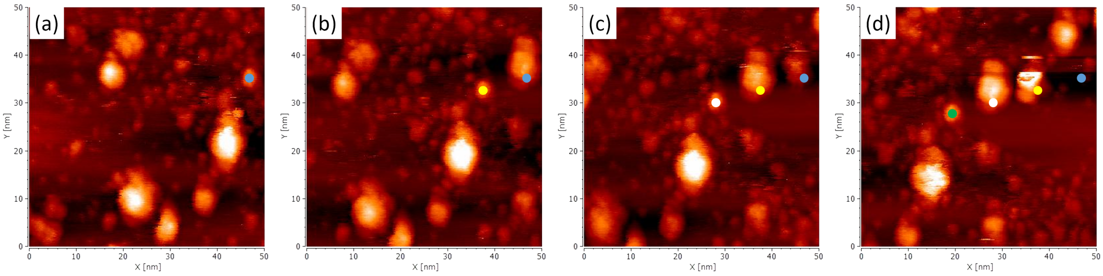

FIGURE 5.14 Drift measurement. 50 nm × 50 nm STM images of bP with copper islands are shown, measured chronologically from (a) to (d). An island is marked in (a) by a blue dot which is identified in subsequent images and marked by a yellow dot in (b), a white dot in (c) and a green dot in (d). The shift in the position of the island indicates a drift towards left in the horizontal direction and downwards in the vertical direction.

indicated in Fig. 5.13(c). The direction of measurement is indicated by a color gradient, from red for the first spectrum to yellow for the last spectrum, going from left to right. At each of these spots, three sets of curves[1] are taken. An average of these three sets of curves gives the spectrum for each spot, which statistically represents the electronic behavior of the spot. The average curves for each spot are plotted in Fig. 5.13(a), colored accordingly to the same color gradient. The spectra in yellow and red (at extreme positions of the line spectroscopy), corresponding to spots on bP, are V-shaped, while the spectra in orange (at the middle of the line spectroscopy), corresponding to copper, are flatter, similar to what was shown in Fig. 5.10.

We performed an analysis of doping from these spectra. We measured the position of the middle of the band gap relative to the Fermi level (0 eV) for individual sets of curves, which gives three values for each spot along the line spectrum. These values are plotted in Fig. 5.13(b). The x-axis indicates the lateral position of each spot of line spectroscopy. Recalling from section 5.5.1, a negative mid-band gap value corresponds to p-type doping, while a positive mid-band gap value corresponds to n-type doping. In the plot in Fig. 5.13(b), we see initially a p-type behavior, which changes to n-type behavior in the middle, and finally again becomes p-type behavior at the end. Figure 5.13(d) shows a line height profile taken across the copper island shown in Fig. 5.13(c). Comparing the onset of change in doping behavior to the line profile, as indicated by two vertical dashed red lines in Fig. 5.13, the lateral positions of the onset of doping match well with the extremity of the copper island. A Gaussian curve is fitted to the data in Fig. 5.13(b), plotted in red color. The position of the Gaussian peak is (10.78 ± 0.17) nm, which also coincides excellently with the center of the copper island. This demonstrates very well that the copper islands are responsible for the n-type doping of bP.

---

[1] One set of curves is one complete forward and backward sweep.

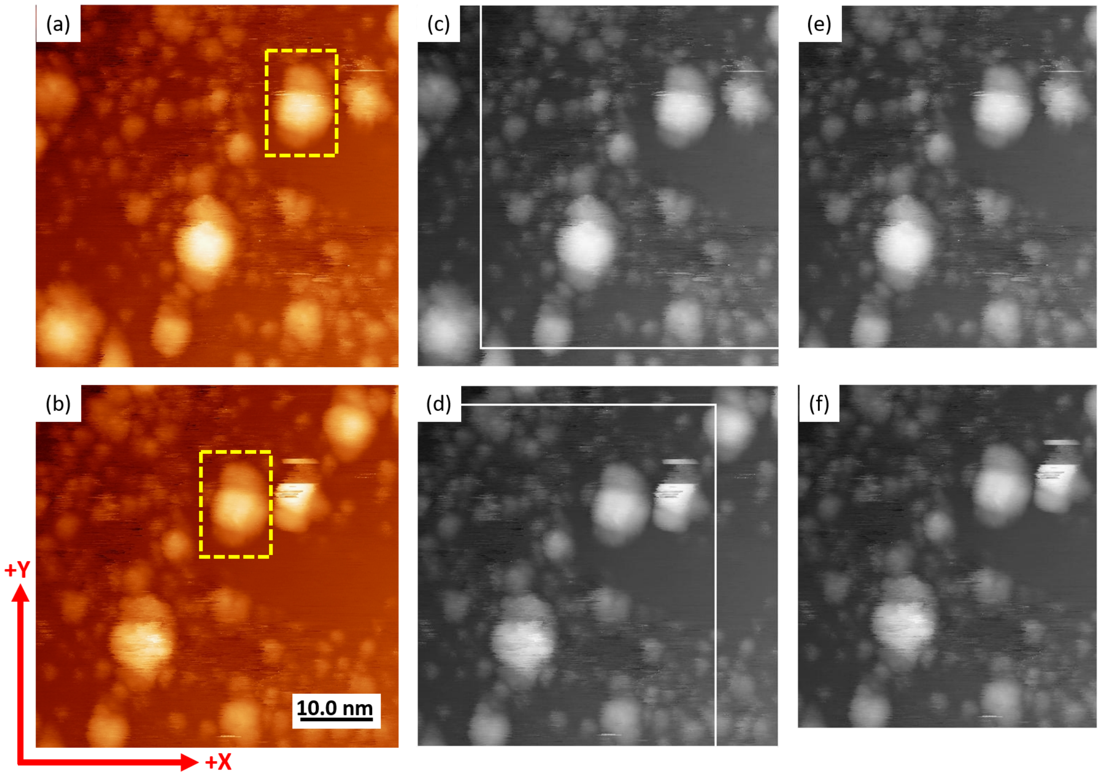

FIGURE 5.15 Drift quantification on 50 nm × 50 nm STM images of bP with copper islands are shown. (a) and (b) shows two successive images measured on the same spot after an interval of 35 minutes. One copper island is identified (indicated using a dotted yellow rectangle), which is identical in both the images. The shift in the position of the island indicates a drift towards negative x-axis and negative y-axis. (c) and (d) shows the images (a) and (b), respectively, converted into grey color scale and analyzed using MATLAB to identify the common regions of both the images. The shift in the position of the common area of the images is quantified as drift. The common area in (c) and (d) are shown using a white rectangle, and reproduced in (e) and (f) respectively. The striking similarity in the common area shown in (e) and (f) despite the differences in parent images (a) and (b) illustrates the well execution of the quantification of drift performed by the MATLAB program. Scanning parameters: (-1.0 V, 0.33 nA).

The matter of drift during STS measurements has already been addressed briefly earlier in this chapter. But it becomes much more prevalent in the case of line spectroscopy when the scanning is paused not for just a single spectrum but for 10 or 20 spectra. Therefore, a more detailed drift analysis is required, which is discussed in the next paragraph.

Figure 5.14 shows four STM images recorded one after the other at the same location. The position of one selected copper island is tracked in successive scans, which is marked by a blue dot in Fig. 5.14(a). In the next image, in Fig. 5.14(b), the copper island has moved to a new position marked by a yellow dot. The blue dot is also shown in this image, which marks the initial position of the same copper island, as seen in the previous image. The same process is repeated for the next two images in Fig. 5.14, showing the new position of the copper island by white and green dots in (c) and (d), respectively.

Figure 5.15 shows the analysis of drift quantification performed using a MATLAB program. Figures 5.15 (a) and (b), which correspond to the images Fig. 5.14(c) and Fig. 5.14(d), respectively, are two successive 50 nm × 50 nm STM images of bP with copper islands, measured on the same spot after an interval of 35 minutes. One of the copper islands, which appears in both images, is indicated by a dotted yellow rectangle. In the absence of drift, two STM images taken on the same spot should appear exactly identical. The shift in position of the island therefore indicates a drift towards left in the horizontal direction and downwards in the vertical direction. Since a drift causes a lateral shift of the features, two STM images taken on the same spot in presence of drift should have only a fraction of area which overlap. The fraction of this common area should get smaller with increasing drift. So, identification of the common area and the measurement of the shift in the common area leads to quantification of drift. This has been done using a MATLAB program. First, the original images (a) and (b) are converted into grey scale, as shown in (c) and (d), respectively, and the values of each pixel of the images are obtained. The images are then overlaid on each other, such that each pixel of one image lies on a corresponding pixel of the other image. On subtracting the values of individual corresponding pixels of both images and dividing by the total number of pixels, we get a mean difference in the pixel values, called Φ. This mean value Φ will be minimum when the two images align exactly to each other. The images are then translated horizontally and vertically with respect to each other in steps of a single pixel, and Φ is calculated as a function of shift for the portions of the images which overlap. The minimum value of Φ indicates the maximum alignment of the images and the corresponding shift values indicate the drift. The overlapping area of the images is represented by white rectangles in Fig. 5.15 (c) and (d) and reproduced separately in Fig. 5.15 (e) and (f). The copper islands and their lateral distribution in (e) look identical to those in (f), which illustrates the high performance of the MATLAB program to identify the common area. Similar analysis has been performed for the pair of images: Figs. 5.14(a), (b) and Figs. 5.14(b), (c) as well, which gives an average drift of (-0.26 ± 0.12) nm/min in the x-axis and (-0.07 ± 0.00) nm/min in the y-axis during this measurement.

The calculated drift has been used in the analysis of line STS measured soon after. The lateral position of each spot of measurements is corrected for drift using: (a) the initial position of the measurement spots, (b) the rate of drift calculated in the previous analysis, and (c) individual spectra measurement times. Figure 5.16 shows a line spectroscopy measurement recorded across two copper islands. Figure 5.16(a) shows an STM image where two islands are indicated by a semi-transparent blue box. The same region is cropped and rotated, as shown in Fig. 5.16(d). Line spectra are recorded, starting from

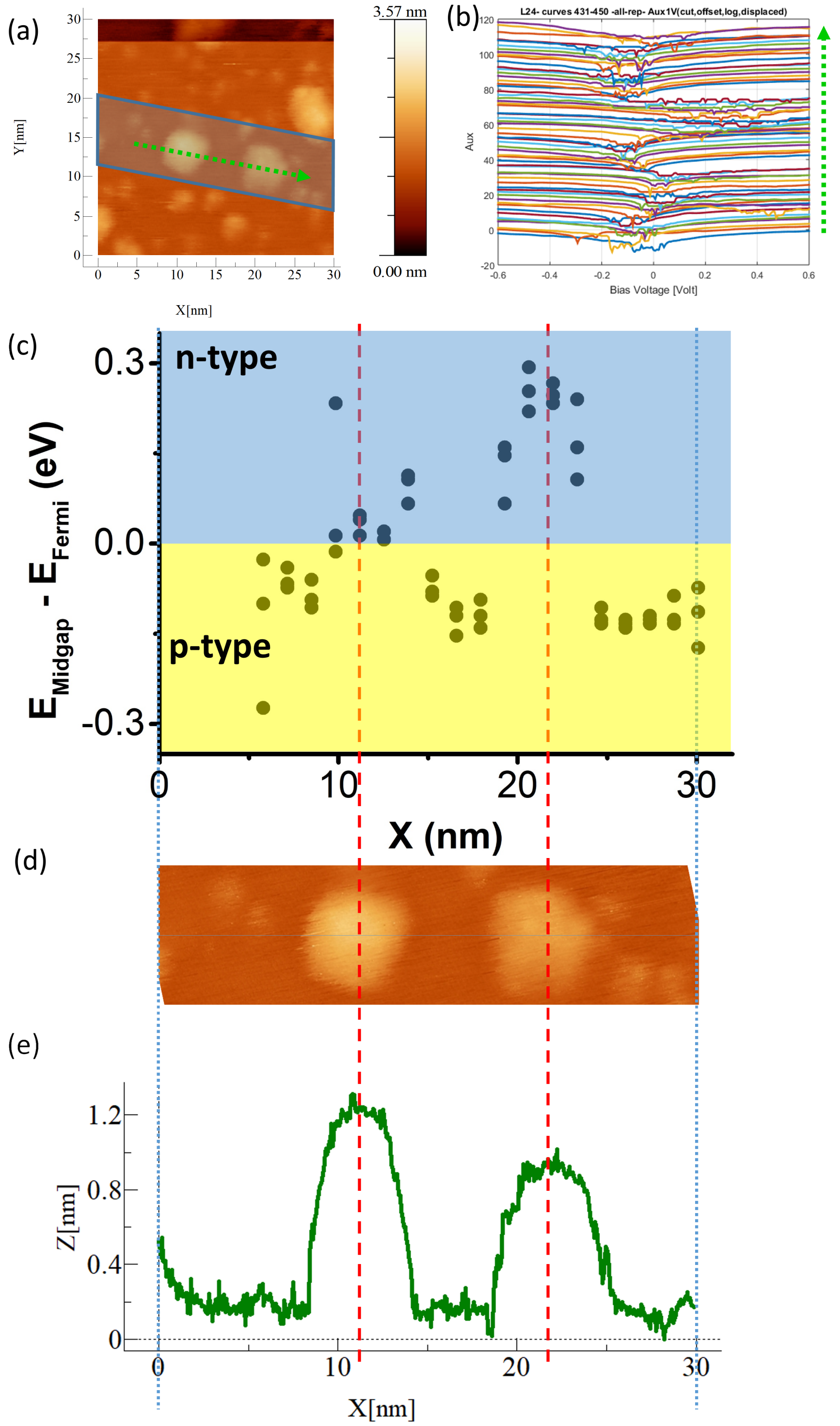

FIGURE 5.16 Line STS - double copper island. (a) 30 nm × 30 nm STM images of bP with copper islands shows a location where a line STS measurement is carried out across two copper islands. The path of spectroscopic measurement is shown using a green dotted arrow. (b) Individual spectra are plotted in log scale and displaced vertically for visualization. A smooth transition can be seen in the successive spectra due to passage from bP to copper and then back to bP, twice. (c) Position of mid-band gap value in individual spectra with respect to the position of the Fermi level is plotted against lateral position where individual spectra are recorded. (d) A zoom-in of the region marked by blue area in (a) is shown. The image is rotated to place the two copper islands horizontally. (e) Height profile across the islands in (d) is shown. The x-axis in (c), (d), and (e) are kept at same scale. Two vertical dashed red lines provide a correlation of the peak of the n-type behavior with center of the copper islands.

a spot on bP on the left of the two islands, moving rightwards across both islands, and ending at another spot on bP lying on the right of the two islands, as indicated by a dotted green arrow in Fig. 5.16(a). Again three sets of curves are recorded at each spot, and all curves are plotted on a log scale in Fig. 5.16(b). Subsequent curves are displaced for better visualization. The green arrow indicates the position where curves where measured along the direction indicated in Fig. 5.16(a). Starting from the bottom most curve, corresponding to a spot on the left of the copper islands, the band gap region shifts to the right as it approaches the first copper island, and then goes back to the left on reaching the boundary of the copper island. It repeats the same behavior on going through the second island. In Fig. 5.16(c), the value of mid-band gap relative to the Fermi level (0 eV) is plotted for each set of curves against lateral position. We see a shift from p-type behavior to n-type behavior, twice. Figure 5.16(e) shows a line profile across the two copper islands. On comparing the peak positions of n-type behavior in Fig. 5.16(c), using vertical dashed red lines, we understand that it coincides well with the center of the island, as seen in the STM image in Fig. 5.16(d) as well as in the line profile shown in Fig. 5.16(e). This further demonstrates that the n-type behavior is due to the copper on bP.

5.6 DFT calculations

To complement the experimental observations and gain a deeper understanding on copper doping, we collaborated with Dr. Deborah Prezzi, working at CNR-Nano Modena, who investigated from first principles both the stability and electronic properties of copper doped bP using a plane-wave, pseudopotential implementation of density functional theory (DFT) [144, 145], as available in the Quantum ESPRESSO package [146, 147].

We studied the effect of three possible copper sites on few-layer bP, that is: (i)substitutional copper (Cu-s), where a copper atom occupies a missing phosphorus atom (vacancy) site; (ii) interstitial copper (Cu-i), with the copper atom sitting in between two layers; (iii) copper adsorbed on the bP topmost layer. For the latter we have explored four different sites with respect to the bP surface, i.e. hollow (H), top (T), and two different bridge positions (B1 and B2), as shown in Fig. 5.17, where the values of the binding energies, E_b are also reported.

The most stable impurity is the substitutional copper, with $E_b(s)$ = -4.48 eV, which suggests that a vacancy on the bP surface is likely to be filled by a copper atom. This is consistent with the preferential filing of defects observed in our STM experiment. Intercalated copper represents a highly stable impurity as well, with a value of $E_b(i)$ = -3.52 eV. Regarding copper adsorption, finally, the most stable site is the hollow one,

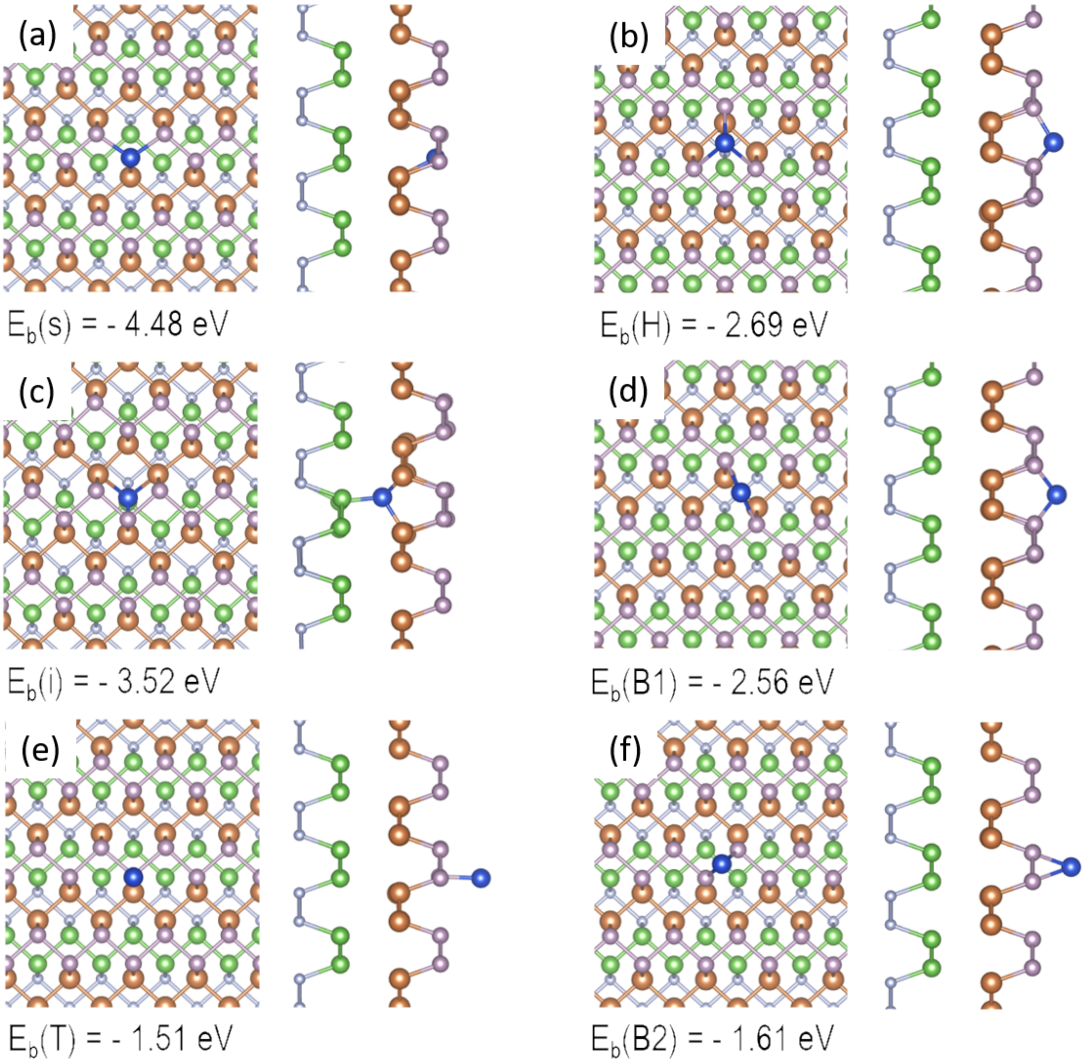

FIGURE 5.17 DFT calculated binding energies of single copper atom on bP in different configurations: (a) copper atom substituting a phosphorus atom; (b) copper atom adsorbed on hollow site on bP surface; (c) intercalated copper atom; (d) copper atom adsorbed on bridge-1 site; (e) copper atom adsorbed on top site; (f) copper atom adsorbed on bridge-2 site. A side view for each configuration is also shown.

with a value of $E_b(H) = -2.69$ eV. The comparison of the last two values suggests that a copper atom would preferably intercalate with respect to adsorbing on the bP clean surface.

Apart from the most stable adsorption site, also the energetics of the other adsorption sites is interesting to analyze. In fact, while it does not give precise information on diffusion barriers, for the estimation of which different approaches are requested (e.g. nudged elastic band method [148, 149], we can nonetheless extract some indication. In particular, we notice that H and B1 differ by about 130 meV, while other configurations are much less favored.

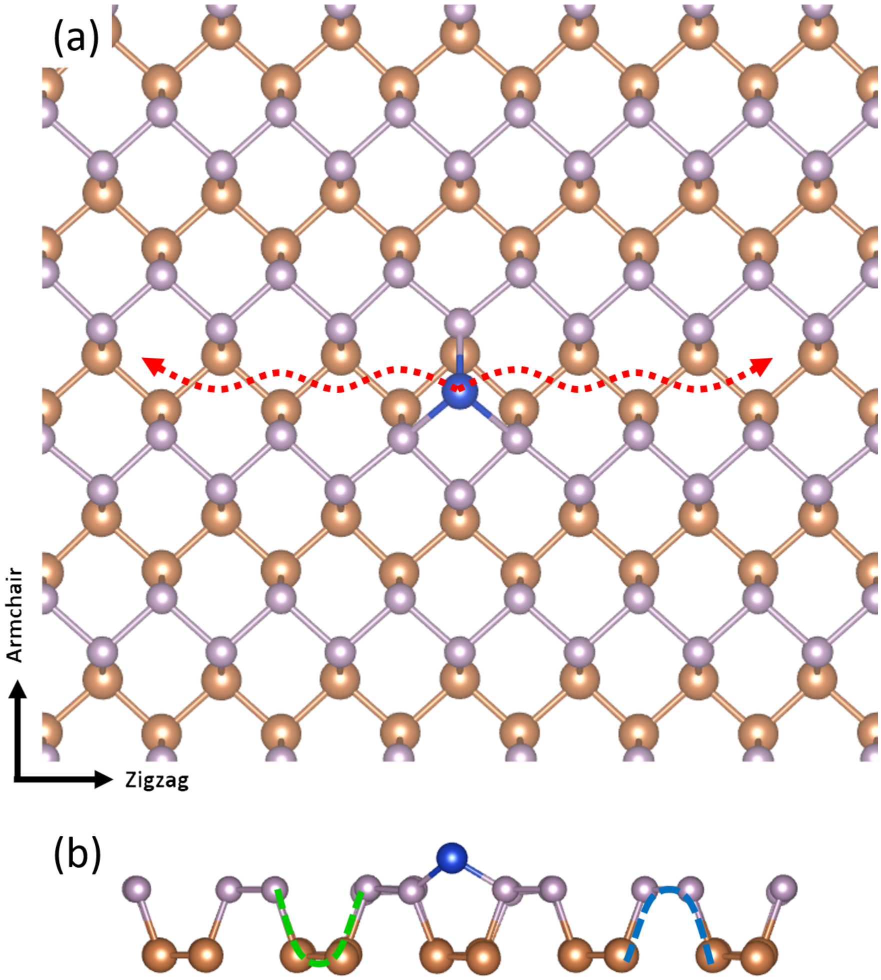

FIGURE 5.18 Copper diffusion along the zigzag direction is shown using a red dotted arrow in (a). A trench and a dune are indicated using a dashed green and blue line in (b).

We consider the motion from one H site to another. We can see in Fig. 5.17 that each H site is surrounded by two B1 sites, two B2 sites, and four T sites. The binding energy for B2 and T site is much lower. Since B1 is more bound, with a binding energy closer to H as compared to the B2 and T sites, it would be easier for a copper atom to go from one H site to another using pathway: H-B1-H. But again, after moving once, the copper atom lies in an identical situation, which means that it would prefer to take an identical pathway to diffuse further: H-B1-H-B1-H-B1-H..., as illustrated in Fig. 5.18(a) using a dotted red arrow. Comparing this to the bP lattice, the direction of diffusion corresponds to the zigzag direction. This means that a copper atom prefers to diffuse along the zigzag direction, moving in the same trench in which it lies initially. A trench and a dune are shown in Fig. 5.18(b) using a green and a blue dotted shape, respectively.

DFT calculations have also analyzed the effect of copper on the electronic structure of few-layer bP. Copper is found to cause n-doping of bP when adsorbed in H position

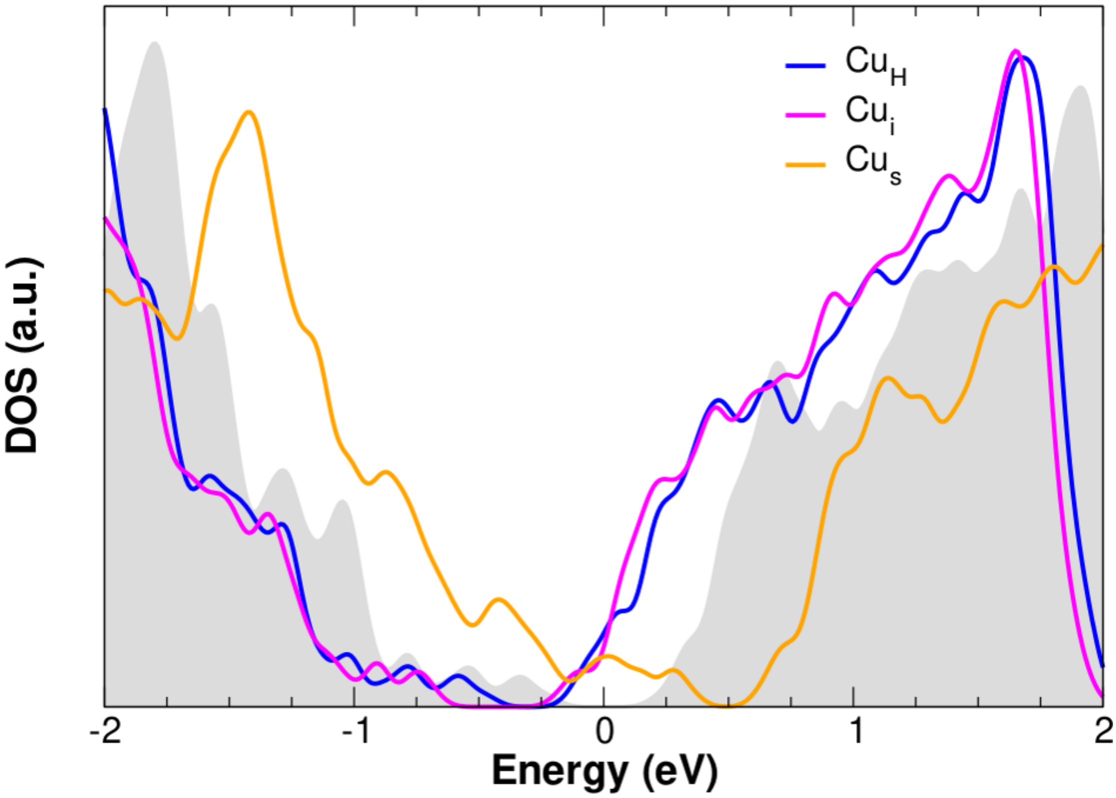

FIGURE 5.19 Density of states (DOS) calculation is shown for pristine bP (2L) in grey, for copper adsorbed on bP surface at H-site in blue, for interstitial copper in pink and for substitutional copper in yellow.

(blue curve, Fig. 5.19), with the Fermi level (E_F) lying $\sim$ 0.2 eV above the conduction band bottom (CBB), in agreement with previous reports [65]. At the same time the gap decreases from 0.21 (i.e. pristine) to 0.12 eV. The interstitial Cu impurity is also predicted to induce n-doping in bP, with the E_F being $\sim$ 0.3 eV above the CBB. At variance with the adsorbed impurity, for the interstitial one the gap increased to 0.26 eV. Finally, the substitutional copper defect induces a gap closure to about 40 meV, with the E_F lying $\sim$ 0.47 eV below the valence band top (VBT), which indicates a p-type doping.

We remark here that, in order to have a more complete picture regarding intercalation and adsorption phenomena including cluster alignment, many more situations should be taken into account, e.g. one should also investigate the dependence of the binding energy on defect concentration, as well as consider adsorption at substitutional copper and formation of larger clusters. These and other calculations are currently ongoing.

5.7 Discussion

An n-type doping in bP caused by copper is reported by Koenig *et al.* [65] through transport measurements. But no surface investigation has been performed so far to understand the copper morphology on bP. We have deposited copper on exfoliated bP flakes and performed a morphological study of copper on bP. We observed atomic resolution on bP after depositing copper, which confirms the high quality of the bP surface even after copper deposition.

At low copper coverage, we do not detect any copper, but we observe a decrease in the number of defects on the bP surface with increasing copper coverage. This indicates a filling of defects on the bP surface by copper atoms. This is also supported by a high binding energy of substitutional copper atoms from the DFT calculations, which shows that such a process is energetically preferred. At slightly higher coverages, we do not observe any defect anymore, but depressions which are signatures of defects, indicating the presence of defects below copper islands. This further indicates the preference of copper to occupy bP defect sites. This also implies that copper atoms are mobile on bP at room temperature.

We studied the morphology of copper on bP with increasing copper coverage. We also performed a statistical analysis of areal and volume copper coverages on the bP surface. We noticed some deviations from the expected behavior. At high copper coverages, we observed a lower amount of copper on bP than expected. This could be because of intercalation, which is also suggested by the DFT calculations, and reported by Koenig *et al.* [65] and Lin *et al.* [150]. However, we did not observed any evidence of intercalation experimentally, probably due to the copper on the surface, which makes it difficult to observe intercalation by a surface sensitive technique like STM.

We observed decoration of bP step edges by copper, which further indicates that copper is mobile on bP. We also observed an alignment of copper islands on the bP surface along the crystallographic armchair direction of bP, and confirmed that this is not caused by the tip. From the DFT calculations, we compared the binding energy for different configurations of copper atoms on bP. The energetics of these configurations suggests that copper prefers to diffuse along the zigzag direction. Kiraly *et al.* [122] has performed a similar study of diffusion of potassium atoms on bP and reported that potassium atoms prefer to diffuse along the zigzag direction.

To understand the effect of copper on the band structure of bP, we performed STS measurements. We noticed a clear distinction between spectra of pristine and spectra taken on copper islands. We measured a band gap of 0.25 eV and p-type doping for pristine bP, consistent with literature values [50, 51]. For copper on bP, we see an n-type doping and an increase in the measured band gap value to 0.46 eV.

On performing line STS measurements across single and double copper islands, we observed a transition from p-type to n-type and back to p-type behavior in the chemical potential of the sample within a few nanometers, which coincides excellently with the boundaries of the copper islands. Also, the peak of the n-type behavior matches well with the center of the copper islands. This demonstrates that it is copper islands which are responsible for the observed n-type doping of bP by surface charge transfer from copper, and it also indicates the length scale over which the effect of isolated copper islands on bP is prominent.

We should be careful about the interpretation of the measured band gap value of 0.46 eV recorded on copper islands on bP, because we measure the current flowing across a metallic copper islands, then an n-type doped bP and then the bulk of the bP flake which is p-type. This might induce a p-n junction type behavior in measured the spectra. In that case, we would expect an increase in the asymmetry of the I-V curve and consequently, also in the dI/dV curve. But on comparing the dI/dV curves measured on bP and copper islands, as is clearly visible in Fig. 5.10(b), not only we do not observe any increase in asymmetry in the dI/dV curve, but in fact it becomes even more symmetric on the copper. This indicates that a p-n junction formation is not a dominating factor in the electronic behavior measured on copper, and thus the measured band gap broadening could be a feature of the n-type doped bP itself. A first hint that copper could induce not just a Fermi level shift but also a band gap broadening comes from the ab initio DFT calculations that are shown in Fig. 5.19, where a fraction of intercalated copper is predicted to cause both n-type doping and band-gap broadening. However, further analysis is necessary to pinpoint the reason behind the observed band gap broadening and to understand if other effects are contributing to the measured electronic behavior of copper on bP.

Chapter 6

Summary and Outlook

6.1 Summary

In this work, we carried out sample preparation procedures in an inert atmosphere, which preserved the bP from degradation. We used a glove bag to facilitate an inert atmosphere, which is much cheaper than a glove box setup. The prepared samples were also mounted on the STM sample holder and carried to the STM chamber in the same inert atmosphere, to minimize any degradation of samples due to exposure to ambient atmosphere. The effectiveness of our sample preparation protocol is reflected in the high quality of the STM images on thin flakes of bP achieved in our experiment. Thus, we demonstrate an inexpensive solution to prepare clean surfaces of exfoliated thin flakes of bP suitable for STM and other surface investigations, which eliminates the compulsion to work with encapsulated bP or cleaved bP samples.

Performing a statistical analysis of the size of the bP flakes, we measured height and area of $\sim$ 40 flakes and found that our flakes are typically 30 nm high and 1 μm^2 in area. Upon zooming in, we performed atomic resolution imaging on bP flakes, and measured the unit cell parameters: $a = (3.45 \pm 0.43)$ Å and $c = (4.40 \pm 0.12)$ Å, consistent with the reported values. To distinguish the bP from the substrate, we also obtained atomic resolution on graphene, and measured the unit cell parameter, $a = (2.46 \pm 0.22)$ Å, which is also consistent with literature.

While investigating pristine bP surfaces, we studied the thermal stability of few layer thin bP flakes and changes in their surface morphology with increasing annealing temperature using an STM in UHV conditions. We have shown STM images of bP surfaces after annealing in steps of 50 °C, starting from 200 °C, till 500 °C. We observed that 300 °C-350 °C annealing is suitable for cleaning bP surfaces from residual oxides, which gives clearer subsequent STM images. We also observed defects on the bP surface, which are probably due to phosphorus vacancies.

Upon annealing at ∼400 °C, we observed the formation of monolayer deep anisotropic craters by phosphorus desorption. Being one order of magnitude smaller than those reported in literature, these craters are the initial stages of the reported craters. By statistical analysis, we found that these craters are aligned to each other. We imaged these craters with changing tip movement direction to rule out the possibility of crater modification by the tip. Taking advantage of the high resolution of imaging provided by STM, we obtained atomic resolution imaging on a bP surface near one of these elongated craters. With this, we were able to relate the alignment direction of the long axis of these anisotropic craters to the crystallographic zigzag direction of bP. This enabled us to solve an existing debate in literature on this topic.

We also discussed an existing model relating the atomic P desorption mechanism with the formation of elongated craters along the armchair direction. We evaluated the order of removal of unsaturated P atoms in different configurations considered in the model. On comparing it with the DFT calculated activation energy values for such processes, we established the proper order for removal of P atoms in different configurations and found that atomic P desorption leads to the formation of craters along the zigzag direction. However, the DFT and KMC simulation results suggest that molecular P_2 desorption also leads to elongated crater formation along the zigzag direction. This indicates that what earlier appeared so trivial, that the atomic P desorption leads to crater alignment along the armchair direction and the molecular P_2 desorption mechanism to crater alignment along the zigzag direction, is not so simple, as both desorption mechanisms cause crater alignment along the zigzag direction. STM imaging alone is not enough to pinpoint the underlying mechanism. However, the energetics of the two mechanisms reported by Fortin-Deschenes *et al.* [115] indicates that a molecular P_2 desorption mechanism is energetically more favorable.

We also studied transfer doping of bP by copper. We deposited copper on exfoliated bP flakes and performed a morphology study of copper on bP. After deposition of 1200 seconds of copper, we found a majority of copper islands with dimension: (0.47 ± 0.12) nm height and (2.19 ± 0.34) nm width. There were few larger islands with dimension: (2.00 ± 0.25) nm height and (7.20 ± 0.98) nm width.

We obtained atomic resolution on bP after depositing copper, which confirms that the high quality of the bP surface is maintained even after copper deposition. But the atomic resolution of bP is only on bare bP and not on the position of copper islands, which indicates that the copper stays on top of the bP surface. Also, the multilayer height of copper islands indicates island growth of copper on the bP surface instead of copper intercalation.

We studied the morphology of copper on bP on three different samples and for 18 different copper deposition times. We also performed a statistical analysis of areal and volume coverages on bP against increasing copper deposition time.

We observed some deviations from the expected behavior of areal and volume coverages. At low copper coverages, we did not detect any copper initially in the STM images. However, we observed a decreasing number of defects on the bP surface with increasing copper coverage. This indicates the filling of defects on the bP surface by copper atoms. This is also supported by a high binding energy of substitutional copper atoms as per the calculation using DFT, which shows that such a process is energetically favorable. At slightly higher coverages, we did not see any defects but we see depressions which are signatures of defects lying below copper islands. This further indicates that copper prefers to occupy bP defects. It also implies that copper atoms are mobile on bP at room temperature.

We also observed step decoration of copper atoms at bP step edges. This further indicates mobile copper on bP. From the energetics of various positions of copper atoms on bP, as calculated using DFT, copper might prefer to diffuse along the zigzag direction. Kiraly *et al.* [122] has performed a similar study of diffusion of potassium atoms on bP and reported that potassium atoms prefer to diffuse along the zigzag direction.

At higher copper coverages, we observed a lower amount of copper on bP than expected. This could be because of intercalation, which is a fairly common phenomenon in 2D materials like graphene [139, 140]. This is also suggested by a high binding energy of interstitial copper atoms from the DFT calculations, as well as reported by Koenig *et al.* [65] and Lin *et al.* [150]. However, we observed that copper islands stay on the surface at low coverages. Also, since STM is a surface sensitive technique, it is difficult to observe intercalation at higher coverages, when there are already copper islands on the surface.

We observed the alignment of copper islands on bP along the crystallographic armchair direction of bP. On another flake, we performed STM imaging of aligned copper islands with changing tip movement direction. Unchanging copper alignment with changing tip movement direction rules out any possibility of such a behavior caused by the tip. On zooming in, we observed atomic resolution of bP and again found an alignment of copper islands along the armchair direction. This confirms the armchair alignment of copper islands.

To understand the effect of copper on the bandstructure of bP, we performed STS measurements. We noticed a clear distinction between spectra from pristine and doped bP. We measured a band gap of 0.25 eV and p-type doping for pristine bP, consistent with literature values. For copper doped bP, we see an n-type doping and an increase in measured band gap value to 0.46 eV.

On performing a line STS measurement, starting from bP and going across a copper island, we observed a transition of spectra from bP-type to copper type, and again to bP-type when coming back to bare bP. The chemical potential obtained from these spectra plotted against the lateral position where spectra were recorded was compared with the height profile taken across the copper island. We saw a clear correlation in the transition from p-type to n-type behavior with the onset of a copper island and back to p-type behavior at the boundary of copper island. This demonstrates that it is the copper which is responsible for the n-type doping of bP.

We also analyzed drift in STM images, which becomes important in long spectroscopic measurements. We studied one such long spectroscopic measurement across two copper islands, and with the required drift correction, to compare the spectroscopic features with lateral positions. In the plot where the individual spectra were plotted in log scale (and displaced for visualization), we saw a smooth transition from p-type to n-type and then back to p-type behavior, twice, because of the presence of two copper islands. Another plot of chemical potential against lateral position is compared with the height profile taken across two islands, in which the peak of the n-type behavior matches exactly with the center of copper islands. This shows the repeated observation of same behavior and further establishes the n-type behavior in copper due to bP. Locally, it indicates the length scale of few nanometers over which the effect of isolated copper islands on bP is prominent.

Thus, our study provides a detailed study of bP surface morphology with temperature. It also investigates in detail the transfer doping of exfoliated flakes of bP by copper, studying both morphological and electronic aspects at the nanoscale.

6.2 Outlook

Our work provides an inexpensive and reliable method to make samples with thin bP flakes in which the high quality of the surface is maintained, ideal to perform surface investigations of thin flakes of bP. This removes the limitation of depending on cleaving of bulk bP crystals to have a clean and non degraded surface of bP to perform surface studies. With this technique, it is much easier to obtain clean surfaces of high quality in thin exfoliated bP flakes. This allows investigation of surfaces of thin exfoliated bP flakes which is closer from a 2D application point of view, rather than surfaces of bulk bP cleaved *in-situ*, used in earlier studies.

This sample preparation method, can also be used to prepare clean surface of other reactive materials like Silicene, Stenene, Germanene and Borophene. So, it paves the way for the development of not only bP but also other 2D materials by allowing clean sample preparation in an inexpensive manner.

The observation of monolayer deep craters due to phosphorus desorption suggests that with proper tuning, layer by layer desorption of thin bP flakes could be obtained controlled by temperature. This could further enhance the preparation of thin bP samples. In principle one could start with few layer thin bP flakes and end up with a single monolayer by controlled annealing in UHV. Such systematic control of thinning of bP would enable realization of devices, which could allow optical response of bP in the infrared spectrum, which is of great interest for applications in medical imaging, night vision, and optical communication networks.

Combined with the controllable thinning of bP flakes by annealing, selective deposition of copper on a single layer of bP would allow realization of p-n diode on monolayer bP. Apart from n-type doping, copper also causes an increase in the band gap of bP. Thus, deposition of copper unlocks another opportunity to control the band gap of bP.

A selective deposition of copper on bP, apart from giving two regions with different doping, would also cause a difference in band gap values in the two regions. This is similar to the creation of a heterostructure along the 2D plane of bP. So, a repetition of such selective deposition of copper with controlled lateral interval would enable creation of superlattices on bP, which is another research opportunity to be explored with wide practical applications.

Bibliography

[1] F. Bassani and G. Pastori Parravicini. Band structure and optical properties of graphite and of the layer compounds GaS and GaSe. *Il Nuovo Cimento B (1965-1970)*, 50(1):95–128, 1967.

[2] G. Fischer and J. L. Brebner. Electrical resistivity and Hall effect of single crystals of GaTe and GaSe. *Journal of Physics and Chemistry of Solids*, 23(10):1363 – 1370, 1962.

[3] R. Fivaz and E. Mooser. Electron-phonon interaction in semiconducting layer structures. *Phys. Rev.*, 136:A833–A836, 1964.

[4] A. Gouskov, J. Camassel, and L. Gouskov. Growth and characterization of III–VI layered crystals like GaSe, GaTe, InSe, $GaSe_{(1-x)}Te_x$ and $Ga_xIn_{(1-x)}Se$. *Progress in Crystal Growth and Characterization*, 5(4):323 – 413, 1982.

[5] J. A. Wilson and A. D. Yoffe. The transition metal dichalcogenides discussion and interpretation of the observed optical, electrical and structural properties. *Advances in Physics*, 18(73):193–335, 1969.

[6] A. D. Yoffe. Layer compounds. *Annual Review of Materials Science*, 3(1):147–170, 1973.

[7] Alexander E. Karu and Michael Beer. Pyrolytic formation of highly crystalline graphite films. *Journal of Applied Physics*, 37(5):2179–2181, 1966.

[8] Chuhei Oshima, Eisuke Bannai, Takaho Tanaka, and Shichio Kawai. Carbon layer on lanthanum hexaboride (100) surface. *Japanese Journal of Applied Physics*, 16(6):965–969, 1977.

[9] M. Eizenberg and J. M. Blakely. Carbon monolayer phase condensation on Ni(111). *Surface Science*, 82(1):228 – 236, 1979.

[10] J.C. Hamilton and J.M. Blakely. Carbon segregation to single crystal surfaces of Pt, Pd and Co. *Surface Science*, 91(1):199 – 217, 1980.

[11] T. Aizawa, R. Souda, S. Otani, Y. Ishizawa, and C. Oshima. Anomalous bond of monolayer graphite on transition-metal carbide surfaces. *Phys. Rev. Lett.*, 64:768–771, 1990.

[12] Takashi Aizawa, Ryutaro Souda, Yoshio Ishizawa, Hideki Hirano, Taro Yamada, Ken ichi Tanaka, and Chuhei Oshima. Phonon dispersion in monolayer graphite formed on Ni(111) and Ni(001). *Surface Science*, 237(1):194 – 202, 1990.

[13] A. Nagashima, K. Nuka, K. Satoh, H. Itoh, T. Ichinokawa, C. Oshima, and S. Otani. Electronic structure of monolayer graphite on some transition metal carbide surfaces. *Surface Science*, 287-288:609 – 613, 1993.

[14] Ayato Nagashima, Kenji Nuka, Hiroshi Itoh, Takeo Ichinokawa, Chuhei Oshima, and Shigeki Otani. Electronic states of monolayer graphite formed on TiC(111) surface. *Surface Science*, 291(1):93 – 98, 1993.

[15] A. Nagashima, K. Nuka, H. Itoh, T. Ichinokawa, C. Oshima, S. Otani, and Y. Ishizawa. Two-dimensional plasmons in monolayer graphite. *Solid State Communications*, 83(8):581 – 585, 1992.

[16] A. Nagashima, H. Itoh, T. Ichinokawa, C. Oshima, and S. Otani. Change in the electronic states of graphite overlayers depending on thickness. *Phys. Rev. B*, 50:4756–4763, 1994.

[17] H. Itoh, T. Ichinose, C. Oshima, T. Ichinokawa, and T. Aizawa. Scanning tunneling microscopy of monolayer graphite epitaxially grown on a TiC(111) surface. *Surface Science*, 254(1):L437 – L442, 1991.

[18] R.J. Simonson and M. Trenary. An infrared study of the adsorption of borazine, $(BHNH)_3$, on the Pt(111) Surface. *Journal of Electron Spectroscopy and Related Phenomena*, 54-55:717 – 728, 1990.

[19] A. Nagashima, N. Tejima, Y. Gamou, T. Kawai, and C. Oshima. Electronic dispersion relations of monolayer hexagonal boron nitride formed on the Ni(111) surface. *Phys. Rev. B*, 51:4606–4613, 1995.

[20] A. Nagashima, N. Tejima, Y. Gamou, T. Kawai, and C. Oshima. Electronic structure of monolayer hexagonal boron nitride physisorbed on metal surfaces. *Phys. Rev. Lett.*, 75:3918–3921, 1995.

[21] P. W. Bridgman. Two new modifications of phosphorus. *Journal of the American Chemical Society*, 36(7):1344–1363, 1914.

[22] Yuichi Akahama, Shoichi Endo, and Shin-ichiro Narita. Electrical properties of black phosphorus single crystals. *Journal of the Physical Society of Japan*, 52(6):2148–2155, 1983.

[23] John C. Jamieson. Crystal structures adopted by black phosphorus at high pressures. *Science*, 139(3561):1291–1292, 1963.

[24] A. Brown and S. Rundqvist. Refinement of the crystal structure of black phosphorus. *Acta Crystallographica*, 19(4):684–685, 1965.

[25] H Asahina and A Morita. Band structure and optical properties of black phosphorus. *Journal of Physics C: Solid State Physics*, 17(11):1839–1852, 1984.

[26] S. Sugai and I. Shirotani. Raman and infrared reflection spectroscopy in black phosphorus. *Solid State Communications*, 53(9):753 – 755, 1985.

[27] Shin-ichiro Narita, Shin-ichi Terada, Shigeru Mori, Kiyofumi Muro, Yuichi Akahama, and Shoichi Endo. Far-infrared cyclotron resonance absorptions in black phosphorus single crystals. *Journal of the Physical Society of Japan*, 52(10):3544–3553, 1983.

[28] Robert W. Keyes. The electrical properties of black phosphorus. *Phys. Rev.*, 92:580–584, 1953.

[29] Akira Morita and Taizo Sasaki. Electron-phonon interaction and anisotropic mobility in black phosphorus. *Journal of the Physical Society of Japan*, 58(5):1694–1704, 1989.

[30] Haruki Kawamura, Ichimin Shirotani, and Kyoji Tachikawa. Anomalous superconductivity and pressure induced phase transitions in black phosphorus. *Solid State Communications*, 54(9):775 – 778, 1985.

[31] J. Wittig and B. T. Matthias. Superconducting phosphorus. *Science*, 160(3831):994–995, 1968.

[32] K. S. Novoselov, A. K. Geim, S. V. Morozov, D. Jiang, Y. Zhang, S. V. Dubonos, I. V. Grigorieva, and A. A. Firsov. Electric field effect in atomically thin carbon films. *Science*, 306(5696):666–669, 2004.

[33] K. S. Novoselov, A. K. Geim, S. V. Morozov, D. Jiang, M. I. Katsnelson, I. V. Grigorieva, S. V. Dubonos, and A. A. Frisov. Two-dimensional gas of massless Dirac fermions in graphene. *Nature*, 438:197–200, 2005.

[34] K. S. Novoselov, Z. Jiang, Y. Zhang, S. V. Morozov, H. L. Stormer, U. Zeitler, J. C. Maan, G. S. Boebinger, P. Kim, and A. K. Geim. Room-temperature Quantum Hall Effect in Graphene. *Science*, 315(5817):1379–1379, 2007.

[35] The nobel prize in physics 2010, 2010.

[36] Zehua Hu, Zhangting Wu, Cheng Han, Jun He, Zhenhua Ni, and Wei Chen. Two-dimensional transition metal dichalcogenides: interface and defect engineering. *Chem. Soc. Rev.*, 47:3100–3128, 2018.

[37] A. K. Geim and I. V. Grigorieva. Van der Waals heterostructures. *Nature*, 499:419–425, 2013.

[38] Alessandro Molle, Joshua Goldberger, Michel Houssa, Yong Xu, Shou-Cheng Zhang, and Deji Akinwande. Buckled two-dimensional Xene sheets. *Nature Materials*, 16:163, 2017.

[39] Patrick Vogt, Paola De Padova, Claudio Quaresima, Jose Avila, Emmanouil Frantzeskakis, Maria Carmen Asensio, Andrea Resta, Bénédicte Ealet, and Guy Le Lay. Silicene: Compelling experimental evidence for graphenelike two-dimensional silicon. *Phys. Rev. Lett.*, 108:155501, 2012.

[40] M E Dávila, L Xian, S Cahangirov, A Rubio, and G Le Lay. Germanene: a novel two-dimensional germanium allotrope akin to graphene and silicene. *New Journal of Physics*, 16(9):095002, 2014.

[41] Zhu, Feng-feng and Chen, Wei-jiong and Xu, Yong and Gao, Chun-lei and Guan, Dan-dan and Liu, Can-hua and Qian, Dong and Zhang, Shou-Cheng and Jia, Jin-feng. Epitaxial growth of two-dimensional stanene. *Nature Materials*, 14:1020, 2015.

[42] Yong Xu, Binghai Yan, Hai-Jun Zhang, Jing Wang, Gang Xu, Peizhe Tang, Wenhui Duan, and Shou-Cheng Zhang. Large-gap quantum spin Hall Insulators in Tin Films. *Phys. Rev. Lett.*, 111:136804, 2013.

[43] Yong Xu, Zhongxue Gan, and Shou-Cheng Zhang. Enhanced thermoelectric performance and anomalous Seebeck effects in topological insulators. *Phys. Rev. Lett.*, 112:226801, 2014.

[44] Stephan Rachel and Motohiko Ezawa. Giant magnetoresistance and perfect spin filter in silicene, germanene, and stanene. *Phys. Rev. B*, 89:195303, 2014.

[45] Andrew J. Mannix, Xiang-Feng Zhou, Brian Kiraly, Joshua D. Wood, Diego Alducin, Benjamin D. Myers, Xiaolong Liu, Brandon L. Fisher, Ulises Santiago, Jeffrey R. Guest, Miguel Jose Yacaman, Arturo Ponce, Artem R. Oganov, Mark C. Hersam, and Nathan P. Guisinger. Synthesis of borophenes: Anisotropic, two-dimensional boron polymorphs. *Science*, 350(6267):1513–1516, 2015.

[46] Baojie Feng, Jin Zhang, Qing Zhong, Wenbin Li, Shuai Li, Hui Li, Peng Cheng, Sheng Meng, Lan Chen, and Kehui Wu. Experimental realization of two-dimensional boron sheets. *Nature Chemistry*, 8:563, 2016.

[47] K. S. Novoselov, A. Mishchenko, A. Carvalho, and A. H. Castro Neto. 2D materials and van der Waals heterostructures. *Science*, 353(6298), 2016.

[48] Han Liu, Adam T. Neal, Zhen Zhu, Zhe Luo, Xianfan Xu, David Tománek, and Peide D. Ye. Phosphorene: An unexplored 2D semiconductor with a high hole mobility. *ACS Nano*, 8(4):4033–4041, 2014.

[49] Andres Castellanos-Gomez, Leonardo Vicarelli, Elsa Prada, Joshua O Island, K L Narasimha-Acharya, Sofya I Blanter, Dirk J Groenendijk, Michele Buscema, Gary A Steele, J V Alvarez, Henny W Zandbergen, J J Palacios, and Herre S J van der Zant. Isolation and characterization of few-layer black phosphorus. *2D Materials*, 1(2):025001, 2014.

[50] Saptarshi Das, Wei Zhang, Marcel Demarteau, Axel Hoffmann, Madan Dubey, and Andreas Roelofs. Tunable transport gap in phosphorene. *Nano Letters*, 14(10):5733–5739, 2014.

[51] Vy Tran, Ryan Soklaski, Yufeng Liang, and Li Yang. Layer-controlled band gap and anisotropic excitons in few-layer black phosphorus. *Phys. Rev. B*, 89:235319, 2014.

[52] Xi Ling, Han Wang, Shengxi Huang, Fengnian Xia, and Mildred S. Dresselhaus. The renaissance of black phosphorus. *Proceedings of the National Academy of Sciences*, 112(15):4523–4530, 2015.

[53] Fengnian Xia, Han Wang, and Yichen Jia. Rediscovering black phosphorus as an anisotropic layered material for optoelectronics and electronics. *Nature Communications*, 5:4458, 2014.

[54] Han Liu, Yuchen Du, Yexin Deng, and Peide D. Ye. Semiconducting black phosphorus: synthesis, transport properties and electronic applications. *Chem. Soc. Rev.*, 44:2732–2743, 2015.

[55] Ruixiang Fei and Li Yang. Strain-engineering the anisotropic electrical conductance of few-layer black phosphorus. *Nano Lett.*, 14(5):2884–2889, 2014.

[56] Likai Li, Yijun Yu, Guo Jun Ye, Qingqin Ge, Xuedong Ou, Hua Wu, Donglai Feng, Xian Hui Chen, and Yuanbo Zhang. Black phosphorus field-effect transistors. *Nature Nanotechnology*, 9:372, 2014.

[57] Steven P. Koenig, Rostislav A. Doganov, Hennrik Schmidt, A. H. Castro Neto, and Barbaros Özyilmaz. Electric field effect in ultrathin black phosphorus. *Applied Physics Letters*, 104(10):103106, 2014.

[58] Tu Hong, Bhim Chamlagain, Wenzhi Lin, Hsun-Jen Chuang, Minghu Pan, Zhixian Zhou, and Ya-Qiong Xu. Polarized photocurrent response in black phosphorus field-effect transistors. *Nanoscale*, 6:8978–8983, 2014.

[59] Michele Buscema, Dirk J. Groenendijk, Gary A. Steele, Herre S. J. van der Zant, and Andres Castellanos-Gomez. Photovoltaic effect in few-layer black phosphorus PN junctions defined by local electrostatic gating. *Nature Communications*, 5:4651, 2014.

[60] Michele Buscema, Dirk J. Groenendijk, Sofya I. Blanter, Gary A. Steele, Herre S. J. van der Zant, and Andres Castellanos-Gomez. Fast and broadband photoresponse of few-layer black phosphorus field-effect transistors. *Nano Lett.*, 14(6):3347–3352, 2014.

[61] Ruixiang Fei, Alireza Faghaninia, Ryan Soklaski, Jia-An Yan, Cynthia Lo, and Li Yang. Enhanced thermoelectric efficiency via orthogonal electrical and thermal conductances in phosphorene. *Nano Lett.*, 14(11):6393–6399, 2014.

[62] Guangzhao Qin, Qing-Bo Yan, Zhenzhen Qin, Sheng-Ying Yue, Hui-Juan Cui, Qing-Rong Zheng, and Gang Su. Hinge-like structure induced unusual properties of black phosphorus and new strategies to improve the thermoelectric performance. *Scientific Reports*, 4:6946, 2014.

[63] Liangzhi Kou, Thomas Frauenheim, and Changfeng Chen. Phosphorene as a superior gas sensor: Selective adsorption and distinct I-V response. *J. Phys. Chem. Lett.*, 5(15):2675–2681, 2014.

[64] Brian Kiraly, Nadine Hauptmann, Alexander N. Rudenko, Mikhail I. Katsnelson, and Alexander A. Khajetoorians. Probing single vacancies in black phosphorus at the atomic level. *Nano Letters*, 17(6):3607–3612, 2017.

[65] Steven P. Koenig, Rostislav A. Doganov, Leandro Seixas, Alexandra Carvalho, Jun You Tan, Kenji Watanabe, Takashi Taniguchi, Nikolai Yakovlev, Antonio H. Castro Neto, and Barbaros Özyilmaz. Electron doping of ultrathin black phosphorus with cu adatoms. *Nano Letters*, 16(4):2145–2151, 2016. PMID: 26938106.

[66] A. Morita. Semiconducting black phosphorus. *Applied Physics A*, 39(4):227–242, 1986.

[67] P. W. Bridgman. Further note on black phosphorus. *J. Am. Chem. Soc.*, 38(3):609–612, 1916.

[68] Robert B. Jacobs. Phosphorus at high temperatures and pressures. *The Journal of Chemical Physics*, 5(12):945–953, 1937.

[69] Mikihiko Ikezawa, Yasuhiro Kondo, and Ichimin Shirotani. Infrared optical absorption due to one and two phonon processes in black phosphorus. *Journal of the Physical Society of Japan*, 52(5):1518–1520, 1983.

[70] Naoshi Suzuki and Masato Aoki. Interplanar forces of black phosphorus caused by electron-lattice interaction. *Solid State Communications*, 61(10):595 – 600, 1987.

[71] Kiyotaka Shibata, Taizo Sasaki, and Akira Morita. The energy band structure of black phosphorus and angle-resolved ultraviolet photoelectron spectra. *Journal of the Physical Society of Japan*, 56(6):1928–1931, 1987.

[72] A. N. Rudenko and M. I. Katsnelson. Quasiparticle band structure and tight-binding model for single- and bilayer black phosphorus. *Phys. Rev. B*, 89:201408, 2014.

[73] Hanchul Kim. Effect of van der Waals interaction on the structural and cohesive properties of black phosphorus. *Journal of the Korean Physical Society*, 64(4):547–553, 2014.

[74] Yan Li, Shengxue Yang, and Jingbo Li. Modulation of the electronic properties of ultrathin black phosphorus by strain and electrical field. *J. Phys. Chem. C*, 118(41):23970–23976, 2014.

[75] A. S. Rodin, A. Carvalho, and A. H. Castro Neto. Strain-induced gap modification in black phosphorus. *Phys. Rev. Lett.*, 112:176801, 2014.

[76] Qun Wei and Xihong Peng. Superior mechanical flexibility of phosphorene and few-layer black phosphorus. *Applied Physics Letters*, 104(25):251915, 2014.

[77] Ruixiang Fei and Li Yang. Lattice vibrational modes and Raman scattering spectra of strained phosphorene. *Applied Physics Letters*, 105(8):083120, 2014.

[78] Xihong Peng, Qun Wei, and Andrew Copple. Strain-engineered direct-indirect band gap transition and its mechanism in two-dimensional phosphorene. *Phys. Rev. B*, 90:085402, 2014.

[79] Jin-Wu Jiang and Harold S Park. Mechanical properties of single-layer black phosphorus. *Journal of Physics D: Applied Physics*, 47(38):385304, 2014.

[80] Yuanyue Liu, Fangbo Xu, Ziang Zhang, Evgeni S. Penev, and Boris I. Yakobson. Two-dimensional mono-elemental semiconductor with electronically inactive defects: The case of phosphorus. *Nano Lett.*, 14(12):6782–6786, 2014.

[81] Xue-fang Yu, Hiroshi Ushiyama, and Koichi Yamashita. Comparative study of sodium and lithium intercalation and diffusion mechanism in black phosphorus from first-principles simulation. *Chemistry Letters*, 43(12):1940–1942, 2014.

[82] Jin-Wu Jiang and Harold S. Park. Negative Poisson's ratio in single-layer black phosphorus. *Nature Communications*, 5:4727, 2014.

[83] Shuang Zhang, Jiong Yang, Renjing Xu, Fan Wang, Weifeng Li, Muhammad Ghufran, Yong-Wei Zhang, Zongfu Yu, Gang Zhang, Qinghua Qin, and Yuerui Lu. Extraordinary photoluminescence and strong temperature/angle-dependent Raman responses in few-layer phosphorene. *ACS Nano*, 8(9):9590–9596, 2014.

[84] Wanglin Lu, Haiyan Nan, Jinhua Hong, Yuming Chen, Chen Zhu, Zheng Liang, Xiangyang Ma, Zhenhua Ni, Chuanhong Jin, and Ze Zhang. Plasma-assisted fabrication of monolayer phosphorene and its Raman characterization. *Nano Research*, 7(6):853–859, 2014.

[85] V. Tayari, N. Hemsworth, I. Fakih, A. Favron, E. Gaufrès, G. Gervais, R. Martel, and T. Szkopek. Two-dimensional magnetotransport in a black phosphorus naked quantum well. *Nature Communications*, 6:7702, 2015.

[86] Han Wang, Xiaomu Wang, Fengnian Xia, Luhao Wang, Hao Jiang, Qiangfei Xia, Matthew L. Chin, Madan Dubey, and Shu-jen Han. Black phosphorus radio-frequency transistors. *Nano Lett.*, 14(11):6424–6429, 2014.

[87] Yuchen Du, Han Liu, Yexin Deng, and Peide D. Ye. Device perspective for black phosphorus field-effect transistors: Contact resistance, ambipolar behavior, and scaling. *ACS Nano*, 8(10):10035–10042, 2014.

[88] H. Liu, A. T. Neal, M. Si, Y. Du, and P. D. Ye. The effect of dielectric capping on few-layer phosphorene transistors: Tuning the Schottky barrier heights. *IEEE Electron Device Letters*, 35(7):795–797, 2014.

[89] Yexin Deng, Zhe Luo, Nathan J. Conrad, Han Liu, Yongji Gong, Sina Najmaei, Pulickel M. Ajayan, Jun Lou, Xianfan Xu, and Peide D. Ye. Black phosphorus-monolayer MoS_2 van der Waals heterojunction p-n diode. *ACS Nano*, 8(8):8292–8299, 2014.

[90] Tony Low, Michael Engel, Mathias Steiner, and Phaedon Avouris. Origin of photoresponse in black phosphorus phototransistors. *Phys. Rev. B*, 90:081408, 2014.

[91] Michael Engel, Mathias Steiner, and Phaedon Avouris. Black phosphorus photodetector for multispectral, high-resolution imaging. *Nano Lett.*, 14(11):6414–6417, 2014.

[92] Leonardo Viti, Jin Hu, Dominique Coquillat, Wojciech Knap, Alessandro Tredicucci, Antonio Politano, and Miriam Serena Vitiello. Black phosphorus terahertz photodetectors. *Advanced Materials*, 27(37):5567–5572, 2015.

[93] Xiaomu Wang, Aaron M. Jones, Kyle L. Seyler, Vy Tran, Yichen Jia, Huan Zhao, Han Wang, Li Yang, Xiaodong Xu, and Fengnian Xia. Highly anisotropic and robust excitons in monolayer black phosphorus. *Nature Nanotechnology*, 10:517, 2015.

[94] Jingsi Qiao, Xianghua Kong, Zhi-Xin Hu, Feng Yang, and Wei Ji. High-mobility transport anisotropy and linear dichroism in few-layer black phosphorus. *Nature Communications*, 5:4475, 2014.

[95] Ruixiang Fei and Li Yang. Strain-engineering the anisotropic electrical conductance of few-layer black phosphorus. *Nano Lett.*, 14(5):2884–2889, 2014.

[96] Zhen Zhu and David Tománek. Semiconducting layered blue phosphorus: A computational study. *Phys. Rev. Lett.*, 112:176802, 2014.

[97] Jie Guan, Zhen Zhu, and David Tománek. Phase coexistence and metal-insulator transition in few-layer phosphorene: A computational study. *Phys. Rev. Lett.*, 113:046804, 2014.

[98] Xiaoyu Han, Henry Morgan Stewart, Stephen A. Shevlin, C. Richard A. Catlow, and Zheng Xiao Guo. Strain and orientation modulated bandgaps and effective masses of phosphorene nanoribbons. *Nano Lett.*, 14(8):4607–4614, 2014.

[99] Xihong Peng, Andrew Copple, and Qun Wei. Edge effects on the electronic properties of phosphorene nanoribbons. *Journal of Applied Physics*, 116(14):144301, 2019.

[100] Hongyan Guo, Ning Lu, Jun Dai, Xiaojun Wu, and Xiao Cheng Zeng. Phosphorene nanoribbons, phosphorus nanotubes, and van der Waals multilayers. *J. Phys. Chem. C*, 118(25):14051–14059, 2014.

[101] Vy Tran and Li Yang. Scaling laws for the band gap and optical response of phosphorene nanoribbons. *Phys. Rev. B*, 89:245407, 2014.

[102] Ashwin Ramasubramaniam and Andre R. Muniz. Ab initio studies of thermodynamic and electronic properties of phosphorene nanoribbons. *Phys. Rev. B*, 90:085424, 2014.

[103] Jun Dai and Xiao Cheng Zeng. Bilayer phosphorene: Effect of stacking order on bandgap and its potential applications in thin-film solar cells. *J. Phys. Chem. Lett.*, 5(7):1289–1293, 2014.

[104] Alexandre Favron, Etienne Gaufrés, Frédéric Fossard, Anne-Laurence Phaneuf-L'Heureux, Nathalie Y.-W. Tang, Pierre L. Lévesque, Annick Loiseau, Richard Leonelli, Sébastien Francoeur, and Richard Martel. Photooxidation and quantum confinement effects in exfoliated black phosphorus. *Nature Materials*, 14:826, 2015.

[105] Yuan Huang, Jingsi Qiao, Kai He, Stoyan Bliznakov, Eli Sutter, Xianjue Chen, Da Luo, Fanke Meng, Dong Su, Jeremy Decker, Wei Ji, Rodney S. Ruoff, and Peter Sutter. Interaction of black phosphorus with oxygen and water. *Chemistry of Materials*, 28(22):8330–8339, 2016.

[106] Wei Luo, Dmitry Y Zemlyanov, Cory A Milligan, Yuchen Du, Lingming Yang, Yanqing Wu, and Peide D Ye. Surface chemistry of black phosphorus under a controlled oxidative environment. *Nanotechnology*, 27(43):434002, 2016.

[107] Shueh Lin Yau, Thomas P. Moffat, Allen J. Bard, Zhengwei Zhang, and Michael M. Lerner. STM of the (010) surface of orthorhombic phosphorus. *Chemical Physics Letters*, 198(3-4):383–388, 1992.

[108] C. D. Zhang, J. C. Lian, W. Yi, Y. H. Jiang, L. W. Liu, H. Hu, W. D. Xiao, S. X. Du, L. L. Sun, and H. J. Gao. Surface structures of black phosphorus investigated with scanning tunneling microscopy. *The Journal of Physical Chemistry C*, 113(43):18823–18826, 2009.

[109] Liangbo Liang, Jun Wang, Wenzhi Lin, Bobby G. Sumpter, Vincent Meunier, and Minghu Pan. Electronic bandgap and edge reconstruction in phosphorene materials. *Nano Letters*, 14(11):6400–6406, 2014.

[110] J. V. Riffle, C. Flynn, B. St. Laurent, C. A. Ayotte, C. A. Caputo, and S. M. Hollen. Impact of vacancies on electronic properties of black phosphorus probed by STM. *Journal of Applied Physics*, 123(4):044301, 2018.

[111] Zhizhan Qiu, Hanyan Fang, Alexandra Carvalho, A S Rodin, Yanpeng Liu, Sherman J.R. Tan, Mykola Telychko, Pin Lv, Jie Su, Yewu Wang, A H Castro Neto, and Jiong Lu. Resolving the Spatial Structures of Bound Hole States in Black Phosphorus. *Nano Letters*, 17(11):6935–6940, 2017.

[112] Qingfeng Gui, Xiaobin Zhu, Lizhe Liu, Zhen-Yu Jia, Ye-Heng Song, Shao-Chun Li, Paul K. Chu, and Xinglong Wu. Identification of lattice oxygen in few-layer black phosphorus exfoliated in ultrahigh vacuum and largely improved ambipolar

field-effect mobilities by hydrogenation and phosphorization. *ACS Appl. Mater. Interfaces*, 9(45):39804–39811, 2017.

[113] Yanpeng Liu, Zhizhan Qiu, Alexandra Carvalho, Yang Bao, Hai Xu, Sherman J. R. Tan, Wei Liu, A. H. Castro Neto, Kian Ping Loh, and Jiong Lu. Gate-tunable giant Stark effect in few-layer black phosphorus. *Nano Letters*, 17(3):1970–1977, 2017.

[114] Xiaolong Liu, Joshua D. Wood, Kan-Sheng Chen, EunKyung Cho, and Mark C. Hersam. In situ thermal decomposition of exfoliated two-dimensional black phosphorus. *The Journal of Physical Chemistry Letters*, 6(5):773–778, 2015.

[115] Matthieu Fortin-Deschênes, Pierre L. Levesque, Richard Martel, and Oussama Moutanabbir. Dynamics and mechanisms of exfoliated black phosphorus sublimation. *The Journal of Physical Chemistry Letters*, 7(9):1667–1674, 2016.

[116] Nawat Suvansinpan, Fayyaz Hussain, Gang Zhang, Cheng Hsin Chiu, Yongqing Cai, and Yong-Wei Zhang. Substitutionally doped phosphorene: electronic properties and gas sensing. *Nanotechnology*, 27(6):065708, 2016.

[117] Priyank Rastogi, Sanjay Kumar, Somnath Bhowmick, Amit Agarwal, and Yogesh Singh Chauhan. Effective doping of monolayer phosphorene by surface adsorption of atoms for electronic and spintronic applications. *IETE Journal of Research*, 63(2):205–215, 2017.

[118] Bingchao Yang, Bensong Wan, Qionghua Zhou, Yue Wang, Wentao Hu, Weiming Lv, Qian Chen, Zhongming Zeng, Fusheng Wen, Jianyong Xiang, Shijun Yuan, Jinlan Wang, Baoshun Zhang, Wenhong Wang, Junying Zhang, Bo Xu, Zhisheng Zhao, Yongjun Tian, and Zhongyuan Liu. Te-doped black phosphorus field-effect transistors. *Advanced Materials*, 28(42):9408–9415, 2016.

[119] Yijun Xu, Jian Yuan, Linfeng Fei, Xinliang Wang, Qiaoliang Bao, Yu Wang, Kai Zhang, and Yuegang Zhang. Selenium-doped black phosphorus for high-responsivity 2D photodetectors. *Small*, 12(36):5000–5007, 2016.

[120] Jimin Kim, Seung Su Baik, Sae Hee Ryu, Yeongsup Sohn, Soohyung Park, Byeong-Gyu Park, Jonathan Denlinger, Yeonjin Yi, Hyoung Joon Choi, and Keun Su Kim. Observation of tunable band gap and anisotropic Dirac semimetal state in black phosphorus. *Science*, 349(6249):723–726, 2015.

[121] A Sanna, A V Fedorov, N I Verbitskiy, J Fink, C Krellner, L Petaccia, A Chikina, D Yu Usachov, A Grüneis, and G Profeta. First-principles and angle-resolved photoemission study of lithium doped metallic black phosphorous. *2D Materials*, 3(2):025031, 2016.

[122] Brian Kiraly, Elze J. Knol, Klara Volckaert, Deepnarayan Biswas, Alexander N. Rudenko, Danil A. Prishchenko, Vladimir G. Mazurenko, Mikhail I. Katsnelson, Philip Hofmann, Daniel Wegner, and Alexander A. Khajetoorians. Anisotropic two-dimensional screening at the surface of black phosphorus. *arXiv e-prints*, page arXiv:1906.02627, 2019.

[123] C. Julian Chen. *Introduction to Scanning Tunneling Microscopy.* Oxford University Press Inc., New York, 2008.

[124] Karina Morgenstern. Scanning Tunneling Microscopy. Ruhr-Universität Bochum, webpage: https://www.ruhr-uni-bochum.de/pc1/methoden/rastertunnelmikroskopie.html.en, 2019.

[125] J. Bardeen. Tunnelling from a many-particle point of view. *Phys. Rev. Lett.*, 6:57–59, 1961.

[126] J. Tersoff and D. R. Hamann. Theory of the scanning tunneling microscope. *Phys. Rev. B*, 31:805–813, 1985.

[127] Alexander Saranin A. V. Zotov M. Katayama K. Oura, V. G. Lifshits. *Surface Science*. Springer-Verlag Berlin Heidelberg, 2003.

[128] Tom Nilges, Marcel Kersting, and Thorben Pfeifer. A fast low-pressure transport route to large black phosphorus single crystals. *Journal of Solid State Chemistry*, 181(8):1707 – 1711, 2008.

[129] D. W. Feldman, James H. Parker, W. J. Choyke, and Lyle Patrick. Raman scattering in $6H$ SiC. *Phys. Rev.*, 170:698–704, 1968.

[130] L.M. Malard, M.A. Pimenta, G. Dresselhaus, and M.S. Dresselhaus. Raman spectroscopy in graphene. *Physics Reports*, 473(5):51 – 87, 2009.

[131] Focus, Omicron Nanotechnology, Limburger Str. 75 D-65232 Taunusstein Germany. *EFM3s*, 3.9 edition.

[132] John P. Perdew, Matthias Ernzerhof, and Kieron Burke. Rationale for mixing exact exchange with density functional approximations. *The Journal of Chemical Physics*, 105(22):9982–9985, 1996.

[133] Stefan Grimme. Semiempirical GGA-type density functional constructed with a long-range dispersion correction. *Journal of Computational Chemistry*, 27(15):1787–1799, 2006.

[134] Andrea Dal Corso. Pseudopotentials periodic table: From H to Pu. *Computational Materials Science*, 95:337 – 350, 2014.

[135] J Hass, W A de Heer, and E H Conrad. The growth and morphology of epitaxial multilayer graphene. *Journal of Physics: Condensed Matter*, 20(32):323202, 2008.

[136] Neeraj Mishra, John Boeckl, Nunzio Motta, and Francesca Iacopi. Graphene growth on silicon carbide: A review. *Physica Status Solidi (a)*, 213(9):2277–2289, 2016.

[137] Yongqing Cai, Qingqing Ke, Gang Zhang, Boris I. Yakobson, and Yong-Wei Zhang. Highly itinerant atomic vacancies in phosphorene. *Journal of the American Chemical Society*, 138(32):10199–10206, 2016.

[138] I. Horcas, R. Fernández, J. M. Gómez-Rodríguez, J. Colchero, J. Gómez-Herrero, and A. M. Baro. WSXM: A software for scanning probe microscopy and a tool for nanotechnology. *Review of Scientific Instruments*, 78(1):013705, 2007.

[139] L. Daukiya, M.N. Nair, M. Cranney, F. Vonau, S. Hajjar-Garreau, D. Aubel, and L. Simon. Functionalization of 2D materials by intercalation. *Progress in Surface Science*, 94(1):1 – 20, 2019.

[140] Madeline S. Stark, Kaci L. Kuntz, Sean J. Martens, and Scott C. Warren. Intercalation of layered materials from bulk to 2D. *Advanced Materials*, 31(27):1808213, 2019.

[141] Ziyuan Lin, Jingli Wang, Xuyun Guo, Jiewei Chen, Chao Xu, Mingqiang Liu, Bilu Liu, Ye Zhu, and Yang Chai. Interstitial copper-doped edge contact for n-type carrier transport in black phosphorus. *InfoMat*, 1(2):242–250, 2019.

[142] M Vladimirova, M Stengel, A. De Vita, A Baldereschi, M Böhringer, K Morgenstern, R Berndt, and W.-D Schneider. Supramolecular self-assembly and selective step decoration on the Au(111) surface. *Europhysics Letters*, 56(2):254–260, 2001.

[143] M. Krohn, G. Gerth, and H. Stenzel. Conditions of step decoration on crystal surfaces. *physica status solidi (a)*, 55(2):375–383, 1979.

[144] W. Kohn and L. J. Sham. Self-consistent equations including exchange and correlation effects. *Phys. Rev.*, 140:A1133–A1138, 1965.

[145] P. Hohenberg and W. Kohn. Inhomogeneous electron gas. *Phys. Rev.*, 136:B864–B871, 1964.

[146] P. Giannozzi, S. Baroni, N. B., M. Calandra, R. Car, C. Cavazzoni, D. Ceresoli, G. L. Chiarotti, M. Cococcioni, I. Dabo, A. Dal Corso, S. de Gironcoli, S. Fabris, G. Fratesi, R. Gebauer, U. Gerstmann, C. Gougoussis, A. Kokalj, M. Lazzeri, L. Martin-Samos, N. Marzari, F. Mauri, R. Mazzarello, S. Paolini, A. Pasquarello,

L. Paulatto, C. Sbraccia, S. Scandolo, G. Sclauzero, A. P. Seitsonen, A. Smogunov, P. Umari, and R. M. Wentzcovitch. QUANTUM ESPRESSO: a modular and open-source software project for quantum simulations of materials. *Journal of Physics: Condensed Matter*, 21(39):395502, 2009.

[147] P Giannozzi, O Andreussi, T Brumme, O Bunau, M Buongiorno Nardelli, M Calandra, R Car, C Cavazzoni, D Ceresoli, M Cococcioni, N Colonna, I Carnimeo, A Dal Corso, S de Gironcoli, P Delugas, R A DiStasio, A Ferretti, A Floris, G Fratesi, G Fugallo, R Gebauer, U Gerstmann, F Giustino, T Gorni, J Jia, M Kawamura, H-Y Ko, A Kokalj, E Küçükbenli, M Lazzeri, M Marsili, N Marzari, F Mauri, N L Nguyen, H-V Nguyen, A Otero de-la Roza, L Paulatto, S Poncé, D Rocca, R Sabatini, B Santra, M Schlipf, A P Seitsonen, A Smogunov, I Timrov, T Thonhauser, P Umari, N Vast, X Wu, and S Baroni. Advanced capabilities for materials modelling with quantum ESPRESSO. *Journal of Physics: Condensed Matter*, 29(46):465901, 2017.

[148] Daniel Sheppard, Penghao Xiao, William Chemelewski, Duane D. Johnson, and Graeme Henkelman. A generalized solid-state nudged elastic band method. *The Journal of Chemical Physics*, 136(7):074103, 2012.

[149] Bruce J Berne, Giovanni Ciccotti, and David F Coker. *Classical and Quantum Dynamics in Condensed Phase Simulations.* WORLD SCIENTIFIC, 1998. Pages:385–404.

[150] Ziyuan Lin, Jingli Wang, Xuyun Guo, Jiewei Chen, Chao Xu, Mingqiang Liu, Bilu Liu, Ye Zhu, and Yang Chai. Interstitial copper-doped edge contact for n-type carrier transport in black phosphorus. *InfoMat*, 1(2):242–250, 2019.

List of Figures